Effect of Substrate and Morphology on the Relaxation Dynamics of Carriers and Phonons in Graphene

By

Zeynab Jarrahi

Dissertation
Submitted to the Faculty of the
Graduate School of Vanderbilt University
in partial fulfillment of the requirements
for the degree of

DOCTOR OF PHILOSOPHY
in

Physics
August, 2016
Nashville, Tennessee

Approved:

Professor Norman Tolk

Professor Jim Davidson

Professor Richard Mu

Professor Volker Oberacker

Professor Kalman Varga

ACKNOWLEDGMENTS

This Dissertation would not have been possible without the financial support from the Department of Energy (DOE), the Army Research Office (ARO), the National Science Foundation (NSF), as well as the resources and technical support provided by Vanderbilt Institute of Nanoscale Science and Engineering (VINSE).

I am forever grateful to my parents for their never ending love and support and especially to my mom who raised me to believe I could do anything I set my mind to. I am thankful to Ted Cinker for his all-encompassing support and patience and for proof reading this dissertation despite it being long and boring.

I am indebted to my advisor Dr. Norman Tolk for his guidance, trust and mentoring style which gave me the confidence to be an independent thinker and provided me with the freedom to shape my own path. I must acknowledge Dr. Jim Davidson for his help on all things diamond. I must also thank many others who were a part of this journey, VINSE staff: Anthony Hmelo, Bo Choi, Ben Schmidt and Vanderbilt administrative team: Don Pickert, Peggy McGowan, Jane Fall, Barbara Amann, Sheila Warf and Libby Johnson.

TABLE OF CONTENTS

LIST OF FIGURES

FOREWORD

Graphene, the two dimensional allotrope of the carbon family, exhibits extremely high electron mobility, thermal conductivity and fascinating ultrafast carrier-carrier and carrier-phonons interactions. However, being merely one atom thick, introducing a substrate or altering the morphological form of graphene can affect both its equilibrium and non-equilibrium dynamics and inevitably influence the performance of graphene-based devices. In the first part of this dissertation, we use fluence and energy dependent ultrafast pump-probe spectroscopy to determine the effect of substrate on the femtosecond transient electron and phonon dynamics of single layer graphene transferred on sapphire, quartz and single crystalline diamond.

Using a multi-channel cooling theory involving surface phonons of the substrate, intrinsic optical phonons of graphene and the corresponding competing scattering rates, we proceed to explain the strong substrate-dependent dynamics of graphene observed in our experiments. We stipulate that the sub-nm surface roughness of the studied substrates, enable a strong coupling between the phototexcited carriers in graphene and the surface vibrational modes of the polar substrates. We show that this additional energy relaxation pathway can compete with the intrinsic phonons of graphene to not only reduce the transient electron temperature but also the carrier and optical phonon lifetimes in graphene.

In the second part of this dissertation, we introduce a methodology for fabrication of a novel quasi-one dimensional morphology of graphene called curled graphene ribbons (CGR). Our gate dependent scanning photocurrent measurements reveal an astounding two orders of magnitude enhancement in the photocurrent response of CGR which we attributed to the photothermoelectric effect (PTE).

Understanding how the equilibrium and non-equilibrium dynamics of carriers and phonons in graphene are altered by the interface or morphology and deciphering the various energy relaxation pathways, will pave the way towards realization of higher performance graphene based electronics and optoelectronics.

CHAPTER

1. GRAPHENE

1.1. Introduction

Graphene, the 2D allotrope of the carbon family, was deemed unstable at room temperature for decades.[1] Half a century ago, Mermin and Wagner stipulated that a 2D material is thermodynamically unstable due to the thermal fluctuations of the membrane which, at any finite temperature, would lead to a displacement of atoms greater or comparable to the distance between the atoms and ultimately lead to dissociation.[2][3] In 1947, P.R Wallace calculated the band structure of graphene and identified graphene as a zero bandgap semiconductor.[4] Almost 40 years later, DiVincenzo introduced the linear dispersion of graphene near the zone edges and predicted the relativistic nature of the electrons as a consequence of this linearity.[5] Although some work on graphene was reported in the following decades, the breakthrough came about in 2004 when Geim and Novoselov reported observation of a single layer graphene made by mechanical exfoliation.[6] It is believed that the inherent ripples and height fluctuations in a free standing layer of graphene is the underlying reason for its stability in the three dimensional space.[7] The extraordinary transport properties of graphene, in addition to the easy fabrication process, initiated one of the fastest paced research areas in the history.[8] In the first part of this chapter, we will discuss the linear band structure of graphene and its implications on the associated density of states (DOS) of graphene. The second part of this chapter will cover the optical properties of graphene in the visible and near IR spectral range. We will then discuss the interband and intraband transitions and their contributions to the optical sheet conductivity of graphene. This topic will be discussed in more details in chapter 3.

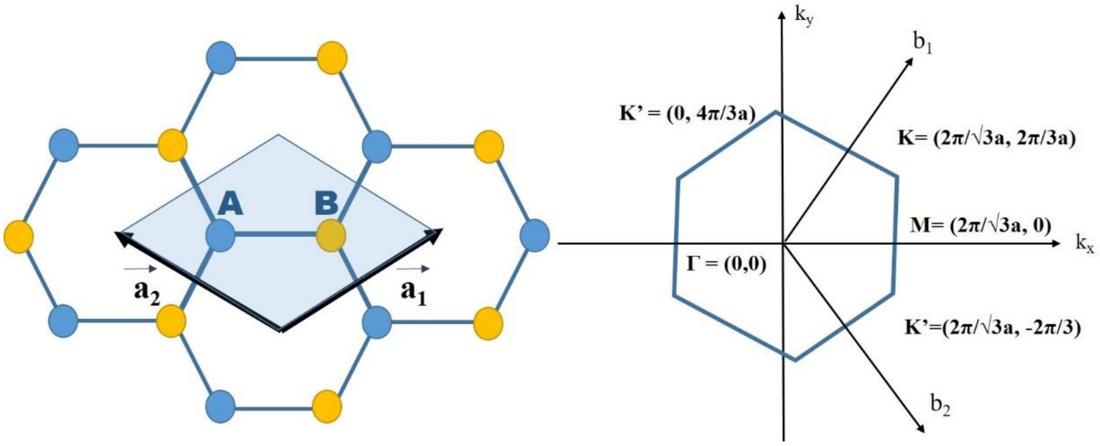

Figure 1.1. (a) The lattice of single layer pristine graphene, where lattice vectors a_1 and a_2 define the unit cell which is shown in light blue. **(b)** The first Brillouin zone of graphene which is defined by the reciprocal lattice vectors b_1 and b_2. $\Gamma = (0,0)$ is in the center of the hexagon and K and K' points are in the corners of the hexagon. M point is defined as the middle point of the neighboring high symmetry K and K' points.

1.2. Band structure of graphene

Graphene is a sp^2 hybridized lattice of carbon atoms in a hexagonal honey comb configuration. Figure 1.1. (a) shows the unit cell of single layer graphene consisting of two un-equivalent atoms: A and B, defined by the lattice vectors $a_1 = a_0(1/2, \surd 3/2)$ and $a_2 = a_0(1/2, -\surd 3/2)$, with the lattice constant a_0 = 0.2461. The high symmetry points of the Brillouin zone (BZ), described by $\Gamma = (0,0)$, $K = 1/a_0\ (2\pi/\surd 3, 2\pi/3)$ and $M = 1/a_0\ (2\pi/\surd 3, 0)$ are shown in Figure 1.1. (b). K and K' points are particularly important for resonant processes in graphene and will be discussed in more detail in Chapter 2.

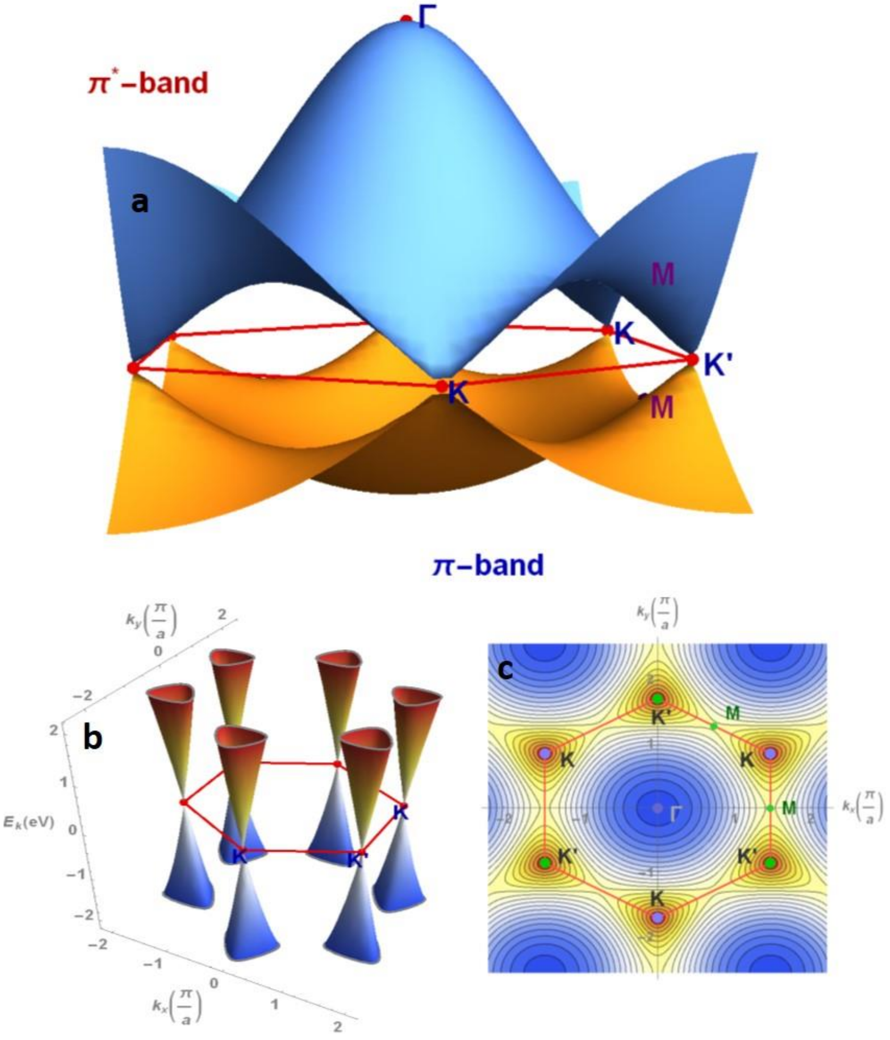

Figure 1.2 (a) 3D energy dispersion for the two π bands in the first Brillouin zone of a hexagonal lattice of single layer graphene. **(b)** Pseudo-3D near-linear energy dispersion for the two π bands near k points (Dirac cones). **(c)** Constant energy contours for the π valence band and the first Brillouin zone of graphene.

The two carbon atoms in the unit cell of graphene, each contribute four electrons and evidently form graphene's unique band structure. Three of these electrons form the sp^2

hybridized orbitals responsible for the extremely strong planar covalent σ bonds that give rise to the unusual stiffness of graphene. [9] With a measured Young's modulus of up to $1\ TPa$ [10], this stiffness is also related to the high thermal conductivity of $\sim 5300\ W \cdot m^{-1} \cdot K^{-1}$ for suspended graphene.[11] These σ bonds are energetically separated and due to the Pauli principle, have a filled shell. As a result, they form valence bands far from the Dirac point and are not considered in the scope of this thesis.

The remaining 2pz electron contributes to the binding and anti-binding π and π^* bonds that are perpendicular to the plane of graphene. Only these electrons can contribute to the transport and conductivity phenomena in graphene. Lack of a band gap and the filled valence and empty conduction bands at zero temperature, fits graphene into the semi-metal category.

The band structure of graphene was first calculated by Wallace in 1947. [4] Within the picture of the tight binding model with the nearest neighbor approximation, the energy dispersion can be described as:

$$E = \pm\sqrt{\gamma_0^2(1 + 4\ \cos^2(\pi k_y\, a) +\ 4\cos(\pi k_y a)\cos(\pi k_x\sqrt{3}a)} \qquad \text{Eq.1.1}$$

where γ_0 is the nearest neighbor hopping energy and a is the lattice constant. Figure 1.2. (a) shows the π and $\pi *$ bands touching at the high symmetry points K and K' of the BZ. The point where the conduction and valance bands come together is called the Dirac point (Figure 1.2. (b)) where charge carriers experience a linear dispersion around this crossing. Further away in the BZ, one can see the saddle point singularity in the electronic band at the M point. In the center of the BZ at Γ point, the conduction and valence bands are separated with an energy gap of ~ 20 eV,[12][13] the equi-energy contour near this point is isotropic in character and follows a parabolic dispersion. (Figure 1.2. (a) and (c)) In the vicinity of the Dirac point and in the linear regime, equation 1.1 can be formulated as:

$$E = \upsilon_F \hbar \Delta k \,, \qquad \text{Eq.1.2}$$

where ħ is the Plank's constant, $\upsilon_F \approx 10^6 \ {}^{m}/_{S}$ is the Fermi velocity and Δk is the 2D wave-vector relative to the K-point. Equation 1.3 below, shows the Einstein's energy-momentum relation:

$$E = \sqrt{m^2c^4 + p^2c^2} = mc^2\sqrt{1 + \frac{p^2}{m^2c^2}} \,, \qquad \text{Eq.1.3}$$

When $p^2 \gg \ m^2c^2$, this equation can be approximated as:

$$E \simeq pc = \hbar kc \,, \qquad \text{Eq.1.4}$$

A simple comparison between equations 1.2 and 1.4 highlights the relativistic nature of the carriers in graphene. According to the Dirac equations, electrons in graphene behave as massless Dirac fermions with a velocity $\upsilon_F{\sim}c/300$.[12]

The two dimensional DOS per unit area can be formulated as:

$$D(E) = \frac{2}{A}\sum_k \delta(E(\boldsymbol{k}) - E) \,, \qquad \text{Eq.1.5}$$

where a factor of two has been added for the spin degeneracy. Integrating over the Brillouin zone we get:

$$D(E) = \frac{1}{2\pi^2}\int \delta(E(\boldsymbol{k}) - E)\, d^2k \,, \qquad \text{Eq.1.6}$$

With the Dirac approximation $E(\boldsymbol{k}) = \pm\hbar\upsilon_F q$ close to the K and K' points, an analytical solution can be written as:

$$D(E) = \frac{1}{\pi^2} \iint \delta(\hbar v_F q - E)\, d^2 q = \frac{2}{\pi} \int_0^\infty \delta(\hbar v_F q - E)\, q dq$$

$$= \frac{2}{\pi \hbar^2 v_F^2} \int_0^\infty \delta(u - E) u\, du \qquad \text{Eq.1.7}$$

Consequently, DOS can be approximated as:

$$D(E) = \frac{2|E|}{\pi \hbar^2 v_F^2} \qquad \text{Eq.1.8}$$

Equation 1.8 implies that pristine graphene has a DOS of zero at the Dirac point. The linear increase of DOS with energy, in addition to the linear band structure around the zone edges and the zero band gap, lead to the extremely high electron mobility of graphene which can reach $200{,}000\ cm^2/Vs$.[14] The room temperature (RT) mobility of graphene $\sim 15{,}000\ cm^2/Vs$ [8] greatly exceeds that of silicon ~ $1400\ cm^2/Vs$. [15] Although some semi-conductors such as InSb, show RT mobilities of ~ $77{,}000\ cm^2/Vs$, these values refer to the bulk undoped sample and not the intrinsic material.

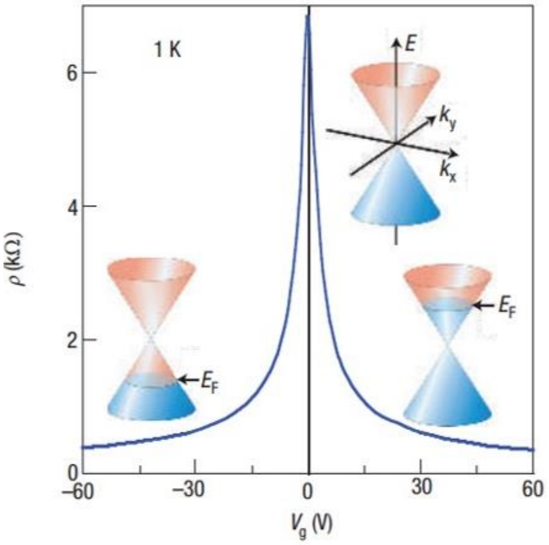

Figure 1.3. Ambipolar electric field effect in single layer graphene. The inset shows the Dirac cone near K point of the BZ. The figure shows the change in the Fermi level of graphene as the gating voltage is changed and the consequent change in the resistivity of graphene. (Reference [8])

Figure 1.3 displays graphene's ambipolar field effect, where the charge carrier density in graphene can be tuned as high as $10^{13}\ cm^{-2}$ both below and above the Dirac point. [8] Interestingly enough, the mobility of graphene does not vary considerably even at high doping levels. The long mean free path of $\sim 0.5\ \mu m$, fits graphene's transport into the ballistic regime and makes graphene a desirable candidate for field effect transistor (FET) applications.[16]

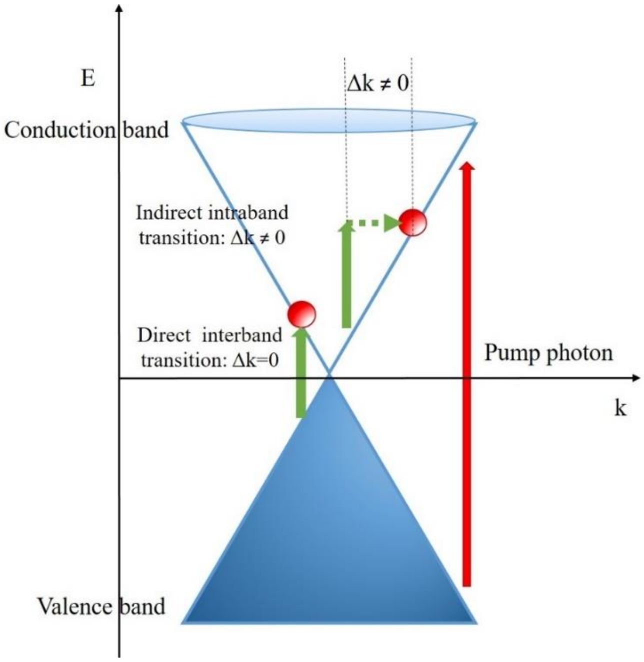

Figure 1.4. Dirac cone of graphene near the K point. Green arrows indicate possible direct and indirect intra and inter band transitions. The indirect intraband transitions will require a change in the momentum of the carriers.

1.3. Optical properties of graphene

The initial discovery of single layer exfoliated graphene in 2004, was in part due to graphene's strong optical absorption in the visible spectral range. Even though graphene is one atom thick, the absorbance of ∼2.3 % made its detection under optical microscope a possibility.[6] The coveted broad band absorption, in combination with an extremely high electron mobility, makes graphene a strong contender in optoelectronic applications such as near IR and THz detectors and saturable absorbers.[17][18] Being a flexible transparent conductor, the future of graphene might lie in the transparent touch screens. One of the advantages of graphene over current contenders, such as Indium Tin Oxide (ITO), stems from the abundancy of carbon as opposed to rare elements.

The optical absorption in graphene is due to two fundamentally different contributions from interband and intraband phenomena. (Figure 1.4) In the far-IR spectral range, free carrier absorption or intra-band transitions are dominant. However, in the mid to near IR range, the optical response of graphene is mostly due to the inter-band transitions between the valence and conduction band.[19][20]

1.3.1. Interband transitions and universal absorption of graphene

Inter-band transitions occur when carriers are directly excited from the valence band to the conduction band of graphene. (Figure 1.5. (b)) When a photon with an energy above IR gets absorbed, an electron-hole pair is created and the optical response of graphene will be mainly dominated by this band to band transition. The net loss of the photon energy can be linked to the real part of the optical sheet conductivity. The optical sheet conductivity of graphene for the inter-band phenomena can be described as: [21] [22]

$$\sigma_{inter}(\omega) = \frac{\pi e^2}{4h}\left[\tanh(\frac{\hbar\omega+2E_F}{4K_BT}) + \tanh(\frac{\hbar\omega-2E_F}{4K_BT})\right] \quad \text{Eq.1.9}$$

For pristine graphene at zero temperature and zero doping, the optical conductivity response in the linear dispersion regime can be described as: [19] [23]

$$\sigma(\omega) = \pi e^2/2h \qquad \text{Eq.1.10}$$

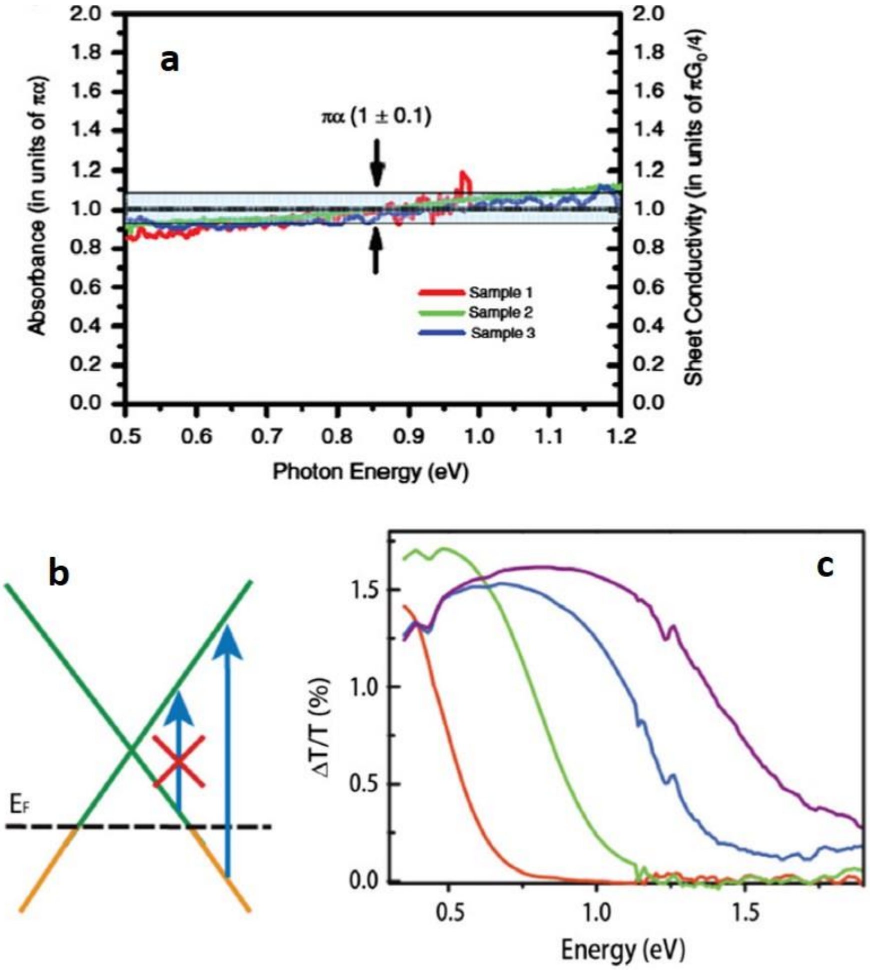

Figure 1.5. (a) Universal absorbance and optical sheet conductivity of graphene in the energy range: 0.5-1.2 eV. The absorbance is in units of πα with α being the fine structure constant of the matter. The black line corresponds to the universal sheet optical absorbance of single layer graphene πα=2.293%. **(b)** Schematics of interband transitions for hole doped graphene where optical transitions or absorption with photon energies below $|2E_F|$ are blocked. **(c)** Change in transmission of hole-doped graphene induced by gate voltage, curves from left to right correspond to the transmission for values of change in Vg from charge neutrality point: -0.75,-1.75,-2.75 and -3.5 Reference [31]

This frequency independent response is referred to as the universal absorption of graphene and is equal to a universal value determined by the fine structure constant of the matter $\alpha = \frac{e^2}{4\pi\varepsilon_0\hbar c} \simeq 1/137$ in pristine graphene for the discussed spectral range. [24] (Figure 1.5. (a)) In the next section we will discuss how this universal conductivity corresponds to a transmittance of $\sim 97.7\%$ or universal absorption of $\sim 2.3\%$ in graphene.[25]

1.3.2. Optical transmission in 2D graphene

When the incident light is perpendicular to the plane of graphene, we can determine the associated optical transmission through the amplitude of the electric field:[26]

$$E = Ae^{i\mathbf{k}.r} = Ae^{ik_0\tilde{n}\,z} = Ae^{ik_0nz}e^{-k_0kz} \qquad \text{Eq.1.12}$$

With the complex refractive index being: $\tilde{n} = n + ik,$ Eq.1.13

Then the transmittance T of a single layer graphene with a thickness d can be defined as:

$$T = \frac{I}{I_0}, \qquad \text{Eq.1.14}$$

where I is the intensity of the incident light after it passes through graphene and I_0 is the intensity of the light before it is incident on graphene. Since the intensity of the light is related to square of the electric field $I \propto |E|^2 = A^2e^{-2k_0kz}$, the transmittance can be written as:

$$T = \frac{I}{I_0} = e^{-2k_0kd} \simeq 1 - 2k_0kd\ , \qquad \text{Eq.1.15}$$

where $k_0 = \omega/c$. Knowing the relation between the polarization density, the susceptibility and the current density in graphene, one can write:[26]

$$\mathbf{P}(\omega) = \varepsilon_0 \chi(\omega) \mathbf{E}(\omega), \qquad \text{Eq.1.16}$$

$$\mathbf{J}(\omega) = \sigma_{3D}(\omega) \mathbf{E}(\omega), \qquad \text{Eq.1.17}$$

$$\mathbf{J}_P(t) = \frac{\partial \mathbf{P}(t)}{\partial t}, \qquad \text{Eq.1.18}$$

Here the time dependent component of the electric field will be in the form of $e^{-i\omega t}$, therefore we obtain :

$$\mathbf{J}(\omega) = -i\omega \varepsilon_0 \chi(\omega) \mathbf{E}(\omega), \qquad \text{Eq.1.19}$$

The conductivity then could be derived as:

$$\chi(\omega) = \frac{i\sigma_{3D}(\omega)}{\omega \varepsilon_0}, \qquad \text{Eq.1.20}$$

The three dimensional conductivity approach we adopted, can be related to the two dimensional space through:

$$\sigma_{2D}(\omega) = d\sigma_{3D}(\omega), \qquad \text{Eq.1.21}$$

hence we will have: $\chi(\omega) = \frac{i\sigma_{2D}(\omega)}{d\omega\varepsilon_0}$, Eq.1.22

knowing that: $\tilde{n} = \sqrt{\varepsilon_r \, \mu_r}$, Eq.1.23

With $\varepsilon_r = \chi + 1$, where ε_r is the releative permitivity and μ_r, is the relative permeability (in case of graphene ~1), we can Taylor expand Eq.1.23 into:

$$\tilde{n} \simeq 1 + \frac{1}{2}\chi, \qquad \text{Eq.1.24}$$

As a result, Eq.1.13 can be written as:

$$\tilde{n}(\omega) \simeq 1 + \frac{i\sigma_{2D}(\omega)}{2d\omega\varepsilon_0}, \qquad \text{Eq.1.25}$$

$$k(\omega) = \frac{Re\{\sigma_{2D}(\omega)\}}{2d\omega\varepsilon_0}, \qquad \text{Eq.1.26}$$

and the transmittance T becomes: $T(\omega) = 1 - \frac{Re\{\sigma_{2D}(\omega)\}}{c\varepsilon_0}$, Eq.1.27

For the spectral regions where the universal absorption is valid, we will have $\sigma_0 = e^2/4\hbar$ which ultimately yields: $T(\omega) = 1 - \frac{\sigma_0}{c\varepsilon_0} = 1 - \pi\alpha = 97.7\%$.

1.3.3. Intraband transitions in graphene

The intraband contribution to the optical conductivity of mono layer graphene due to electron-photon scattering processes can be written as : [27][28][29]

$$\sigma_{intra}(\omega) = -\frac{e^2\omega}{i\pi\hbar}\int_{-\infty}^{\infty} dE \frac{|E|}{\omega^2}\frac{\partial f_0(E)}{\partial E} , \qquad \text{Eq.1.28}$$

where f_0 is the Fermi Dirac function:

$$f_0(E) = \frac{1}{\mathrm{e}^{(E - E_F/K_B T)} + 1} . \qquad \text{Eq.1.29}$$

To take into account the electron-disorder/phonon scattering processes, we can write $\omega \rightarrow \omega + i\tau^{-1}$, where τ is the scattering time. Depending on the scattering mechanism, τ can be a function of temperature, impurity or carrier density. Integrating over the equation above, we will obtain:

$$\sigma_{intra}(\omega) = \frac{2iK_B T e^2}{\pi\hbar(\omega + i\tau^{-1})} \ln\left[2\,cosh\left(\frac{E_F}{2K_B T}\right)\right] . \qquad \text{Eq.1.30}$$

When $E_F \gg kT$, the intraband contribution takes the familiar form of Drude-Boltzman expression:

$$\sigma_{intra}(\omega) = \frac{ie^2}{\pi\hbar} \frac{|E_F|}{(\omega+i\tau^{-1})}. \qquad \text{Eq.1.31}$$

An accurate description of the optical dynamics of graphene in a certain spectral range is not possible unless both interband and intraband transitions are considered. We will discuss the total optical conductivity response of graphene $\sigma_{total=}\sigma_{intra} + \sigma_{inter}$ in detail in chapter 3.

1.3.4. Effect of doping on the transmission of graphene

At zero doping density, when there is no shift in the Fermi energy of graphene, the entire conduction band is empty. Therefore, all energies are resonant and any incident photon can get absorbed through creation of an electron-hole pair with similar energy. This phenomena, results in a broadband absorption at a wide range of wavelengths. However,

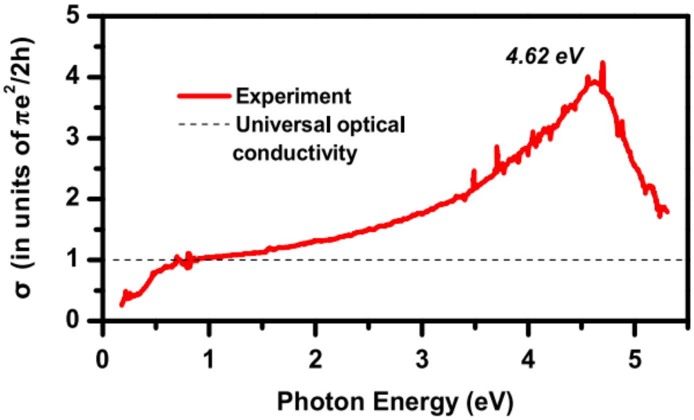

Figure 1.6. Experimental optical conductivity in a wide spectral range (0.25-5.5 eV) as obtained by reference[95]

when there is a shift in the Fermi energy of graphene, due to the Pauli blocking phenomena, the inter-band absorption is suppressed for photon energies below $2|E_F|$. (Figure 1.5. (b)) It is important to note that due to the fabrication process and the presence of the substrate, most graphene samples are unintentionally doped. The Fermi energy in graphene can also be shifted by hundreds of meV via electrostatic gating. [30] (Figure 1.5. (c)) The Pauli blocking of certain transitions due to the change in the carrier density, provides an easy method to measure the Fermi level of graphene without the hassles of microfabrication. The energy threshold where the absorption starts to increase, can reveal the value of $2|E_F|$ and enables us to accurately extract the carrier density through $n = E_F^2/\pi\hbar^2 v_F^2$. [31]

1.3.5. Optical conductivity of graphene in the UV range

Further away from the Dirac cone and away from the linear regime, the optical conductivity of graphene no longer fits in the universal conductivity picture (Figure1.6). The frequency dependent conductivity shows an absorption peak close to $\sim 4.6\ eV$.[32] This resonance can be explained by the band to band transitions near the saddle point singularity at the M point and taking into account the excitonic effects. Although graphene does not have a bandgap and no stationary bound excitons can exist, the electron-hole interactions create a redistribution of the oscillator strength and result in a strong excitonic coupling with the electronic band continuum.[33]

CHAPTER

2. METHODS

2.1. Introduction

The exciting future of graphene in electronics and optoelectronics, further highlights the need for a scalable and large area synthesis of graphene that could be easily integrated into the current industry. Although exfoliated graphene has excellent electronic properties and mobilities, the translation of this technique which has its limitations in terms of reproducibility and large area coverage, into the industry is not quite feasible. Chemical vapor deposition (CVD) method for graphene growth, can yield uniform, large area graphene with electronic properties that can come close to that of the exfoliated samples. In the first part of this chapter, we will discuss different graphene synthesis techniques and optimization of the CVD process and recipes for high quality, large area single layer graphene growth.

The process of transferring CVD graphene onto desired substrates can degrade the desired properties of graphene by introducing impurities or mechanically degrading the fragile graphene membrane. Section 4 will cover a fabrication methodology, developed and used throughout this thesis which can yield clean graphene with little polymer residue. The underlying substrate plays an important role in the different properties of graphene, in section 5, we will characterize and discuss the effect of the surface roughness and its significance in the context of this thesis.

One of the most versatile and time-saving characterization tools in the field of graphene research is Raman spectroscopy. The final section of this chapter will discuss different Raman processes and our utilization of this technique to characterize the layer number, orientation, strain and intrinsic doping of graphene samples.

2.2. Graphene synthesis

2.2.1. Mechanically exfoliated graphene

The first isolation of mono layer graphene from highly ordered pyrolytic graphite (HOPG) occurred in 2004 by Geim and Novoselov using a scotch tape method.[34] The bonding of layers in graphite is of Van der Waals nature which is quite weak ~ $(2\ eV/nm^2)$. Hence, small forces around 300 nN/μm^2 arising from the scotch tape adhesive is enough to separate these layers. In the micro-mechanical exfoliation method, bulk graphite pieces are placed on the adhesive part of a Scotch tape and after repeated peeling, flakes of graphene of different thicknesses are left on the tape. The tape is then pressed on the desired substrate leaving these flakes behind.[34] The quality of exfoliated graphene and the clean nature of this technique drove researchers to opt for this method for studying the *fundamental* electrical and optical properties of graphene. However, due to the small micrometer size crystals and the arbitrary and uncontrollable positioning on the desired substrates, this method is not suitable for technological purposes and large scale production.

2.2.2. Epitaxial Graphene

Epitaxial graphene is a common growth technique that renders high quality large area graphene on the surface of Silicon Carbide (SiC). This technique is based on sublimation of Si from Silicon carbide at temperatures$\sim 1400 - 1600°C$. At these high temperatures Si leaves the surface of SiC and a subsequent graphitization of the surface occurs.[35] Using carbon terminated SiC instead of Si terminated SiC, one can obtain a better graphene coverage.[36] Although epitaxial graphene offers high quality and large area production, the initial cost of SiC and the high temperatures required for the graphitization, renders this method incompatible with a wide range of substrates commonly used in the well-established electronic industry.

2.2.3. Chemical Vapor Deposition (CVD) Graphene

The possibility of large area growth, high degree of control and reproducibility in the production of CVD graphene, and the inherent electrical properties rivaling exfoliated graphene, has made CVD growth method one of the most viable options for the transition of graphene into the industry. [37][38] After the successful isolation of single layer graphene in 2004, many efforts were made to grow larger area graphene on metals. It has been shown that most transition metals serve as efficient catalysts in the transformation of hydro-carbons into graphitic compounds.[39] However, the low cost and extremely low carbon solubility of copper, has ranked copper, the most popular metal for the synthesis of CVD graphene. In this case, lack of bulk carbon and the surface catalysis, results in the self-termination of the growth process and yields uniform single layer graphene growth.[40]

2.3. CVD graphene growth

The first step of the CVD graphene growth is to reduce the oxides on the surface of the copper foil by annealing at high temperatures between $900 - 1000°C$, followed by an exposure to the hydrocarbon precursor. Although a higher temperature is required, we chose methane as our precursor due to its cleaner and more convenient nature. The nucleation of graphene on copper gets larger by feeding off the reactants from the precursor which are catalyzed on copper. The low pressures of the order of millitorr used in this process, result in the deposition of thin membranes of graphene and uniform single layer graphene coverage.

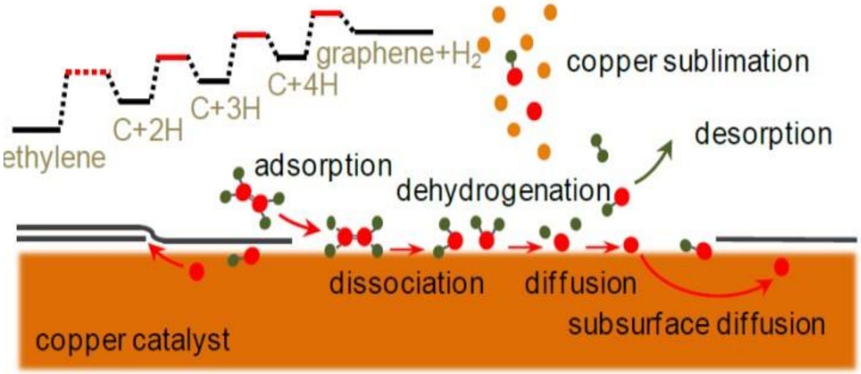

Figure 2.1. Schematics of the CVD graphene growth and the associated mechanisms. Reference [41]

2.3.1. CVD growth kinetics

Graphene growth kinetics have been the subject of extensive debates. It has been proposed that the growth process in CVD graphene is dominated by crystallization of the surface, where in the early stages, the surface is supersaturated with carbon ad-atoms and the graphene nucleation starts at a slightly later stage. A different model has been proposed by

Celebi et al. [41] implying that even after the nucleation process, the growth is still dependent on the continual hydrocarbon adsorption and desorption off of the copper surface. Copper sublimation is deemed to have a significant effect in slowing down the growth process after nucleation, however, when the carbon specie ad-atoms diffuse beneath the growing crystals of graphene, they are isolated and therefore protected from the copper sublimation and the eventual desorption. Figure 2.1 shows the different stages of the graphene growth, starting with the adsorption of hydrocarbon precursor on copper. The pool of intermediate hydrocarbon reactants can go under dissociation and dehydrogenation until they either attach to the graphene lattice or they are desorbed. As we mentioned earlier, this desorption is hindered when these reactants diffuse beneath the growing graphene layer and it is enhanced through the copper sublimation.

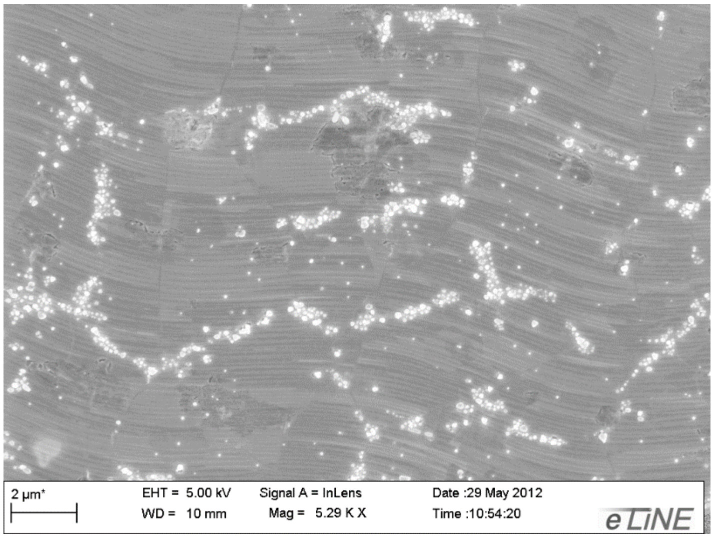

Figure 2.2. SEM images of white particles on the copper foil immediately after the graphene growth process.

2.3.2. Copper foil contamination

While characterizing our early CVD growths, we came across white scattered particles on some graphene samples grown on copper foil. (Figure 2.2) Optimizing the growth parameters seemed to have little effect on the density of these particles. However, we noticed that the older samples seem to have a higher density of these dots and also the density of these particles seemed to be more pronounced around the wrinkles in the copper foil. EDX measurements showed the composition of these dots to be mostly copper oxide. Our results were further confirmed by the work of Celebi et al. [41] where Nano Auger characterization methods revealed the elemental composition of these particles to be mainly copper oxide and chlorine agglomerates and mostly due to the oxidization after exposure to air.

2.3.3. CVD growth recipe

To grow single layer graphene in a high temperature, low pressure CVD furnace, we first treat the copper foil with acetone for approximately 10 minutes, followed by a 10 second IPA rinse to remove any impurities resident on the surface of copper that could contaminate the growth chamber. We then purge the gas lines with argon, methane, and hydrogen respectively and wait until the pressure gets below 10 $millitorr$. 100 $SCCM$ of Ar is then flown with the pressure staying at ~$3x10-1\ torr$. We then start the flow of 10 $SCCM$ of hydrogen and set the furnace temperature at $900°C$ and anneal the copper foil for 1 hour. After 60 minutes, we raise the temperature to $950°C$ and turn off the Ar flow and increase the hydrogen flow to 100 $SCCM$. At the same time, we begin the flow of our carbon precursor: 35 $SCCM$ of methane (CH_4). After 30 minutes, we set the furnace temperature to zero and turn off all gas lines except the Ar and move the quartz boat containing the copper foil out of the furnace. This recipe yields high quality, uniform single layer graphene with large grain size as confirmed by SEM images and Raman spectroscopy.

2.4. CVD graphene transfer

Chemical vapor deposition can provide great quality, large area graphene, however, the next challenge arises from transferring the mono layer of graphene from the copper foil onto the desired substrate. The most common method for small production graphene is the $PMMA$ method, where a layer of widely used polymer: Poly-methyl methacrylate ($PMMA$) is spun on top of graphene to act as support. The copper is then etched away leaving the graphene layer supported by $PMMA$ which can then be easily moved onto any substrate. After transfer to the destination substrate, the $PMMA$ is eventually removed. Although the $PMMA$ method has many advantages such as simplicity and high conformity, it also has its distinct drawbacks. The formation of wrinkles and cracks and especially difficulties involving the removal of the $PMMA$ residue from the surface, call for optimization of the transfer process suited to specific needs. Our optimized method, yields very clean graphene with little $PMMA$ residue. We also used AZ 9260 Photoresist as a substitute for $PMMA$ since it shows higher solubility in Acetone compared to $PMMA$, but the support that $PMMA$ provides proved to be superior to Photoresist. Therefore, we chose $PMMA$ with different anisole concentrations as our primary support polymer. We spin coat $PMMA$ on top of cm size copper foil at $4500\ rpm$. Figure 2.4 shows the $PMMA$ film thickness versus the spin coating speed. A thermal release tape is used in the back of the copper foil to prevent surface deformation of copper caused by the suction of the vacuum chuck. We noticed that even small deformations in the copper foil, while being spin coated, results in an inhomogeneous dispensing of the $PMMA$ and subsequently an inferior transfer, especially for free standing samples. We also noticed that the hot plate bake step at $180\ ºC$ suggetsed by some research groups[42] results in much harder $PMMA$ residue and makes PMMA etching more difficult. (Figure 2.3)

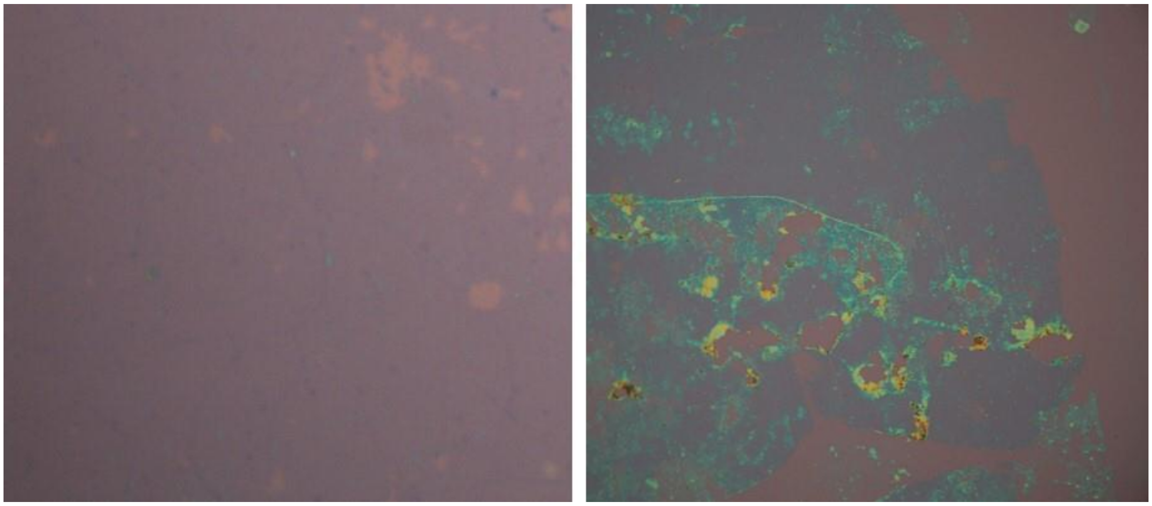

Figure 2.3. Optical images of single layer graphene transferred on SiO_2/Si substrate using PMMA. Left image shows a clean transfer while the right image shows an inferior transfer with improper removal of PMMA.

2.4.1. Etching copper

To etch away the copper foil underneath the graphene membrane, we use Ferric Chloride $(FeCl_3)$, due to its slow and controllable etching rate. The other advantage arises from the fact that unlike etchants such as HNO_3, where the etching process leads to formation of H_2 bubbles and causes tears and cracks and degradation of the carbon sp_2, the etching process with Ferric Chloride, does not generate any bubbles.[43] The etching time of 1 hour suggested by some groups does not seem sufficient to etch the copper particles especially in the edges and folds. We also observed that if the anisole concentration in $PMMA$ is higher, the longer etch times of over 24 hours can at times result in the disintegration of the floating graphene-$PMMA$ membrane. We found the that for $PMMA\ A4$ the optimized time is between 6-8 hours.

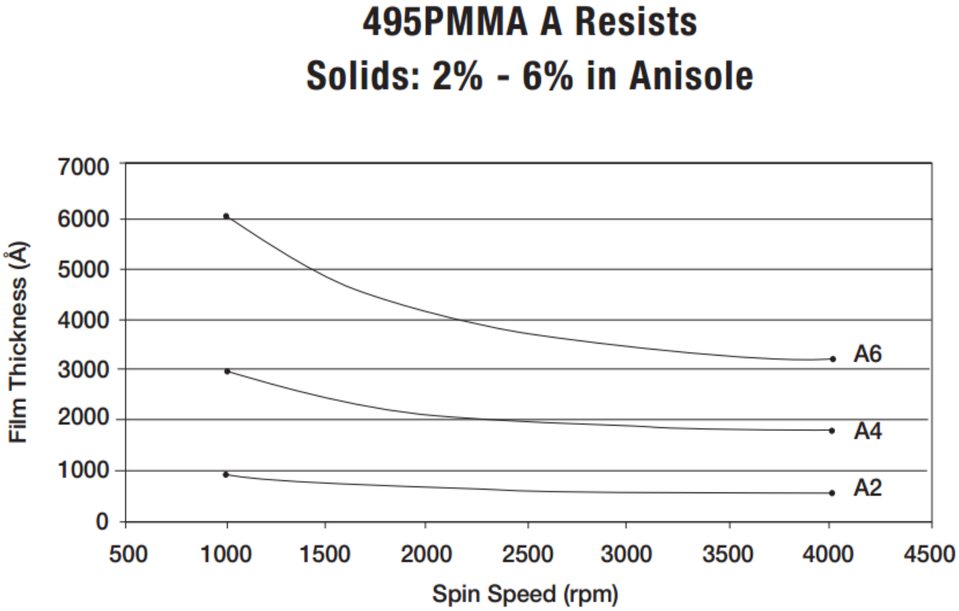

Figure 2.4. PMMA thickness versus spin coating speed for PMMA A2, A4 and A6. [188]

Another important factor that helps with the etching rate is the removal of the graphene layer that is grown on the bottom of the copper foil in the CVD growth process. To remove the backside graphene, we use reactive ion etching (RIE) oxygen plasma with a power of 30 W and flow rate of 30 $sccm$ for 10-20 seconds. We observed that for less solid $PMMA's$ such as $A2$, the amount of time that is required to etch graphene on the back, also provides enough time for the fragile graphene + $PMMA$ layer underneath to be attacked by plasma, which can degrade the edges of the transferred graphene layer. As a result, care needs to be exercised with the $PMMA$ concentration and the timing and power of the O_2 plasma treatment. Otherwise, the plasma will etch the edges of the protective $PMMA$ layer underneath, rendering a jagged transfer.

After the copper foil is etched, the floating PMMA + graphene layer needs to be thoroughly cleaned and rid of the copper etchant residue. It is common in the field to use a few Deionized Water (DI) dips for the duration of 10-60 minutes. Our observations show that this amount of time is not enough for a proper cleaning. We also found that using multiple water baths (5-10) and a subsequent dip of over 24 hours is superior to (1-3) baths for the same amount of time. If the residue of the copper etchant is not thoroughly rinsed, it can form a layer in-between graphene and the substrate, resulting in an inferior graphene transfer and degradation of device performance.

2.4.2. PMMA removal

One of the major drawbacks of the $PMMA$ method is the polymer residue of $\sim nm$ thickness which remains on the graphene surface after the bulk of the $PMMA$ has been removed by organic solvents. It has been shown that the $PMMA$ remnants can actually induce a weak p doping in graphene.[44] The main method for removing $PMMA$ involves dissolving the polymer in acetone followed by an isopropanol (IPA) rinse. Although this method removes the bulk of $PMMA$, the cleanliness is inferior for our specific needs. We experimented with a few different methods such as: leaving the samples in Acetone for varying amounts of time up to 48 hours, dissolving $PMMA$ in heated acetone bath as well as sonicating the samples in Acetone. Although better results were achieved by longer/heated acetone bath, a very thin $PMMA$ residue still remained on the surface, indicating that Acetone alone is not sufficient to remove $PMMA$. Another parameter that we carefully experimented with, was the amount of anisole in $PMMA$ and the thickness of the spin coated layer. Our observations indicate that, although the thinner layer of $A2$ (40 nm) is easier to remove, it does not provide enough support and protection for the multiple steps of the transfer, especially the oxygen plasma treatment. For the graphene samples used in chapter 3, we used 180 nm of $PMMA\ A4$ which provides enough support while not being too thick to be effectively removed.

Thermal annealing in gaseous atmospheres, in addition to solvent cleaning is a well-known method for removing the residue of $PMMA$. Annealing graphene in Ar, H_2 and a mixture of the two has been studied before.[45][46][47] In addition to annealing in ultra-high vacuum which has been shown to greatly increase the mobility of CVD graphene, [44] annealing in oxygen, followed by Hydrogen/Argon, is also shown to be effective in removing most of the $PMMA$ residue.[48]

We studied annealing CVD graphene in different gaseous mixtures. Our observations showed that the best results are achieved by first removing the bulk of $PMMA$ by solvents followed by a two-step thermal process. In this fashion, we will have a lower density of polymer debris compared to a single step annealing process and lesser chance of contaminating the chamber. We obtained our most successful results by first annealing $PMMA$ on a hot plate in ambient air for 30 minutes at $300\ ^{\circ}C$ followed by a hot furnace annealing in $Ar/\ H_2$ at $400\ ^{\circ}C$ for 3 hours. Our studies show that baking at higher temperatures in air, introduces defects in the lattice of graphene and results in a higher D peak in the Raman spectrum, most likely due to the partial oxidation of the graphene layer. (Figure 2.5)

2.5. The Substrate

Although graphene's excellent properties make it a desirable candidate for miniaturization of electronic and optoelectronics, the intrinsic properties of graphene are highly sensitive to the external environments and the substrate on which it resides. As a result, one needs to pay close attention to and accordingly characterize the substrate related parameters such as the roughness and passivation of the underlying surface.

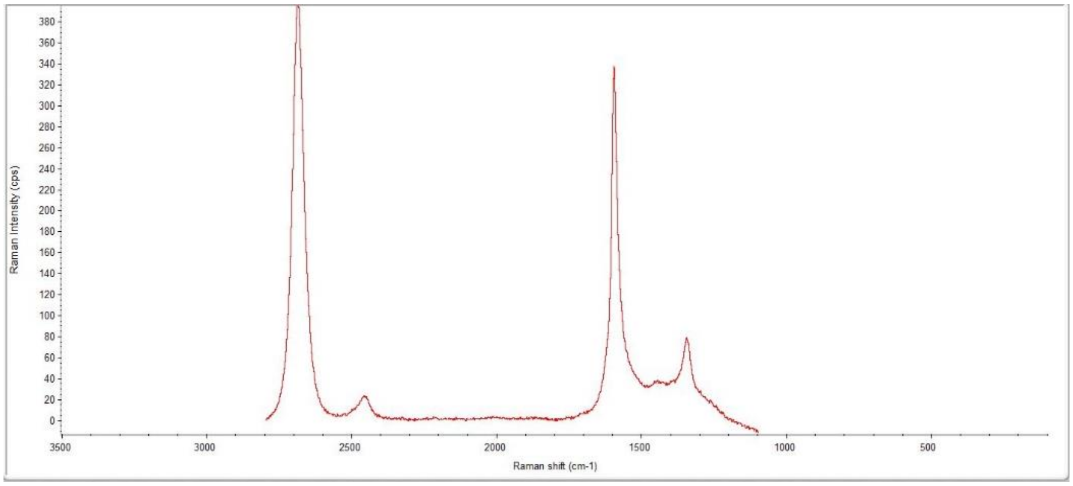

Figure 2.5. Raman spectrum of graphene on quartz annealed in air at 400ºC. The prominent D peak indicates the degradation of carbon lattice due to possible oxidation of graphene in air.

2.5.1. Surface roughness

The morphology and the roughness of the underlying substrate has a substantial impact on the fundamental properties of graphene and graphene based devices.[49] [50] The substrate induced corrugations in graphene are different from the random intrinsic corrugations occurring in suspended graphene. This substrate induced change in the morphology of graphene is shown to be strong enough to overcome the random inherit corrugations.[51] In an experimental work by Plantey et al., it is shown that the morphology of CVD graphene transferred on silica nano-pillars, can range from complete conformation to complete suspension, depending on the density, pitch and sharpness of the nano-pillars.[52] (Figure 2.6)

On the other hand, theoretical studies stipulate that depending on the surface roughness and interfacial binding energy, graphene can exhibit a sharp transition between two distinct morphologies: (1) closely conforming to the substrate (2) laying flat on the substrate's high points. [53][51] Figure 2.7. (a) shows the schematics of the graphene layer conforming to the substrate corrugations, where h is the distance between the middle planes of graphene and the substrate, λ is the groove wavelength and A_g and A_s are the corrugation amplitudes for graphene and the substrate respectively. With λ/A_s being a good measure of the surface roughness, Figure 2.7. (b) shows the effect of the surface roughness on the conformity of graphene. For a given interfacial bonding energy, there exists a threshold roughness above which, the transferred graphene layer lays flat on top of the substrate (i.e. $A_g/A_s = 0$).

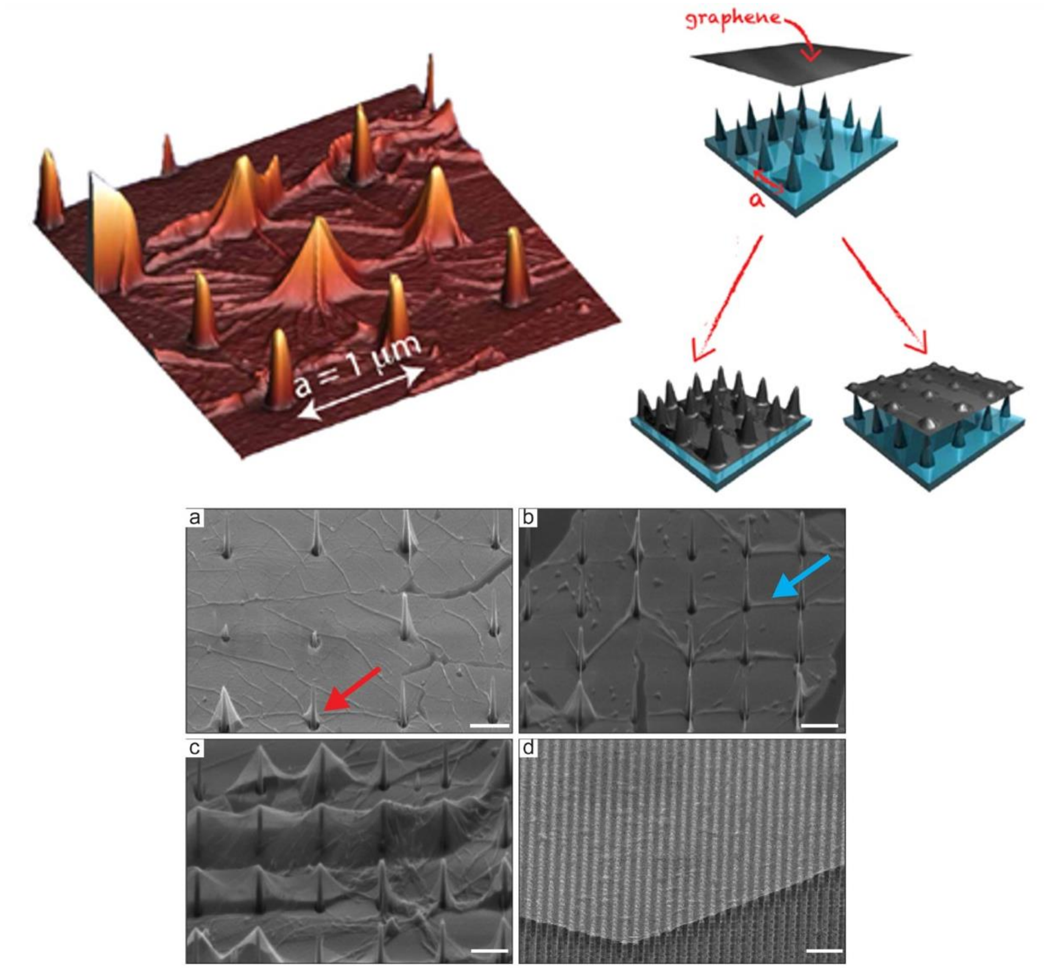

Figure 2.6. Graphene transferred on nanopillars. Image in top left shows the AFM micrograph of graphene on SiO_2 nanopillars. The top right schematics show that depending on the properties of the substrate, a transferred membrane of graphene can either conform or lay flat on top of the pillars. Figures **(a-d)** show SEM images of transferred graphene on surfaces with different densities of nano pillars (Scale bar is 2µm). These images display that the conformity of graphene to the substrate, greatly depends on the roughness and morphology of the surface and can range between complete conformation (a) to lying flat on top of the highest points, with minimal contact with the substrate. Reference [52]

In the scope of this thesis, with the main focus being the substrate induced effects in the carrier and phonon relaxations in graphene, the adhesion of graphene to the substrate is of utmost importance. With the graphene-substrate phonon interactions being an important factor, the roughness of the surface plays a critical role in the conformation of graphene to the substrate and enhancement of the graphene-substrate phonon coupling. As a result, we took extra measures to ensure that all studied substrates in chapter 3 are finely **polished to a sub nm surface roughness** for accurate comparison of the dynamics.

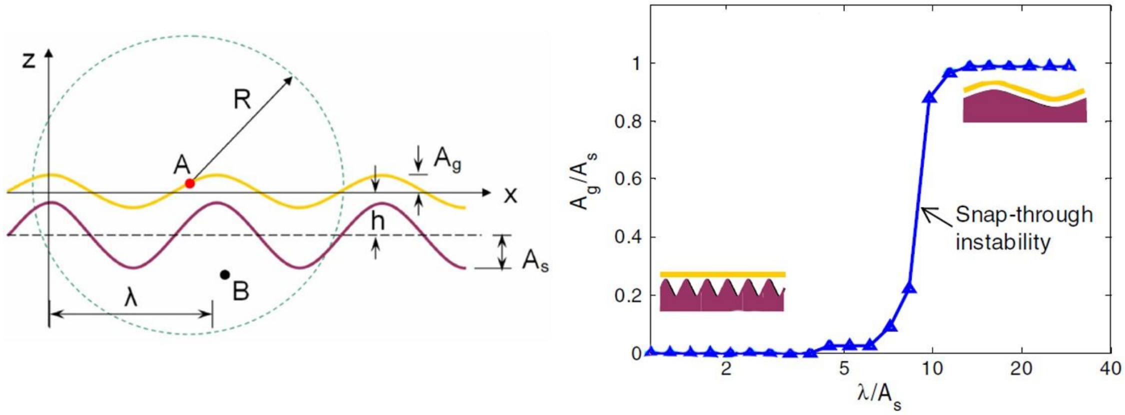

Figure 2.7.(a) Schematics of graphene conforming to the underlying substrate with sinusoidal surface grooves. Point A denotes a carbon atom in graphene and B denotes a substrate location within distance R of point A. **(b)** Shows A_g/A_s as a function of λ/A_s. The inset displays the two distinct states of the graphene morphology on a given substrate.[51]

To characterize the polished sample roughness, we used a Zygo optical profiler. Optical profilometry (OP) is an interference microscopy technique that is used to measure height variations with up to sub nm resolution. The advantage of an optical profiler over AFM in this case is the $cm\ x\ cm$ scanning range for OP as opposed to the maximum

$100\mu m\ x 100\mu m$ spatial range offered by AFM. Fig 2.8. (c) shows the roughness profile for one of our single crystalline diamond samples used in Chapter 3.

2.5.2. Substrate cleaning

To eliminate any contaminations which might reside on the substrate, prior to the graphene transfer, we used a Piranha cleaning method for all samples except diamond plates where in addition to the Piranha cleaning, an RCA cleaning method was used. The RCA cleaning method was first developed by Werner Kern while working for Radio Corporation of America, hence the name RCA. The three-step sequential method involves (step1) removal of organic material from the surface (step 2) oxide strip (step 3) ionic clean. Our XPS measurements show that the RCA method, effectively removes the Si particles from the diamond surface. To avoid compromising the sub nm polish on the quartz and sapphire samples, we used a Piranha etch method which involves a mixture of sulfuric acid (H_2SO_4) and hydrogen peroxide (H_2O_2) to effectively remove organic contaminants.

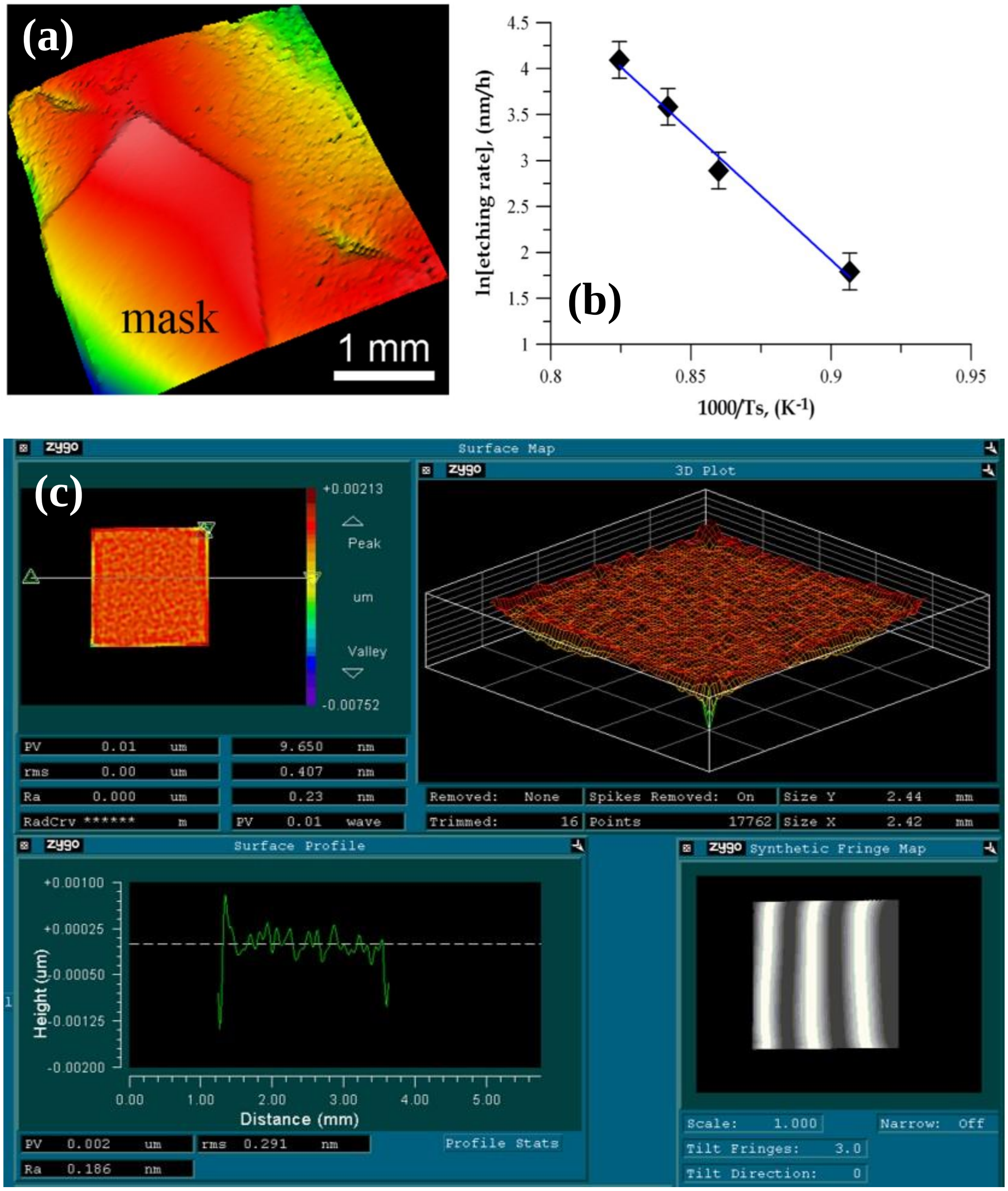

```
PV       0.01    um      9.650   nm
rms      0.00    um      0.407   nm
Ra       0.000   um      0.23    nm
RadCrv ******    m   PV  0.01    wave

Removed:    None   Spikes Removed:  On   Size Y   2.44  mm
Trimmed:      16   Points        17762   Size X   2.42  mm

PV  0.002  um    rms  0.291  nm
Ra  0.186  nm

Scale:          1.000   Narrow:  Off
Tilt Fringes:     3.0
Tilt Direction:     0
```

Figure 2.8. (a) Zygo interferometer image of the etched diamond sample that has been exposed to hydrogen plasma treatment. The smooth section represents the location at which the diamond surface was protected from plasma using a mask. **(b)** The plot of the etching rate versus inverse of the temperature for (100) face of single crystalline diamond. [54] **(c)** Optical profilometry mapping of the (100) face of single crystalline diamond. The mapped area is 2.4 x 2.4 mm and the RMS surface roughness is ~ 0.4 nm.

2.5.3. Passivation of the diamond samples

Although high sp^3 content diamond is known to be fairly non-reactive, the dangling carbon bonds on the surface of the diamond will react to the elements present in the ambient air and the growth chamber, rendering different terminations such as oxygen, nitrogen, hydrogen or silicon. To obtain a controllable and stable passivation of the surface, we use hydrogen plasma to hydrogen terminate both our single crystalline and poly crystalline diamond substrates. After the acid cleaning, we use a microwave plasma system at a temperature of $600^{\circ}C$ with a hydrogen flow of $50\ sccm$ at a chamber pressure of $30\ mbar$ for 15 mins. This process ensures a very clean diamond surface without any hydrocarbons, impurities or oxygen remaining from the oxidation of the surface from the acid cleaning procedures.

Hydrogen plasma treatment can result in fine etching of the diamond surface and inevitably roughening the polish. As seen in Figure 2.8. (a) and (b), Ivanov et al. showed that the hydrogen plasma etching rate of diamond (100), increases exponentially with increasing substrate temperature. [54] We optimized the mentioned etching times and substrate temperatures carefully to not compromise the sub nm polish on our diamond surfaces.

2.6. Characterization

2.6.1. Visibility under optical microscopy

One of the underlying factors expediting the growth of the graphene research was the fact that this atomic layer of carbon, can actually be visualized under an optical microscope if it is prepared on the right substrate with a certain thickness of SiO_2.[55] The visibility of graphene strongly depends on the light wavelength and the thickness of the SiO_2 layer.

Due to the interference between the multiple reflections from the interfaces of air and $SiO_2$and SiO_2/Si, it is possible to correlate the visualized color to the thickness of graphene. Depending on the relative distance, the interfering light paths will experience relative phase shifts. Consequently, when the thickness is varied by a fraction of a wavelength, it can be distinguished and detected by sensitive human eye.[56]

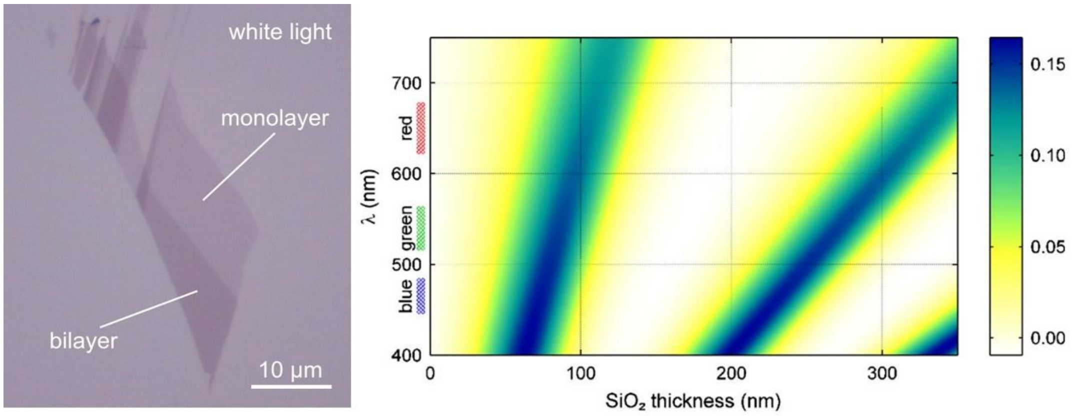

Figure 2.9. (Left) Exfoliated mono and bilayer graphene transferred on SiO2/Si substrate and characterized under white light where the optical contrast provides a quick method to identify layer number**.**[189] **(Right)** Contrast plot of light wavelength versus the thickness of the SiO_2 layer. As one can see, at 300 nm thickness the visibility of graphene is strongest for green wavelength which human eye can detect easily.[55]

This also emphasizes the role played by the wavelength of the light used for detection. As one can see from Figure 2.9, the common 280-300 nm SiO_2thickness used for SiO_2 on Si wafers in graphene research, has been optimized to provide maximum contrast for green wavelengths which human eyes are most sensitive to.[55] If we were not relying on the simplicity and ease of optical microscopy, detection and identification of layer numbers in graphene using other methods such as AFM or TEM with their very small throughput, would have been extremely difficult and possible only in very small scales. Although we use optical microscopy for detection and visualization of graphene in this thesis, Raman spectroscopy provides a more reliable method for layer number identification and can also provide a direct method to estimate strain and doping of the graphene samples.

2.6.2. Raman spectroscopy

Raman spectroscopy is the inelastic scattering of photons by phonons, first discovered in 1928 by C.V. Raman, who two years later won a Nobel Prize for this exact discovery. Almost a century later, in the boom of 2D materials, Raman spectroscopy is a widely common characterization technique used for identifying graphene layer number, strain and electronic doping. When light interacts with a crystal, depending on the energy band structure of the matter and the wavelength of the light, a fraction of the light gets transmitted, reflected, scattered or absorbed. Rayleigh scattering is an elastic scattering process where the radius of the scatterer is smaller than the wavelength of the light and the scattered photons will have the same energy as the incident photon. This phenomenon is responsible for the blue color of the sky where light from the sun is incident on the air molecules and is scattered elastically. The strength of Rayleigh scattering depends on the 4th power of the frequency, hence, the blue wavelength is dispersed more strongly than other wavelengths.

Rayleigh scattering will always accompany Raman scattering and is usually about 3 orders of magnitude more intense; therefore, its separation from Raman signal was one of the obstacles for commercialization of Raman spectroscopy. However, after the invention of laser as a monochromatic light source and reliable selective filters, Raman spectroscopy is now a ubiquitous technique for characterization of different materials.

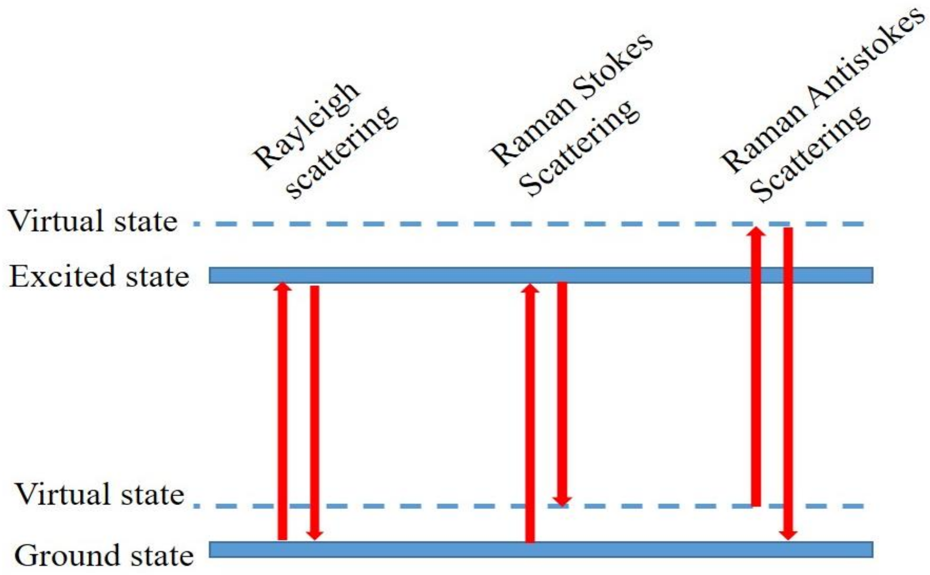

Figure 2.10. Schematics of elastic and inelastic scattering.

The shift in the energy of the incident and inelastically scattered light can be lower (Stokes) or higher (Anti-Stokes) depending on the vibrational state of the molecules and can be expressed in terms of wave numbers associated with specific vibrational levels. (Figure 2.10) Stokes phenomena is much more intense than Anti-Stokes due to the fact that only molecules that are vibrationally excited prior to the excitation can give rise to Anti-stokes lines. As a result, Raman spectroscopy is usually performed measuring the Stokes Raman scattering by plotting the intensity of the scattered light as a function of the difference between the scattered photon energy and the incident photon energy. This energy shift is commonly known as the “Raman shift” and although the units of this quantity should be in units of energy, historically, in the spectroscopy culture, chemists and spectroscopists use wave numbers υ expressed in units of reciprocal centimeters (cm^{-1}). This is defined by υ $= v/c = 1/\lambda$ where c is the speed of light in cm/s and λ is the wavelength in cm and can be readily converted to meV using the relation $1\ meV = 8.0655447\ cm^{-1}$. Since in the NIR and UV spectral range, the energy of the laser is much larger than the phonon energy, the primary scattering mechanism is photon-electron coupling rather than photon-phonon coupling specifically for graphene with its non-polar nature. Therefore, by studying the Raman spectrum of graphene, we can get an accurate insight into the behavior of the electrons.[57]

In 2006, two years after the successful exfoliation of single layer graphene from bulk graphite, Ferrari et al. presented Raman spectroscopy as a powerful tool for characterization of layer numbers in graphene. [58] In the following years, significant advances were made to use Raman spectroscopy to characterize defect concentration[59], [60], doping[61]–[63] and strain[64]–[66] in graphene. The absence of a band gap and the resonance of all incident wavelengths, results in this spectroscopy technique being a powerful tool to study both atomic and electronic structure of graphene. Raman scattering process is very much dependent on the interaction of electrons and phonons. Therefore, any changes in the electronic properties of graphene due to the magnetic or electric field or doping, will accordingly affect the intensity, position and width of the observed Raman peaks. [35][36]

2.6.2.1. Phonons in graphene

To analyze the Raman spectrum of graphene, we need to understand the electron-phonon coupling phenomena and the phonon dispersion curves in the reciprocal space. Phonon dispersion spectra are essential in understanding the fundamental properties of crystals such as heat capacity, velocity of sound in the crystal, thermal conductivity and more importantly electron- phonon and phonon-phonon interactions. As a result, great efforts have been made to understand the phonon modes of graphene and their dispersion. [69][70][71][72]

Since the unit cell of graphene consists of two non-equivalent atoms of carbon, the phonon dispersion curve of graphene has 6 branches: three optical phonon branches (O) and three acoustic phonon branches (A). One branch from each family corresponds to the out of plane vibrational mode (Z) and the two other modes correspond to the in-plane modes: transverse (T) and longitudinal (L) which are related to the atomic vibrations perpendicular or parallel to the vector between the two carbon atoms which form the unit cell.

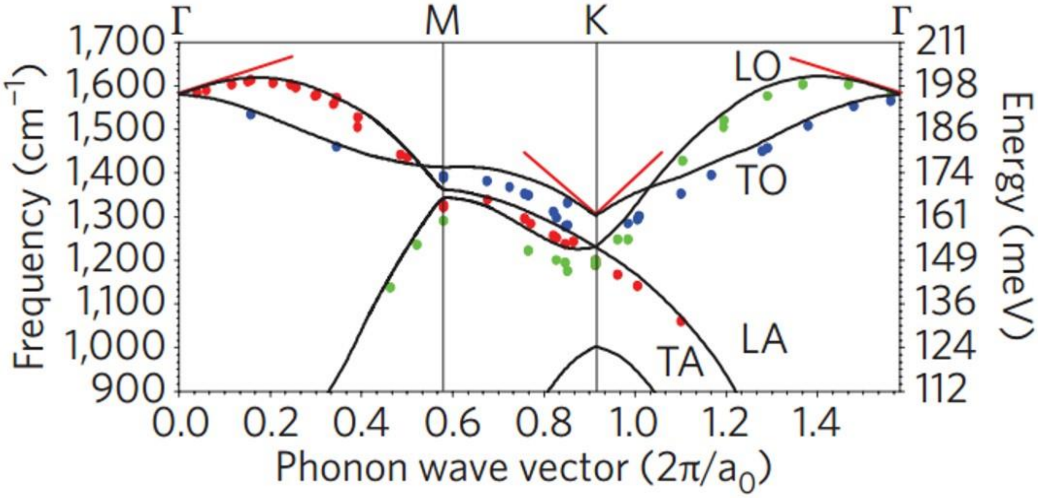

Figure 2.11. Phonon dispersion curve for single layer graphene, red lines represent Kohn anomalies. Reference[190]

The low mass of the carbon atom and the strong sp^2-bonds, lead to lattice vibrations of extremely high energy. Figure 2.11 shows that the optical phonon energy of graphene at the Γ point is close to $0.2\ eV$. The optical phonon branch in the IV group semiconductors is not infrared active but due to the inversion symmetry, it is strongly Raman active. For odd parities, the optical lattice modes at $\vec{q} = 0$ can be accurately studied by infrared spectroscopy. Raman spectroscopy is not only sensitive to even parity modes, but also in the case of graphene, is highly successful in extracting the optical phonon properties. It is widely used to determine the number of layers, doping, strain [64]–[66] and stacking order in graphene.[59]–[63] Since the wave vector of light is much smaller than the BZ dimensions, the momentum conservation law dictates that the wave vector of the phonons created or absorbed, should be small as well. As a result, the wave vector of the phonons probed by infrared spectroscopy or Raman spectroscopy is close to $\vec{q} = 0$. [26]

To obtain information about the phonons *throughout* the BZ for crystals such as diamond and graphite, one can use neutron spectroscopy.[73] This technique uses low energy, thermal neutrons with wavelengths comparable to that of the lattice constants, where the inelastic scattering events with the lattice, results in a large momentum transfer to the neutrons. Although this technique is less accurate than Raman spectroscopy, the wide range of momentum values for neutrons provides an opportunity to probe a wide range of phonon energies in the BZ.

Since the acoustic phonons are the main heat carriers in room temperature for the carbon family [74], acoustic phonon branch characteristics are usually obtained from the thermal conductivity measurements. Acoustic phonon transport and evidently heat transfer in semiconductor nanowires or thin films is inferior to their 3D bulk counterparts due to the increase in phonon boundary scattering and changes in the phonon dispersion and density of states.[75][76] However, it has been shown that the phonon transport properties in graphene such as dispersion relations and scattering rates, are quite different compared to bulk graphite, leading to an extremely high intrinsic thermal conductivity for graphene.[77]

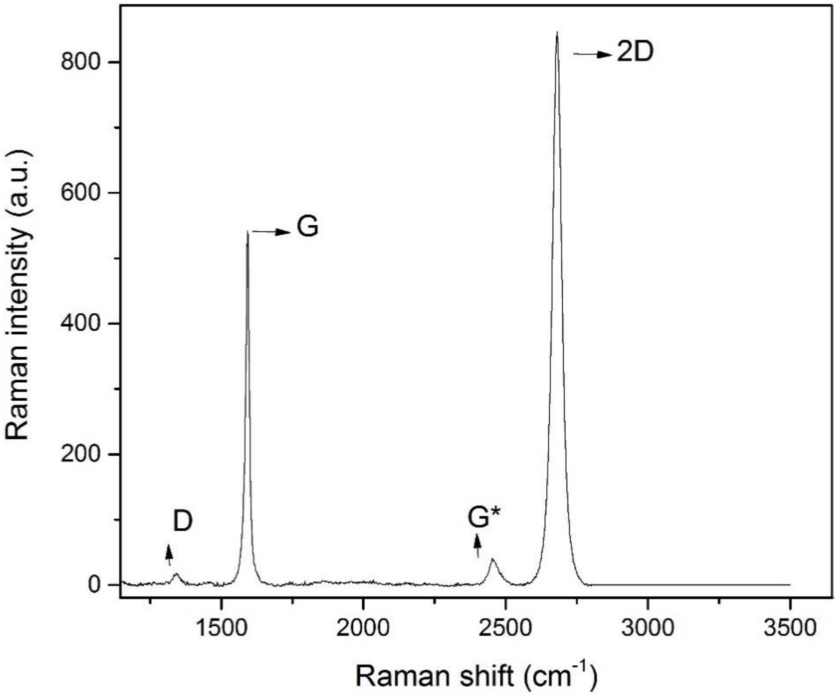

Figure 2.12. Raman spectrum of single layer graphene on quartz and the associated signature peaks.

Both electrons and phonons are believed to participate in the heat transfer process in crystals so that $K = K_p + K_e$, where $K_p$and K_e are contributions due to phonons and electrons respectively. In metals or heavily doped semiconductors, the large number of free carriers results in the dominance of K_e and therefore can be calculated by measuring the electrical conductivity through: [74]

$$\frac{K_e}{\sigma T} = \frac{\pi^2 K_B^2}{3e^2}$$

with K_B being the Boltzmann's constant, σ the conductivity of graphene and e the electron charge. The strong sp^2 bonds in graphene result in a large in-plane phonon group velocity and although graphene is considered a semi-metal, the heat conduction is believed to be mainly due to the acoustic phonons.[78] The relative contribution of different phonon branches to the thermal conductivity of graphene is still open for debate.

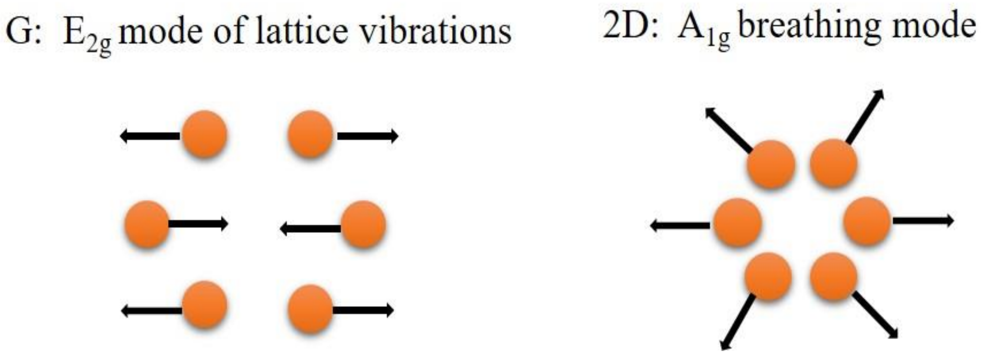
G: E_{2g} mode of lattice vibrations

2D: A_{1g} breathing mode

Figure 2.13. Vibrational modes G and 2D of single layer graphene.

2.6.2.2. Raman peaks of graphene

The prominent Raman peaks of graphene are positioned at $\sim 1580\ cm^{-1}$ and $\sim 2680\ cm^{-1}$ for G and 2D bands respectively. In the presence of disorder, there will be a 3rd peak at $\sim 1350\ cm^{-1}$, a weaker peak at $\sim 2450\ cm^{-1}$ can also be present. (Figure 2.12) The in-plane phonon dispersion curve of graphene is very similar to graphite; therefore, similar peaks are observed in graphite.

As seen in Figure 2.11, the in-plane LO and TO modes at the Γ point of the Brillouin Zone are degenerate. The G peak in graphene corresponds to the high frequency E_{2g} mode, defined by the group theory. [79] The second Raman active mode 2D, is an A_{1g} breathing mode at the K point of the BZ and comes from the TO branch. (Figure 2.13) The discontinuity at the derivation of the phonon dispersion curve at the Γ point of the LO branch and also at the K point of the TO branch are called Kohn anomalies (as represented by the red lines in Figure 2.11). They correspond to a sudden decrease of the lattice vibration due to the screening from the electrons.[80] The 2D and D bands are double resonant processes and are strongly dispersive with excitation energy due to this Kohn anomaly at K point. The slope of the anomalies in the branch can provide direct information on the electron-phonon coupling (EPC). There is a direct relation between the slope and the electron-phonon coupling strength in graphene, therefore EPC is much higher in the K and Γ points than anywhere else in the BZ of graphene and the Raman peaks corresponding to these modes are therefore much stronger.

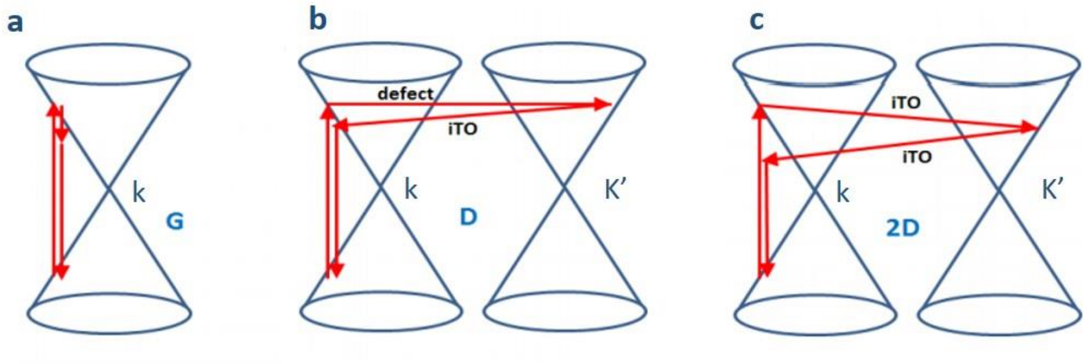

Figure 2.14. Schematics of Raman processes for activation of **(a)** G, **(b)** D and **(c)** 2D peaks in single layer graphene. Adapted from reference [190]

Figure 2.14 depicts the Raman processes for G, 2D and D bands of graphene. The G peak corresponds to a single-phonon process at the Γ point and is due to the in-plane stretching mode of the carbon-carbon bonds. (Figure 2.14. (a)) When a photon of energy E_{pht} is absorbed by graphene, it creates an electron hole pair with an energy E_{e} , E_{h} = E_{pht} /2. The probability of this process is higher at a wave vector k of the BZ that can guarantee a resonant absorption. In this Raman process, the electron loses energy to emit a phonon of energy E_{phn} with wave vector $q = 0$. From this virtual state, the electron then recombines with the hole and emits a photon that has a lower energy than the initial energy E_{pht} . Both momentum and energy are conserved during this whole process. The intensity of the G peak which is a signature of the carbon allotrope family, is higher when the electron-phonon coupling is stronger.

The 2D peak is usually the most intense of all graphene peaks. This double resonant process was first introduced in 2000 and is explained as an intervalley process involving two phonons,[81](Figure 2.14. (c)) where absorption of a photon results in the generation of an electron hole pair. The electron then loses energy E_{phn} to a phonon of the wave vector $q = K$ and the hole loses energy E_{phn} to a phonon with wave vector $q = -K$. Finally, the electron and hole recombine and a photon is emitted that is less energetic than the incident photon. Both energy and momentum are conserved in this process. Since this Raman process does not involve virtual states, it is therefore triple resonant and explains the intense nature of the 2D peak compared to the G peak. As discussed in chapter 1, graphene has a universal absorption in a wide spectral range covering visible and NIR wave lengths. This fact results in the dispersive nature of the frequency of the 2D peak in graphene. Therefore, since all energies are resonant for different excitation energies, the electron wave vector and hence the phonon wave vector will be different. As seen in Figure 2.11, the phonon branches at K point are quite steep and linear, which result in a considerable change in the phonon energy and consequently, the position of the 2D peak at a rate of $100\ cm^{-1}\ /eV$.[82]

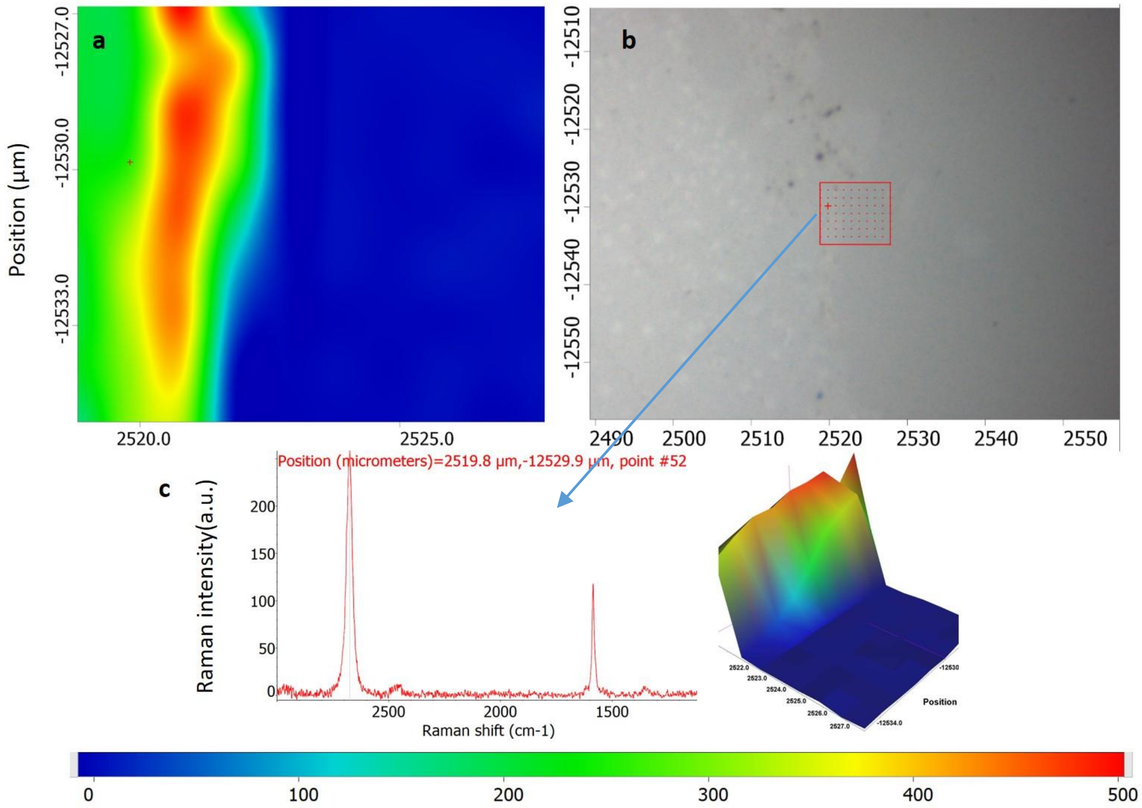

Figure 2.15. Spatial mapping of the 2D Raman peak of graphene transferred on sapphire. The image on the top right **(a)** is the optical image of the sample with the red square being the mapped area shown in **(b),** One can see the edge of the transfer from the optical image with graphene coverage on the left and bare sample on the right**.** (The intensity scale bar is shown in the bottom of the figure.) **(c)** Raman point spectrum from the location marked with the arrow.

Figure 2.15 shows a Raman point mapping of the 2D peak of graphene along the edge of graphene transferred on sapphire. The 2D peak intensity is a good measure of the uniformity of the coverage and mapping of the area with adequate spatial resolution provides a quick and easy way to locate graphene on transparent substrates.

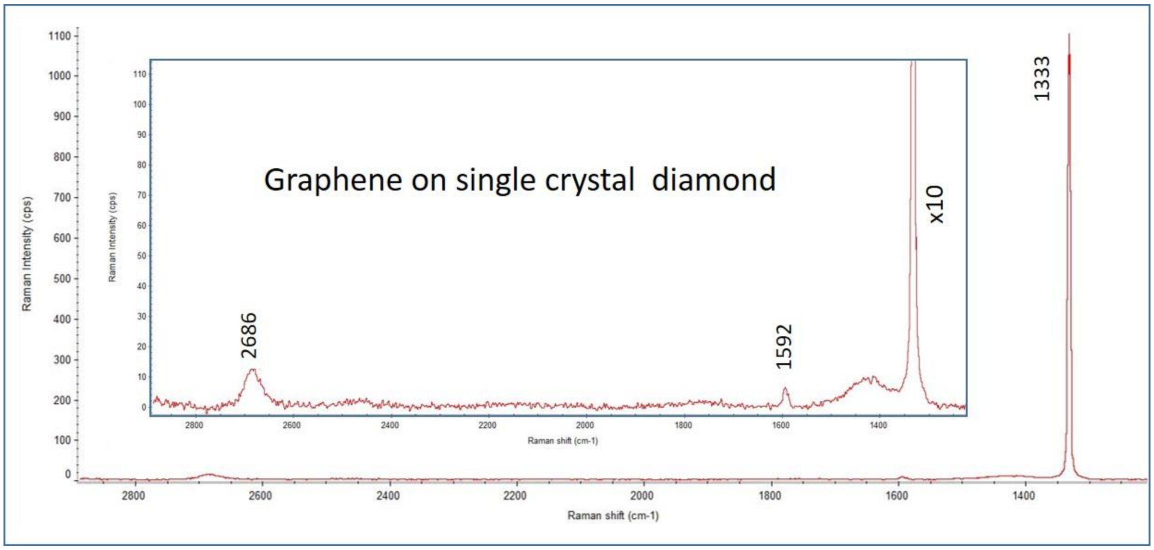

Figure 2.16. Raman spectrum for graphene transferred on single crystal diamond where the 2D and G peaks of graphene are dwarfed by the 1333 peak of diamond. The inset shows a smaller range of intensity for better identification of the graphene peaks.

The D band is also a double resonant process arising from the breathing mode of the hexagonal rings and requires a defect to be activated; therefore, the D peak is not present in pristine graphene. (Figure 2.14. (b)) A much less pronounced peak $\sim 2450\ cm^{-1}$ can also be present in graphene. This peak was first reported in graphite [83] and is often referred to as G*. Many different explanations have been made throughout the years to explain the origin of G*. These explanations range anywhere from contribution of LA phonon branch around the Brillouin Zone edge[84] to a non-dispersive overtone of the LO branch at K point[85] or a combination of the LA and LO phonons.[82] The origin of this band is still under debate to this date.

Figure 2.16 shows the Raman spectrum of a single layer graphene transferred onto (100) face of single crystal diamond. The signature peaks of graphene: G and 2D, are dwarfed by the 1333 cm^{-1} peak of single crystalline diamond corresponding to the vibration of the sp^3 diamond lattice. The inset shows the same spectra at 10x less intensity where the peaks of graphene can be identified.

2.6.2.3. Nomenclature

The nomenclature for the Raman spectra of graphene and graphite can be confusing due to the historical evolution of this technique's development. In 1977 Vidano et al. introduced the first Raman nomenclature, where they named the observed peaks at ~1580 and ~2700 cm^{-1} of the pristine graphite, G and G′ respectively. For defected graphite, they observed peaks at ~1350 and ~1620 cm^{-1} which they named D and D′.[86] The names were chosen based on: G standing for graphite and D standing for Disorder. Many different speculations were made for the origin of the D band, but in the turn of the 21st century, Thomsen et al.[81] offered an explanation based on double resonance. In this explanation, the photons excite electrons with a wave vector k, these electrons then go through electron-phonon scattering with exchanging momentum q near the K point, which is then followed by a defect back scattering of the electron to the initial momentum state k which ultimately results in the recombination of the electrons hole pair. In this process a defect is needed and while there is considerable exchange of momentum for phonons, the energy stays conserved. At this date, D peak is believed to be activated by the double resonance process and is due to the TO phonons around the K point. The ~2700 cm^{-1} peak is no longer referred to as G′ since it had nothing to do with G in terms of symmetry or Raman processes and is in fact a D overtone; as a result, in the more recent years this band has been mostly referred to as 2D.

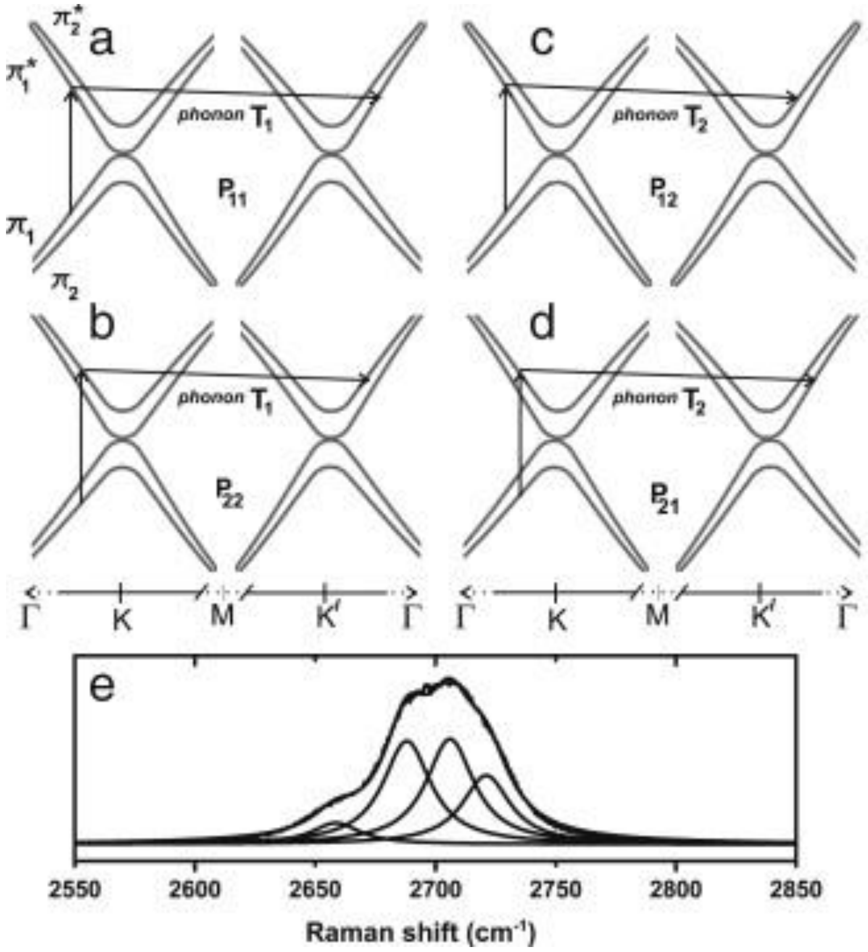

Figure 2.17. (a-d) Schematics of phonon dispersion in bilayer graphene near the Dirac cone for both π_1 and π_2 bands showing the four different double resonance processes involved in Raman scattering in bilayer graphene**. (e)** The measured 2D Raman peak of bilayer graphene with four fitted Lorentzians. Reference [191]

2.6.2.4. Raman spectroscopy and graphene layer number

The distinct Raman fingerprints for single layer, bi-layer, and few-layer graphene have been one of the facilitating factors in the expansion of graphene research. Before the introduction of Raman spectroscopy as a layer identification tool in 2006 by Ferrari et al.[58], the only method to distinguish between single layer and few layer graphene was Atomic Force Microscopy (AFM). Despite the success of AFM, the low throughput and the problems arising from the existence of wrinkles and folds in graphene, put limitations on this method. The resonant nature of the 2D peak in graphene provides a unique opportunity to use Raman spectroscopy as a fast, non-destructive and high throughput identification tool for graphene layer number.

Figure 2.17. (a-d) show the band structure and the double resonant processes for bi-layer graphene (BLG). The evolution of the electronic bands with the layer number and the differences in the band structure of SLG and BLG translate into a distinct difference in their Raman fingerprint. Unlike the linear cone-like band structure of single layer graphene around the K point, the band structure of bi-layer graphene is comprised of four parabolic bands.[87] The interaction of the planes in graphene cause the π and π^* bands to divide into four bands. The incident photon can only couple to two of these bands but the TO phonons can couple to all four. Consequently, in BLG, the 2D peak is a superposition of all these scattering processes and the sum of these four Lorentzian line-shapes, as opposed to SLG with a single symmetric Lorentzian peak of a FWHM ~30 cm^{-1}. (Figure 2.17. (e)) This approach can be extended to multiple layer detection in graphene. Figure 2.18 shows the projected Raman map onto the optical image of a hole in the single layer graphene membrane.

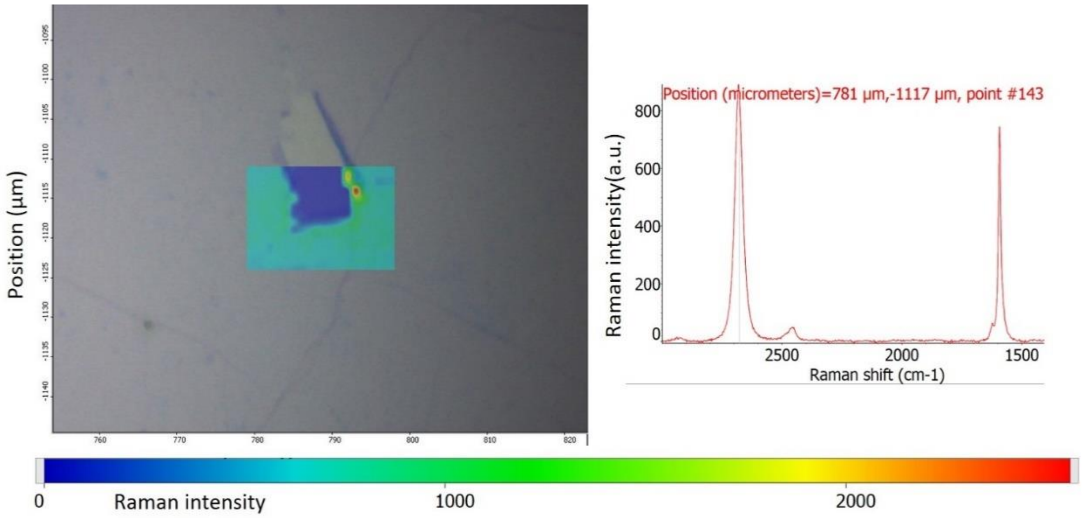

Figure 2.18. Projected 2D Raman map of single layer graphene onto the corresponding optical image. The blue color shows the area with no graphene and the green area shows the coverage of the single layer graphene. The image on the right is the Raman spectrum of an individual mapped point showing the 2D peak with single Lorentzian lineshape indicative of mono layer graphene.

2.6.2.5. Raman spectroscopy and layer stacking

In Bi-layer graphene, the positioning and the stacking order of the two layers, determine the associated vibrational and electronic properties of graphene. In principle, any relative orientation of the graphene layers is possible; however, some stacking orders are much more common. AB or Bernal stacked graphene with an inter-planar spacing of 0.335 nm, is the most common and well-known stacking order in graphene. (Figure 2.19. (c)) [88]

Figure 2.19. (b) shows an AA stacked graphene which is not energetically stable and hence not normally formed in graphitic structures. In the case of no rotational order, the stacking is referred to as Turbostratic stacking. (Figure 2.19. (d)) As discussed, due to the differences in the electronic band structure of the different stacking orders, the Raman 2D

peak of graphene is highly sensitive to the number of layers and the stacking forms. Thus, a detailed study of the 2D peak shape can shed light on the interlayer interactions in Bi-layer and Multi-layer graphene.

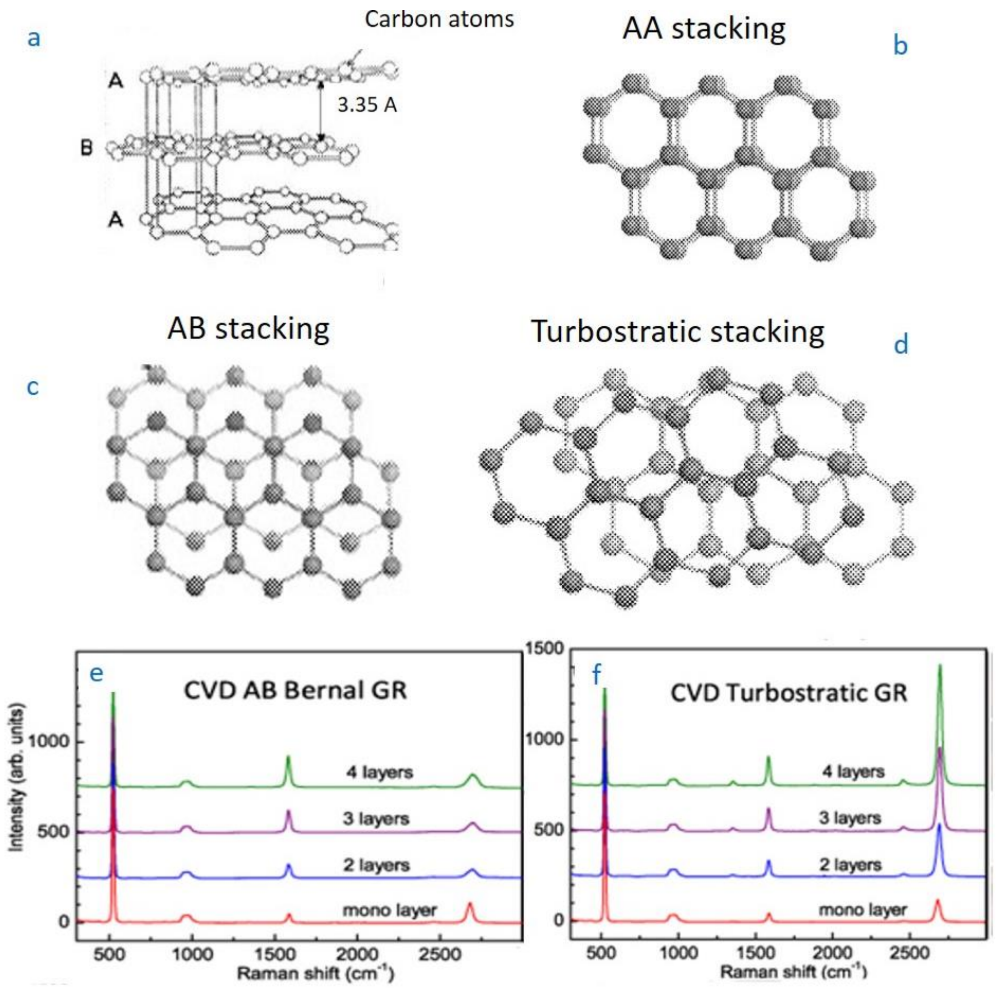

Figure 2.19. (a) Planar view of stacked layers of graphene with AB symmetry. **(b)** Schematics of AA stacking. **(c)** AB or Bernal stacking. **(d)** Turbostratic graphene with no stacking order. [88] **(e)** Raman spectrum for different CVD graphene layer numbers with AB or Bernal stacking. **(f)** Turbostratic stacking. [90]

Turbostratic few layer graphene (FLG) has been shown to possess a *single* Lorentzian 2D peak. [89] Hence, care should be practiced using the single Lorentzian 2D peak as a proof of single layer graphene identification. The similarity to the SLG Raman fingerprint can be understood based on the very weak coupling of the stacked layers in Turbostratic graphene as opposed to AB stacked graphene. [90] However, the FWHM of the 2D peak of Turbostratic graphene is almost double the FWHM of SLG and the position of the peak is also shifted by ~20 cm^{-1}. (Figure 2.19. (e) and(f)) In terms of differentiating Bernal and Turbostratic graphene, Hwang et al. showed that the area ratio of the 2D and G bands could be an effective way of identifying these stacking orders. [90] We use the same method to identify the stacking order and distinguish between the Turbostratic and AB stacked graphene in free standing curled graphene ribbon structures discussed in chapter 4.

2.6.2.6. Raman spectroscopy and defects

In the presence of defects, single phonon scattering events can occur without violating the Raman selection rules. This elastic scattering by a lattice defect, happens in both D and D′ peaks where D is an inter-valley process involving TO phonons near K point and D′ is an intra-valley process involving LO phonons near Γ point of the BZ. Due to the sensitivity of the D peak to the defects and dislocations of the carbon lattice, the existence of edges and grain boundaries in the graphene membrane, are reflected in the Raman D peak. As a result, Raman spectroscopy is an effective and non-invasive tool that can be used to identify (as well as quantify) defects in the lattice of graphene.

In the ground-breaking work of Tuinstra and Koenig, it is shown that the ratio of the D peak to the G peak intensity is inversely related to the crystal size of graphene (L_a). [91] This relationship was further improved by Cançado et al. by including the influence of the excitation energy λ:[92]

$$\frac{\boldsymbol{I(D)}}{\boldsymbol{I(G)}} = \mathbf{2.10^{-10}}\boldsymbol{\lambda^4}\frac{\mathbf{1}}{\boldsymbol{L_a}}$$

The ratio of the D to G peak amplitudes, is commonly used as a quick means of recognizing and estimating defect concentrations in graphene. In Figure 2.20 we show the varying stages of the damage in the planar structure of graphene as a graphene sample is exposed to a high fluence laser for 60 seconds. One can see that the amplitude of the D peak and $\frac{\boldsymbol{I(D)}}{\boldsymbol{I(G)}}$ is increased as time goes by, which means that the graphene membrane is damaged and possibly oxidized in the presence of a high intensity laser beam.

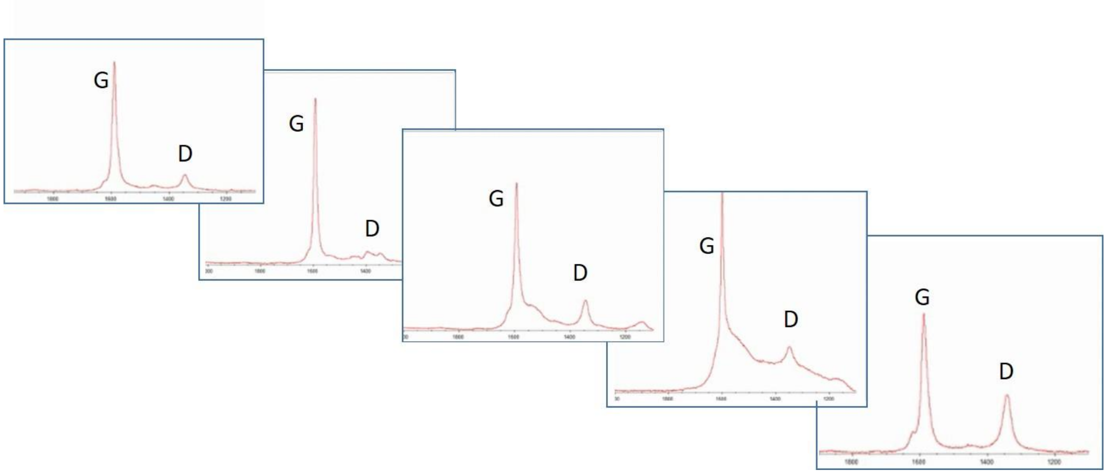

Figure 2.20. Snapshots of the evolution of the Raman spectra of graphene, taken from a video, as the sample is exposed to high fluence laser over a period of 60 seconds. (left to right) It can be seen that the D peak starts to grow in intensity and after 60 seconds, the G to D ratio becomes larger indicating that the sample was damaged by the intense laser beam.

2.6.2.7. Raman spectroscopy and doping in graphene

One of the most useful aspects of Raman spectroscopy in graphene research is the sensitivity of G and 2D peaks of graphene to the electronic doping. In 2008 Das et al.[62]

used a top gate FET to change the doping levels both below and above the Dirac point and performed in situ Raman measurements to monitor the change of the Raman peaks as carrier concentration is changed.

Applying a gate voltage (V_G), creates a potential difference between the gate electrode and graphene, in which case, the additional carriers will change the positioning of the Fermi level. The Fermi energy in graphene changes as: $E_F(n) = \hbar|v_F|\sqrt{\pi n}$ where v_F is the Fermi velocity and n is the electron concentration in units of cm^{-2}. Equation below shows the dependence of n on the applied Top gate voltage (V_{TG}). [62]

$$V_{TG}(volts) = 1.16 \times 10^{-7}\sqrt{n} + 0.723 \times 10^{-13}n$$

As shown in Figure 2.21, both the FWHM and the position of the G peak are dependent on the doping levels where, for both electrons and holes, a G peak stiffening and a decrease in the line-width is observed. Introducing excess carriers causes an expansion or contraction of the crystal lattice and results in a change in the equilibrium lattice constant, hence softening or stiffening of the phonons. This in turn results in a consequent shift of the G peak in graphene. The transition of the G peak to higher energies is believed to be due to the non-adiabatic removal of Kohn anomaly at the Γ point of the BZ.[93]

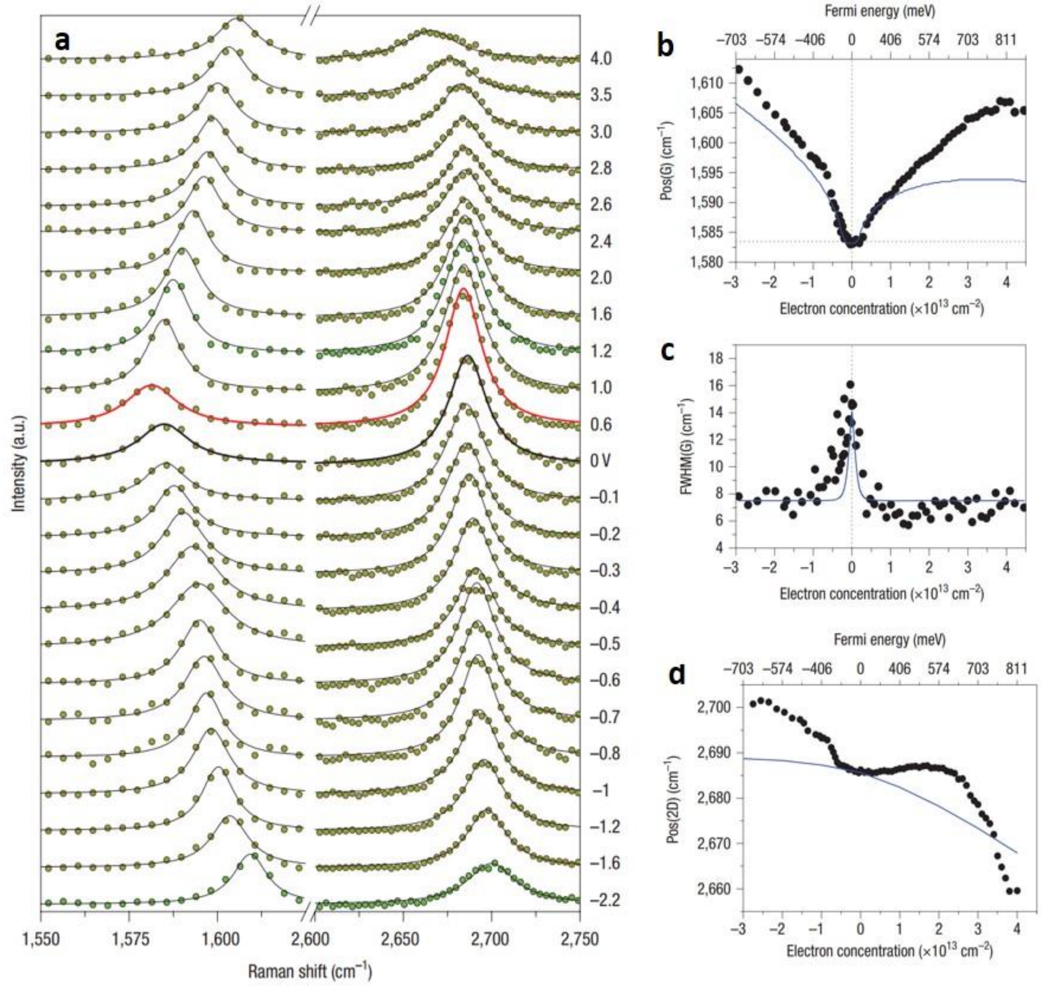

Figure 2.21. (a) Raman shift of graphene as a function of gate voltage, the black lines are lorentzian fits and the red line corresponds to the charge neutrality point. **(b)** Position of the G peak as a function of carrier concentration or change in Fermi level. **(c)** FWHM of the G peak as a function of carrier concentration. **(d)** Position of the 2D peak of graphene as a function of electron doping. Reference [192]

The decrease in the FWHM of the G peak is due to the removal of the phonon to electron-hole pair decay pathway and is based on the Pauli blocking and Pauli Exclusion Principle. [93] Although the G peak shift is a useful tool to estimate carrier concentration, it fails to distinguish between electron and hole doping in graphene. As shown in Figure 2.21. (d), the 2D peak of graphene appears to be a good measure of the character of the doping. The 2D peak shifts to lower energies for an increase in the electron doping and to higher energies for an increase in the hole doping.[62] These position changes are attributed to the change of the lattice parameters due to the excess charge and the consequent softening or stiffening of the phonons. The decrease in the intensity of the 2D peak for both electron and hole doping has been explained using the changes in the scattering rates of carriers.[94]

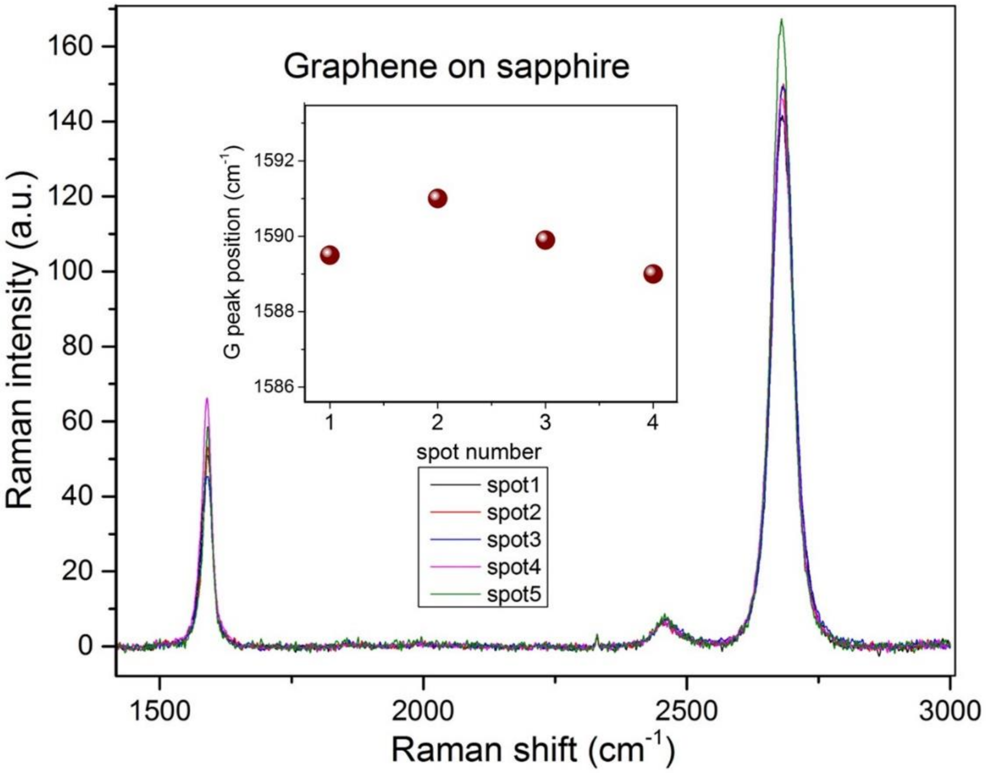

Figure 2.22. Raman spectra taken at different locations for graphene transferred on sapphire. The average G peak shift (inset) is used to estimate the doping of the sample corresponding to E_F= 0.27 ± 0.01 eV.

In the context of this thesis, we use the Raman shift of the G peak to estimate the electron/hole doping of graphene transferred on different substrates in chapter 3. Figure 2.22 shows the Raman spectra for different spots for graphene transferred on sapphire within the studied area of interest. The inset shows the position of G peak for each spot. We used the average value to estimate the change in Fermi level corresponding to $E_F = 0.27 \pm 0.01$ eV.

2.7. Conclusion

In this chapter we reviewed different methods for graphene synthesis and discussed an optimized CVD recipe for large area, single layer graphene growth. We further demonstrated an optimized fabrication and transfer process to minimize the PMMA residue and emphasized the importance of the substrate roughness. Finally, we discussed Raman spectroscopy as a means to deduce layer number, stacking order, defects and doping for graphene samples presented in chapters 3 and 4.

CHAPTER

3. RELAXATION DYNAMICS OF GRAPHENE ON DIFFERENT SUBSTRATES

3.1. Introduction

The unique 2D structure of graphene, the linear energy dispersion, high electron mobility and universal absorption in the visible-NIR spectral range, make graphene a desirable candidate for use in electronics and optoelectronics. [34][95] Although graphene's excellent properties have opened new avenues for improved performance and miniaturization of (opto)-electronic devices, the intrinsic properties of graphene are highly sensitive to the external environments. As a result, placing graphene on a substrate will inevitably affect both its equilibrium and non-equilibrium dynamics. Consequently, to enhance the performance of these high speed devices, one needs to understand the ultrafast carrier dynamics of graphene and the different *intrinsic* and *extrinsic* scattering mechanisms and energy relaxation pathways available through phonons of graphene and phonons of the substrate.

Ultrafast pump probe spectroscopy (UPPS) provides a powerful tool to mimic the behavior of hot carriers in high field FETs and subsequently monitor the relaxation of photoexcited electrons with a femtosecond time resolution which is far superior to what can be achievable by the most advanced electronics. In this chapter we study the effect of substrate on the femtosecond transient electron and phonon dynamics of single layer graphene using

UPPS and show that the temporal evolution of hot carriers in graphene differ *significantly* depending on the underlying substrate.

In the first part of this chapter, we will review the ultrafast dynamics of graphene and derive an expression for the optical conductivity (σ) in the NIR and visible spectral range. We then determine the transient transmission response of graphene on quartz under different excitation energies and photoexcited carrier densities and discuss the role of interband and intraband transitions. The second part of this chapter will be focused on the substrate dependent dynamics of graphene and the role of surface optical phonons as a prominent energy relaxation channel in polar materials. We believe that the fine polish and the sub nm roughness of our studied substrates (sapphire, quartz and single crystal diamond) enable a strong coupling between phototexcited carriers of graphene and surface optical phonons of the underlying substrate. In addition, the lower fluence regime used in our experiment, further highlights the impact of this additional energy relaxation channel on the reduction of the electronic temperature as well as modification of the carrier decay times.

We explain the observed substrate dependent dynamics using a multi-channel cooling picture, involving polar surface phonons of the substrate (SP), graphene's intrinsic optical phonons (IP) and their associated scattering rate and activation timeframe. The observed increase in the carrier relaxation times as the photoexcited carrier density is increased, further confirms the existence of an additional energy relaxation channel through phonons of the substrate which can compete with the intrinsic optical phonons to lower the transient carrier temperature and reduce the lifetimes of the intrinsic optical phonons.

3.2. Ultrafast pump probe spectroscopy of graphene

Since 2007, many different pump probe studies have been reported on single and multi-layer epitaxial, exfoliated and CVD graphene which sometimes resulted in contradictory arguments. It is understood that upon photoexcitation, the interaction of photons with hot carriers in graphene create an out of equilibrium distribution. The strong Coulomb induced interactions and the subsequent electron-electron collisions, result in an evolution towards a hot Fermi-Dirac distribution on a time window of tens of fs.[96][97][98][99] This quasi-thermal distribution subsequently relaxes to lower energies (mainly through phonon coupled channels), on a longer picosecond time scale.

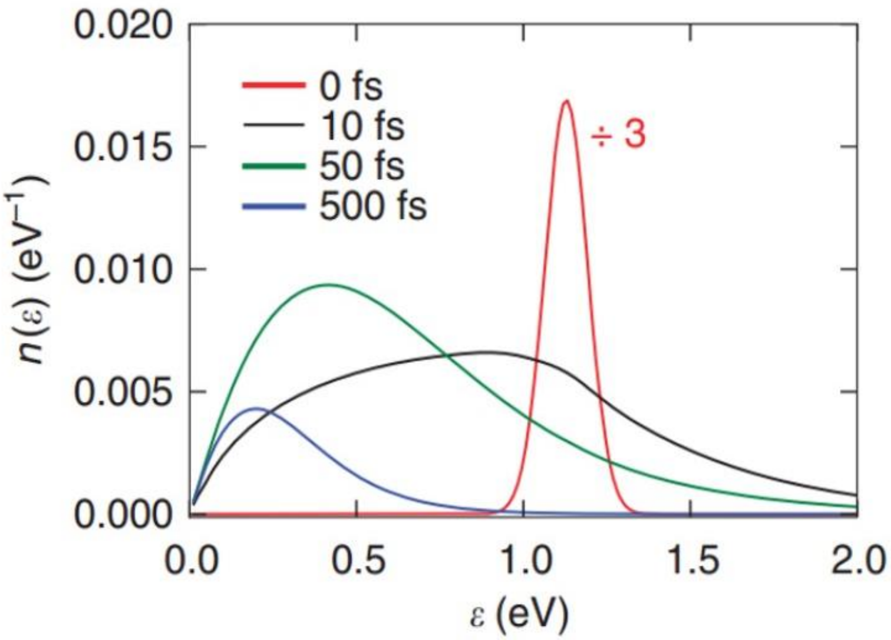

Figure 3.1. Time-evolution of the electron population per unit cell (in units of eV $^{-1}$) in sub picosecond time scale.[96]

The less explored, sub 100 fs non- equilibrium dynamics of graphene was experimentally studied by Brida et al. [96] where the role of Auger recombination and carrier multiplication in the thermalization process was highlighted. Due to the very fast Auger processes that bridge the conduction and valance bands on a very short time scale, the separation of chemical potentials for electrons and holes is considered insignificant in our measurements. [96][100]

Figure 3.1 shows the thermalization process for an extremely hot electron distribution (red curve) and the shifting of the electron population to lower energies as time evolves. One can see that the initial narrow hot distribution, broadens into a non-thermal distribution by $10\ fs$ (black curve), which then thermalizes into a Fermi Dirac distribution (green curve) and by $500\ fs$ starts to cool further down by coupling to phonons.

A uniform positive differential transient transmission (DTT) or a uniform decrease in absorption was first seen in epitaxial graphene by Dawlaty et al.[101] and ever since, has been reported by a number of different groups. [102][103][104] This positive peak in transmission, is attributed to the Pauli Blocking (PB) or bleaching of the interband transitions, where the time evolving *hot* carrier distribution discussed above, inhibits the absorption of the probe beam due to the band filling effects. As the distribution cools down, the peak of the distribution moves to lower energies and the absorption of the probe beam increases. [101][102][96]. Monitoring the femtosecond time evolution of the transmission response of graphene, enables us to directly measure the carrier density and carrier distribution as a function of time.

The cooling mechanisms for the carriers of graphene after photoexcitation, have been studied by many different groups. Wang et al.[102] studied the hot optical phonon dynamics and the different carrier cooling channels for multi-layer graphene grown on silicon face of SiC, carbon face of SiC and CVD graphene grown on nickel and transferred on quartz substrate. A biexponential decay was observed for all different samples, where the dynamics were explained based on the interband transition of the carriers and the subsequent decay of hot optical phonons into two acoustic phonons. As discussed earlier, during the rapid electron-electron scattering events, photo generated carriers thermalize within themselves on a very short timescale. [96][105] The thermalized carrier distribution then cools down through generation of optical phonons. This thermalized electron-optical phonon bath, subsequently cools down through lower energy acoustic phonons which presents a bottle neck for the energy relaxation and is apparent in the slower decay component of the dynamics.

The optical phonon emission rates: $R_{\Gamma e}(R_{Ke})$ due to the intraband intravalley (intraband intervalley) electron-optical phonon scattering at Γ (K, K') points can be defined as: [106]

$$R_{\Gamma \mathrm{e}} \approx 9\frac{(dt/db)^2}{\pi\rho\omega_\Gamma\hbar^4 v^4}\int_{\hbar\omega_\Gamma}^{\infty} dE\, E(E-\hbar\omega_\Gamma)\times\{f_\mathrm{c}(E)[1-f_\mathrm{c}(E-\hbar\omega_\Gamma)](1+n_\Gamma)-f_\mathrm{c}(E-\hbar\omega_\Gamma)[1-f_\mathrm{c}(E)]n_\Gamma\}. \qquad \text{Eq 3.1}$$

Where , $\rho \sim 7.6\times10^{-7}\ \mathrm{kg/m^2}$ is the density of graphene ω_Γ and n_Γ are the frequency and occupation number of the Γ point phonons, dt/db ~ 45eV/nm, [106] υ is the Fermi velocity and $f_\mathrm{c}(E)$ is the Fermi Dirac distribution for electrons. The carrier temperature and the optical phonon occupation numbers can be described as a coupled rate equation system:

$$\frac{dT_\mathrm{c}}{dt} = -\frac{(R_{\Gamma\mathrm{e}}+R_{\Gamma\mathrm{h}})\hbar\omega_\Gamma+(R_\mathrm{Ke}+R_\mathrm{Kh})\hbar\omega_\mathrm{K}}{C_\mathrm{e}+C_\mathrm{h}},$$

$$\frac{dn_\Gamma}{dt} = \frac{R_{\Gamma\mathrm{e}}+R_{\Gamma\mathrm{h}}}{M_\Gamma}-\frac{n_\Gamma-n_\Gamma^o}{\tau_\mathrm{ph}},$$

Eq 3.2

$$\frac{dn_{\mathrm{K}}}{dt} = \frac{R_{\mathrm{Ke}} + R_{\mathrm{Kh}}}{M_{\mathrm{K}}} - \frac{n_{\mathrm{K}} - n_{\mathrm{K}}^{o}}{\tau_{\mathrm{ph}}}.$$

Where C_e and C_h are heat capacities of electrons and holes, τ_{ph} is the average lifetime of the optical phonons, n_{K}^{o} and n_{Γ}^{o} are phonon occupation numbers in equilibrium and M_K and M_Γ are the number of phonon modes per unit area that are involved in carrier-phonon scattering that can be estimated by methods presented in [102][107].

Knowing the carrier distribution and the temperature as a function of time, one can find the transient transmission response of graphene using the expression derived in [101]. Fitting the data to the described quantitative model, with two fitting parameters , τ_{ph} and n_0 , Wang et al. [102] find a fluence and substrate *independent* optical phonon life time $\sim 2.5\ ps$. This substrate and growth independence is contrary to our observation which we will present shortly. This was also contrary to the authors' expectations where they expected that the surface optical phonons of quartz and SiC would affect the optical phonon lifetimes and carrier relaxation times of graphene. They conjecture that this independence might be due to the fact that the samples used in this study were not single layer graphene. Furthermore, we believe that the lack of attention to the *surface roughness* as a critical and non-negligible parameter in the any pump probe experiment, can have a substantial impact on one's ability to resolve substrate coupled energy relaxation pathways.

Until 2011, most pump probe studies of graphene reported a bleaching of interband transitions presented as a uniform positive DTT or a uniform negative DTT (mostly seen in Terahertz studies).[102], [108]–[110] In a study by Malard et al., [111] it was shown that at relatively lower fluences, both a negative and a positive peak can appear. This fluence dependent study highlights the fact that the dynamics of graphene can only be described accurately with consideration of both inter and intraband contributions.

The optical response of graphene is known to originate from two distinct processes: inter band transitions and intra band transitions. [27][31][95] The previously discussed bleaching of interband transitions due to the band filling dynamics or Pauli blocking, results in an increase in transmission at very high electronic temperatures where a substantial filling of states can be induced. The intraband contribution induces a decrease in transmission through free carrier absorption and can be more dominant at lower carrier temperatures. The optical response of graphene arises from both inter and intraband contributions to the optical conductivity:

$$\Delta\sigma_{\,total} = \Delta\sigma_{\,intra} + \Delta\sigma_{\,inter} \qquad \text{Eq 3.3}$$

Where,[112]

$$\mathrm{Re}(\sigma_{intra}(\omega)) = \frac{4k_B T\sigma_0}{\pi\hbar}\left[\ln\left(1 + e^{E_F^h/k_BT}\right) + \ln\left(1 + e^{E_F^e/k_BT}\right)\right]\frac{\Gamma}{\omega^2 + \Gamma^2}$$

$$\mathrm{Re}\left(\sigma_{inter}(\omega)\right) = \frac{\sigma_0}{2}\left[\tanh\left(\frac{\hbar\omega-2E_F^h}{4k_BT}\right) + \tanh\left(\frac{\hbar\omega-2E_F^e}{4k_BT}\right)\right] \qquad \text{Eq 3.4}$$

With the universal conductivity $\sigma_0 = e^2/(4\hbar)$ and Γ being the Drude scattering rate and E_F the Fermi energy. The separation of chemical potentials for electrons and holes is considered to be insignificant due to the very fast Auger processes that connect the conduction and valance bands on a very short time scale.[96][100]

The photo induced change in σ_{intra} is expected to be positive and scale linearly with T, this is attributable to the free carrier absorption due to the presence of additional carriers excited to the conduction band of graphene by the pump beam. Whereas, the change in σ_{inter} will be negative due to Pauli blocking and the induced band filling dynamics. As seen in Figure 3.2 below, at lower fluences (carrier temperatures), the optical response of graphene, reflects the changes in the intraband dynamics and is positive in sign, whereas at higher fluences, it is overwhelmed by the interband contribution and has a negative sign. In the next section, we will present the fluence and excitation energy dependent dynamics of graphene transferred on quartz and discuss the inter vs intraband contribution strength.

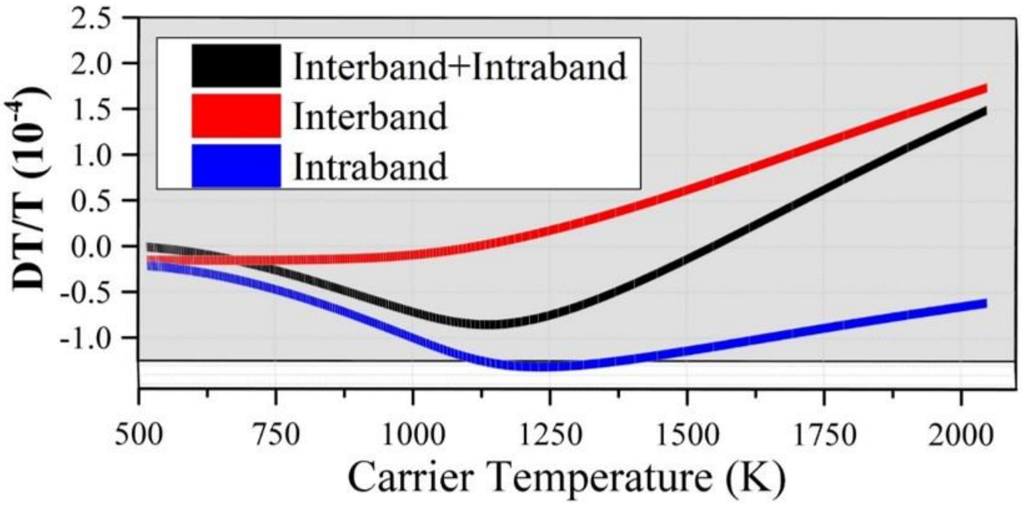

Figure 3.2. Simulated change in the transient transmission of graphene as a function of electronic temperature for a pumping energy of 1.6 eV and an intrinsic carrier density of 1x10^{12} /cm^2. The blue and red curves show the expected contributions from intraband and interband respectively and the black curve shows the total interband+intraband response.

3.3. Ultrafast transient transmission response of graphene on quartz

The opportunity to non-invasively study the relaxation dynamics of carriers and phonons and their consequent interactions in different material systems, is quite unique and advantageous.[113] UPPS can detect the time dependent changes in the complex index of refraction of graphene with fs time resolution. In the following sections, we will show that the evolution of the optical conductivity, carrier temperature and the relaxation times in graphene, depend on the energy and density of the photoexcited carriers and the number of the energy relaxation pathways available to them.

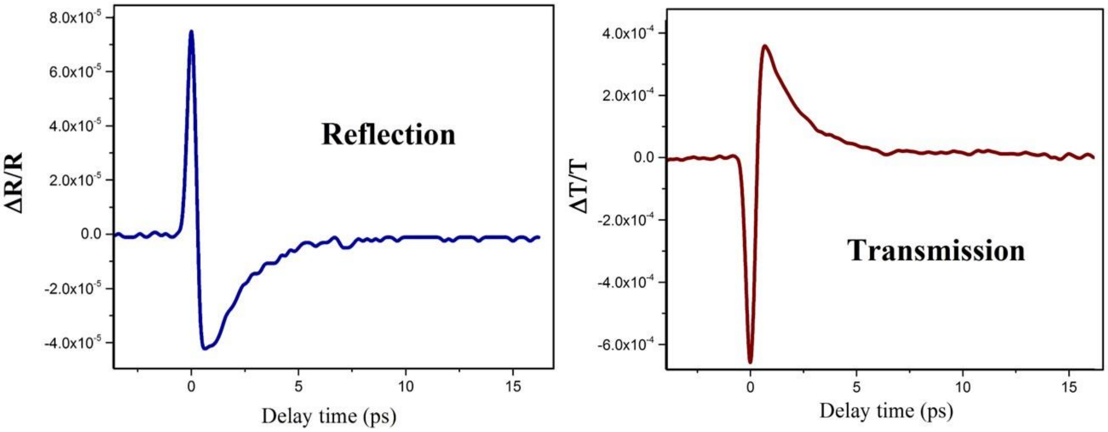

Figure 3.3. Transient reflection and transmission spectra for graphene on quartz, excited at 1.55 eV and measured simultaneously.

3.3.1. Experimental details

In a degenerate (single color) pump probe scheme, the output of a pulsed laser is divided into a stronger (pump) and a weaker (probe) beam, where both beams have the same energy but different powers and are both spatially and temporally overlapped. In our experimental setup, the pump pulse excites electrons to the conduction band of graphene and this change in the density of carriers is reflected in the measured optical conductivity (i.e. time dependent transmission, reflection or absorption) of graphene. Figure 3.3 shows the transient transmission and transient reflection results for graphene on quartz acquired simultaneously with two detectors. The results display that, although the amplitude of the signal is different in the two cases, the relaxation times and the ratio of the two peaks which is indicative of the inter vs intraband interplay, are the same for both transmission and reflection measurements. This means that either spectra could be used for our experiments. The measurements presented in this chapter are done in the transmission scheme due to the stronger signal it provides for our transparent samples.

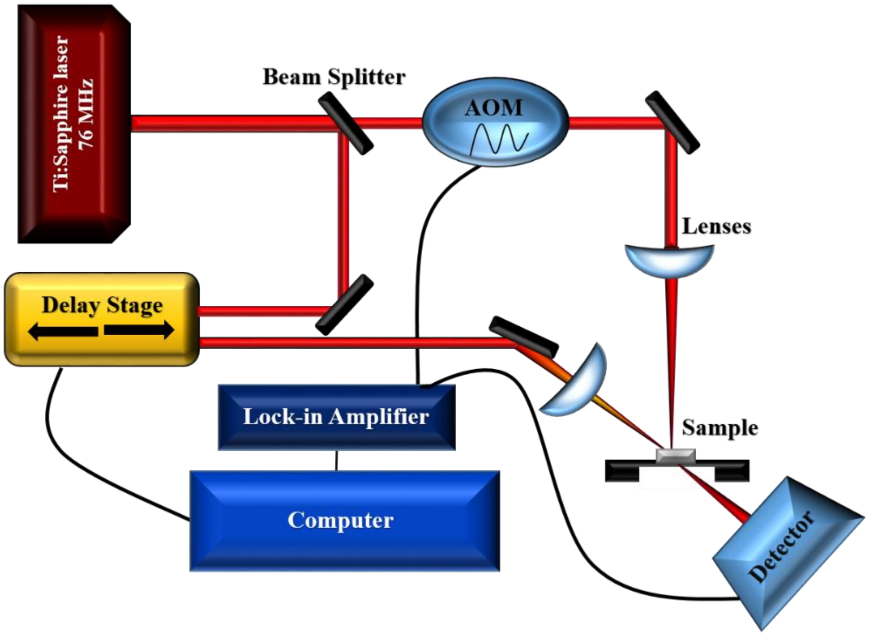

Figure 3.4. Experimental setup for the pump probe measurements presented in this thesis.

In this method, we measure the time dependent change in transmission as a function of the time delay between the pump and the probe pulse. Using a computer controlled delay stage we can change the optical path between these two beams and monitor the relaxation of the carriers as the system relaxes back to equilibrium and the pump induced changes in the optical conductivity of graphene approach zero.

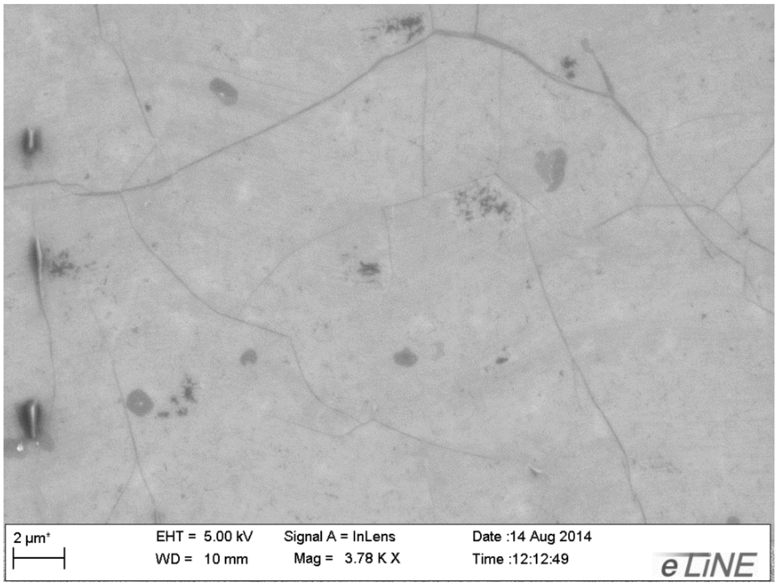

Figure 3.5. SEM image of graphene transferred on super polished quartz, the darker spots on the left of the image show a few rips in the graphene membrane where the insulating nature of quartz creates charging effects.

In the scope of this thesis, we use a Ti-sapphire laser (Coherent Mira 900) at $76\,MHz$ repetition rate and $100\,fs$ pulses. Figure 3.4 shows the schematics of the setup used. All measurements were taken at room temperature and a beam splitter was used to divide the tunable energy laser beam ($750\,nm\ - 850\,nm$) into two beam outputs. The spot size of the focused pump and probe beams are estimated to be $100\,\mu m$ and $50\,\mu m$ in diameter respectively. The average fluence range in our fluence dependent studies is between $(1 - 20)\ \mu J/cm^2$. Varying the pump and probe fluences are done using a continuous neutral density filter to minimize any changes to the alignment. The probe power is consistently kept at 15 x smaller than the pump power and the location of the beam on the sample and the environmental factors are not changed during experiments. We use an acousto-optical modulator (AOM) to modulate the pump frequency at 50 KHz and reduce the interference of the optical signal.

Using a phase sensitive lock-in amplifier with a sensitivity of ~10^{-6} we can measure the pump induced changes in the transmission (ΔT) of the sample. This change is proportional to the change in the voltage that is recorded by the lock-in amplifier.

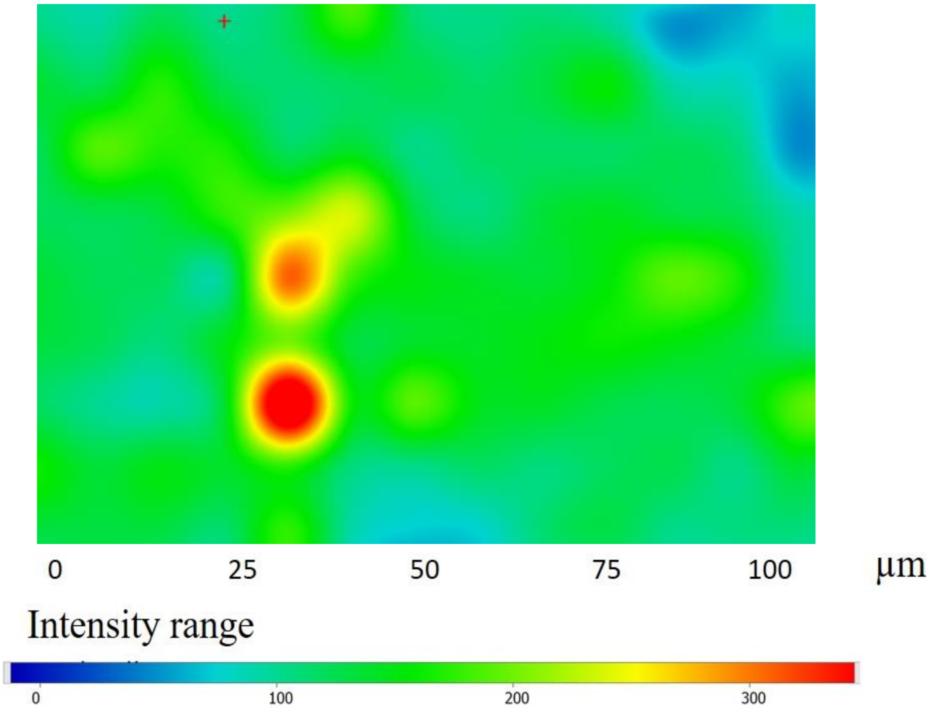

Figure 3.6. Mapping of the Raman 2D peak of graphene transferred on quartz. The mapping shows a uniform coverage of single layer graphene in the probed area.

We use a Labview-based software to record the lock-in amplifier data and control and record the position of the delay stage. To process the data, we subtract the voltage offset originating from the scattered pump beam. To obtain the differential transient transmission ($\Delta T/T_0$) we need to measure the steady state transmission T_0 in the absence of the pump. To acquire this information, we use a mechanical chopper and record the steady state read of the voltage while blocking the pump beam. To reduce the signal-to-noise ratio originating from the entrance of the scattered pump beam into the detector, we change the polarization of the pump beam 90° with respect to the probe.

Figure 3.5 shows the SEM image of CVD graphene transferred on a target quartz substrate (previously polished to sub 2 nm roughness). The details of the transfer process are explained in chapter 2. Mapping of the 2D Raman peak of graphene is shown in Figure 3.6. where point Raman mapping was used to ensure that the graphene coverage over the probed area is uniform. In addition, the shift in the Raman G peak was used to estimate the doping density of the graphene sample. (Details described in chapter 2)

3.3.2. Fluence dependent dynamics of graphene on quartz

To understand the effect of photoexcited carrier density on the optical conductivity of graphene, we performed transient transmission spectroscopy on graphene on quartz with an excitation wavelength of $790\,nm$ where we varied the pump fluence between 2-13 $\mu J/cm^2$. Figure 3.7. (a) shows the differential transmission response in the first 10 ps after photoexcitation for the highest and lowest pump fluences. For a better visualization of the trend, the inset shows the normalized transmission response ΔT at 10 inceremntal fluences where all spectra are shifted on both axes for clarity. As the fluence is increased, one can clearly see a crossover from decreased transmission (negative dip in ΔT) to an enhanced transmission (positive peak in ΔT). This observed crossover can be explained based on the opposing signs of the interband and intraband contributions to the optical conductivity of graphene and their dependence on the electronic temperature.

Figure 3.7. (b) shows the simulation results for the differential transient transmission of graphene, arising from interband and intraband contributions as well as the total interband+intraband transitions, as a function of carrier temperature. These simulations were based on the model described in references [102], [111] which will be discussed in more details in the next section. One can see that at higher (lower) electronic temperatures, the total differential transmission response of graphene is mostly dominated by the interband (intraband) transitions. At higher fluences and subsequently higher carrier temperatures, the induced bleaching arising from the Pauli blocking (PB) of the interband transitions are more dominant. Due to these band filling effects, the probe beam cannot get absorbed which results in an increase in transmission seen in the high fluence spectra in Figure 3.7 (a). For the same excitation energy, at lower fluences, there will be less carriers excited to the conduction band of graphene and the band filling dynamics will no longer be overpowering. Consequently, the total optical response of graphene is more dominated by the induced free carrier absorption from the intraband transitions which results in a decrease in ΔT seen in the lower fluence spectra in Figure 3.7. (a).

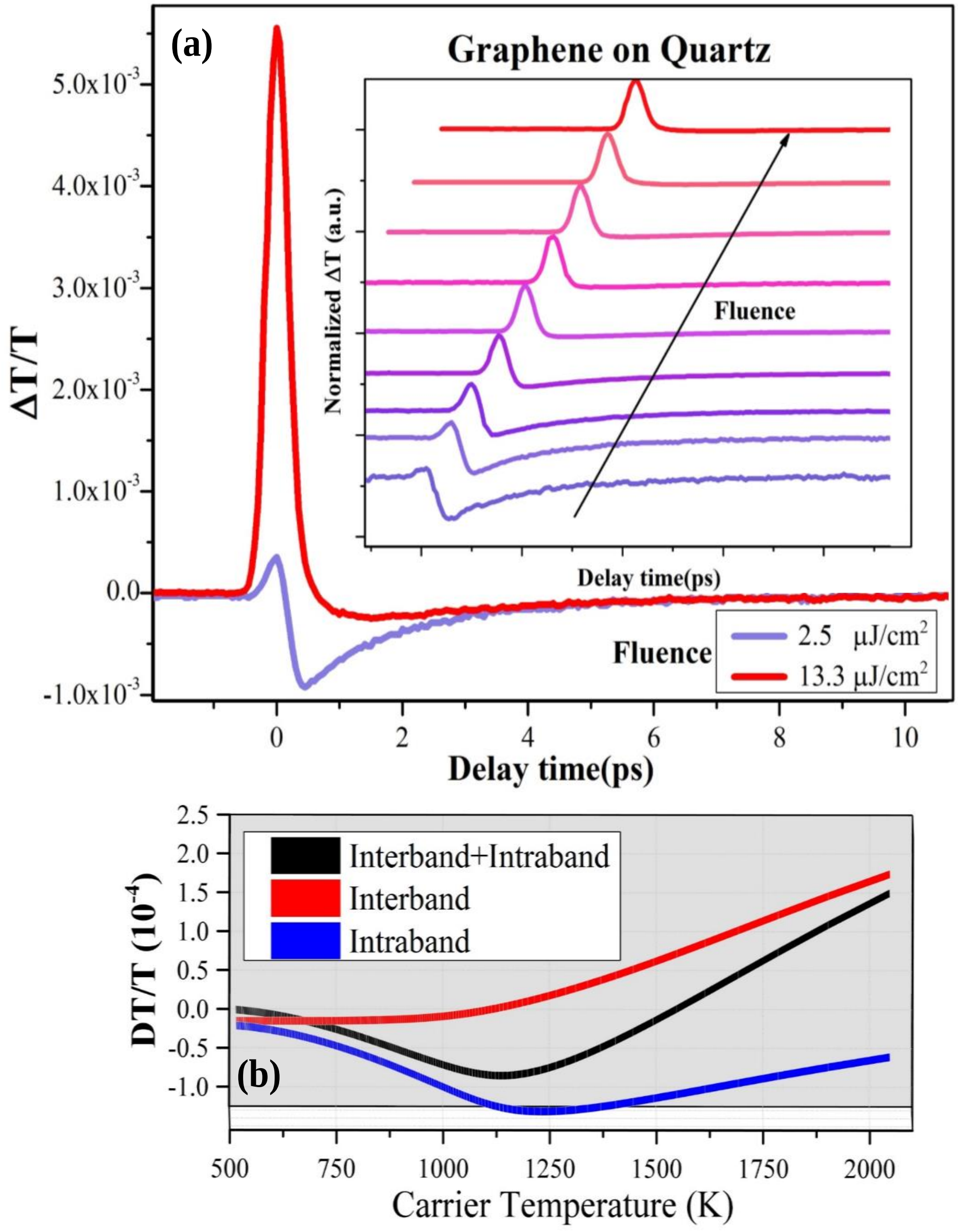

Figure 3.7. (a) Transient transmission response of graphene on quartz excited at 1.55 eV. The inset shows the normalized transmission for 10 incremental fluences. (All curves are shifted on both axes for clarity) **(b)** Simulated change in the transient transmission of graphene as a function of electronic temperature. The results are for a pumping energy of 1.6 eV and an intrinsic carrier density of 1x10^{12} /cm^2. The blue and red curves show the expected contributions from intraband and inter band respectively and the black curve shows the total interband+intraband response.

3.3.3. Excitation energy dependent dynamics of graphene on quartz

The linear band structure of graphene leads to exciting optical and electronic properties. In the results presented in Figure 3.7, we varied the number of the photoexcited carriers but kept the energy of these excited carrier the same. To understand the energy dependent ultrafast dynamics of carriers in graphene, we performed a set of pump probe measurements at different pumping and probing energies where the photoexcietd carrier density remained the same for all measurements. Figure.3.8 shows the transient transmission response of graphene on quartz, as a function of excitation energy. The energy range is between $1.46 - 1.6\ eV$, at a fluence of 5.1 μJ/cm^2. Although the energy range is quite small, one can see the extent of the diversity in the ultrafast dynamics. We define parameter γ as a measure of inter vs intraband interplay where:

$$\gamma \ = \frac{|\ positive\ peak\ in\ \Delta T| - |negative\ peak\ in\ \Delta T|}{|positive\ peak\ in\ \Delta T|}\ .$$

With $\gamma_{1.6\ eV} = 0.42$ and $\gamma_{1.46\ eV} = 1$, it is apparent that γ increases when excitation energy is decreased. At lower energies, we see a uniformly positive peak which implies that the interband contribution is more dominant. As the energy is increased, one can see that the positive peak becomes smaller and a negative dip appears. This decrease is attributed to the enhancement of carrier absorption through intraband transitions.

Due to the linear band structure of graphene close to the Dirac cone, DOS increases linearly with energy. [114] Consequently, given a similar photoexcited carrier density, the band filling dynamics will be more dominant for excitations to lower energy states with smaller DOS. This will result in the more dominant positive peak in transmission seen in the lower energy measurements of Figure 3.8. In contrast, excitations to higher energy states with larger DOS, lead to less overwhelming band filling effects and more pronounced intraband absorption which result in the observed decrease in ΔT in higher energy excitations of Figure 3.8.

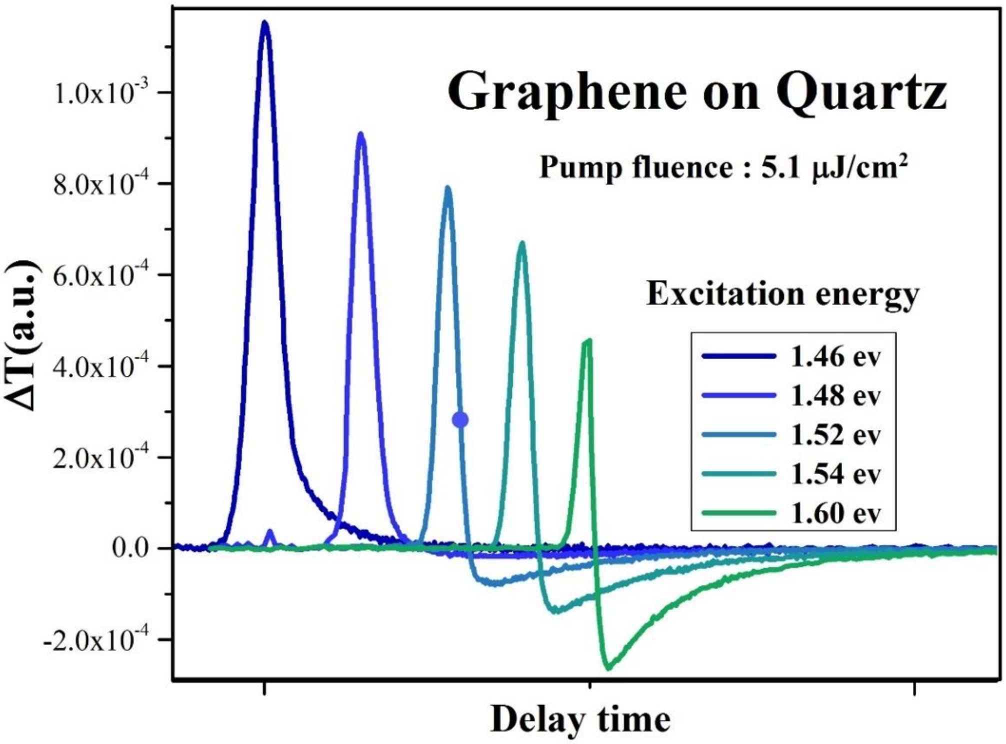

Figure 3.8. Ultrafast transmission response of graphene on quartz as a function of excitation energy and at a pumping fluence of 5.1μJ/cm^2. (All curves have been shifted on x axis for clarity)

As discussed in the beginning of this chapter, the ultrafast dynamics of graphene reported in the literature, have been quite diverse. They range from fully positive transmission (equivalent to fully negative reflection) [101][102][103] to fully negative transmission (positive reflection) [108][115][116] and a positive transmission followed by a negative transmission.[111][110][112] Based on the fluence and energy dependent results presented in Figure 3.7. and 3.8, we can conjecture that the diverse range of trends observed in the literature, could in part be due to the different fluence and pumping/probing energy regimes used in these studies. Later on in this chapter, we will demonstrate that furthermore, the underlying substrate can result in a modification of the ultrafast optical response which could also be a factor in the diverse range of reported dynamics.

In the next section, we will further expand on the quantitative model used in the theoretical calculations of Figure 3.7. (b) and discuss how this model is not sufficient to reproduce our substrate dependent results without the inclusion of substrate coupled extrinsic energy relaxation pathways.

3.4. Simulation and fitting parameters

As discussed, we can simulate the femtosecond transient transmission response of graphene, based on the model described in reference [102]**.** In this model, the energetic carriers decay through optical phonons of graphene and the decay of these optical phonons to the lower energy acoustic phonons, present a bottle neck for the energy relaxation. It is important to note that intrinsic optical phonons are the only decay channel considered in this model and no energy relaxation pathways coupled to the substrate are directly taken into account.

By fitting the experimental pump probe data to this model, one can infer the intrinsic optical phonon lifetime τ and momentum scattering rate Γ. The optical phonon lifetimes reported in the literature, using various direct and indirect measurements, are quite diverse for both graphene and graphite and range from 1.2 ps to ~7 ps. [117][118][119][102][120] By fitting the described model to their experimental data, Wang et al.[102] derived an optical phonon lifetime of $\sim 2.5\ ps$, *independent of the substrate and fluence.* In a study done by Maralard et al., a fluence independent time constant $\tau_{\mathrm{ph}} \sim 1.4\ ps$ was derived. [111] However, the decay time obtained by fitting the experimental data to a mono-exponential decay, produced a relaxation time $\tau_{\mathrm{exp}} \sim 3.1\ ps$. Malard et al. claim that this difference is due to the significant temperature dependence of the phonons heat capacity. The carrier temperature, which tracks the optical phonon temperature, is described by τ_{exp} and falls slower than the energy content of the optical phonons, characterized by τ_{ph}.

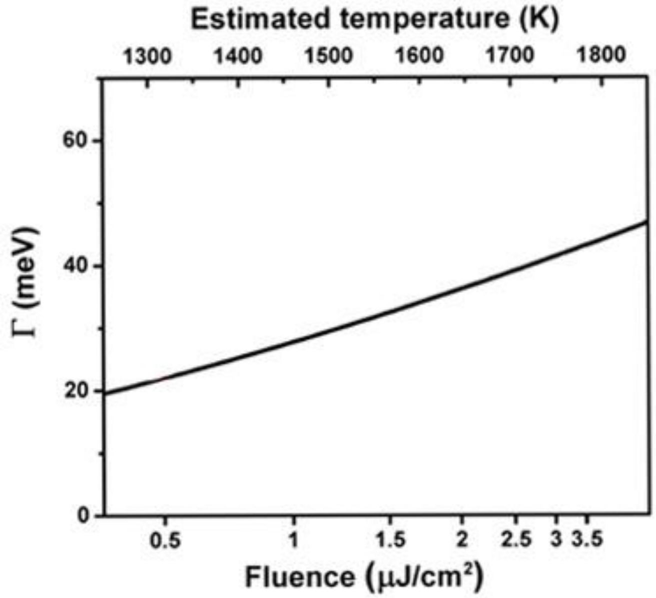

Figure 3.9. Calculated temperature dependence of the Drude scattering rate due to the electron-optical phonon interactions. The top scale shows the inferred peak temperature of electrons. Reference[111]

The range of reported values for the other fitting parameter, momentum scattering rate Γ, has been quite diverse as well. Using a variation of the described model, Chen et al.[112] found a sub femtosecond momentum scattering time which differs greatly from the $10-100\ fs$ accepted otherwise in the literature. The contribution to the carrier scattering rate can arise from a few different mechanisms, [121] namely: elastic scattering with intrinsic acoustic phonons, [122][123] inelastic scattering with intrinsic optical phonons at higher temperatures, [111][124] [125] impurity scattering [126][127] and scattering with phonons of the substrate. [128][129][130][131] [132]

In most studies, one or two of these scattering mechanisms, mainly impurity scattering and sometimes intrinsic optical phonon scattering are considered to have a direct impact on Γ. In the context of pump probe experiments, scattering with optical phonons of the *substrate* is rarely considered. Malard et al. noted that their treatment of only considering optical phonon contribution to the Drude scattering rate is not complete, adding that contributions from e-e scattering and carrier-surface phonon scattering need be taken into account for a more accurate and detailed description.

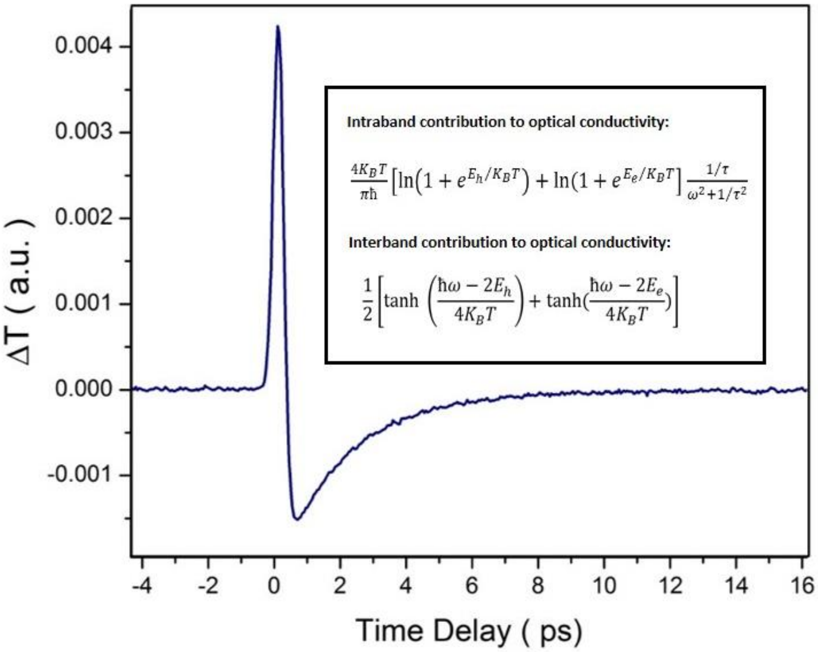

Figure 3.10. Simulated transient transmission of graphene on quartz, with inclusion of both interband and intraband contributions to the optical sheet conductivity.

In addition, in the model described above, Γ is taken to be independent of carrier density and carrier temperature and not affected by phonon scattering channels coupled to the substrate. Figure 3.9 shows the calculated Drude scattering rate as a function of carrier temperature derived by reference [111]. In a pump probe experiment, carrier temperatures and densities, change as a function of time. Subsequently, Γ will not only be fluence dependent, but also time dependent. For simplification, in almost all multiple temperature models of graphene dynamics, Γ is taken to be independent of fluence and time. However, a more comprehensive analysis would need to take these factors into account. In addition, the role of the substrate which can alter carrier temperature and ultimately impact the time dependent Γ, needs to be considered.

Figure 3.10 shows our simulations results based on the described model where both positive and negative peaks observed in our transmission spectra can be qualitatively reproduced. Fitting the simulation results to our experimental data, the model can fairly replicate the experimental results at *higher fluences* for *quartz*, however, it fails to reproduce the right peak ratios and carrier relaxation times for the the lower fluence regimes. More importantly, it fails to reproduce the substrate dependent data presented in the following section.

In addition, the inferred optical phonon lifetimes obtained from fitting the data to the model are unphysically small ($\sim 100\ fs$). The inability to reproduce lower fluence data, as well as the unrealistically short inferred optical phonon lifetimes, point to the fact that the single channel relaxation picture with graphene's optical phonons as the only relaxation mechanism, is not complete and an additional relaxation pathway most possibly through the substrate needs to be taken into account. In the following sections, we will study the effect of substrate on the relaxation dynamics of graphene and discuss the surface optical phonon decay channel and its impact on the carrier temperature and intrinsic optical phonon life times of graphene.

3.5. Effect of substrate on the ultrafast dynamics of graphene

To understand the ultrafast optical conductivity of graphene, one of the main questions that needs to be answered is: “How does the introduction of a substrate affect the ultrafast carrier and phonon energy relaxation channels in graphene?”

Due to the varying extent and the contradictory nature of the reported results, this question still remains unresolved. In 2011, Hale et al.[133] compared the relaxation dynamics of suspended and supported graphene and reported faster relaxation for suspended graphene. In the same year, Gao et al.[118] reported faster relaxation for graphene supported on a substrate. Wang et al.[102] compared the relaxation of CVD graphene on quartz and epitaxial graphene on both Si and C face of SiC and reported that these dynamics do not depend on the substrate or the growth method.

As we discussed in chapter 2, the energy relaxation pathways coupled to the substrate are highly sensitive to the roughness of the surface and the strength of this coupling greatly decreases as the distance between graphene and the substrate is increased. If the conformity of graphene and substrate is not optimal, the relaxation dynamics would be dominated by graphene’s intrinsic relaxation pathways and could potentially be modeled solely through scattering with intrinsic optical phonons. Thus, to resolve any ultrafast energy loss mechanisms attributed to the substrate, it is of utmost importance that the studied substrates are “smooth” and have a uniform ultra-fine sub nm polish in the studied areas. Furthermore, an accurate comparison of graphene’s ultrafast carrier dynamics on different substrates, is only possible if all studied substrates possess a *comparable* surface roughness.

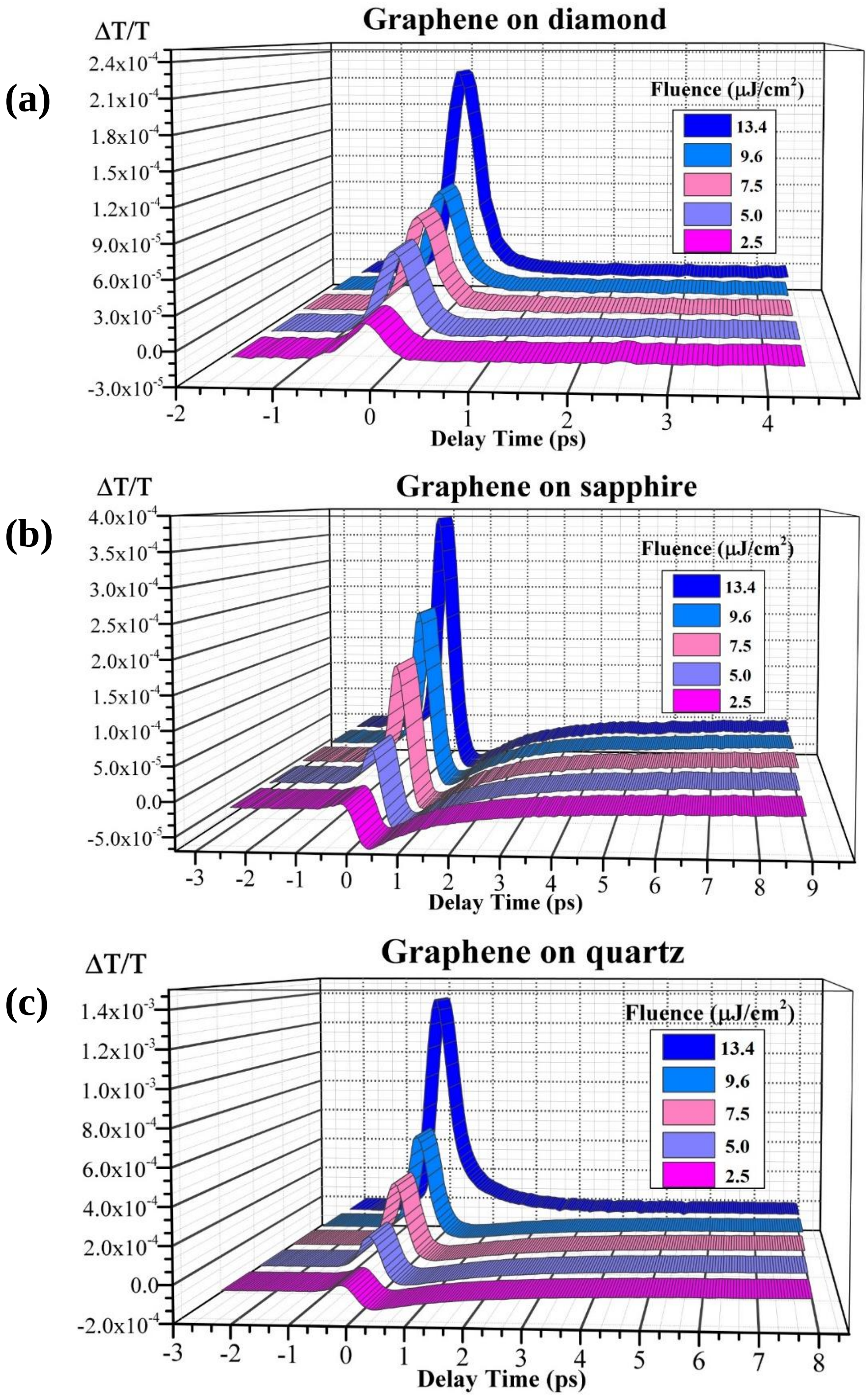

Figure 3.11. Fluence dependent ultrafast transmission response of graphene on: **(a)** diamond, **(b)** sapphire and **(c)** quartz, excited at 1.6 eV.

To isolate the influence of the substrate on the femtosecond dynamics of graphene, we carried out a comprehensive set of excitation energy, fluence and substrate dependent experiments where extra measures were taken to prepare and ensure a sub nm roughness for all substrates. We believe that due to the ultra-fine polish of our samples, the graphene-substrate coupling is less obstructed. In addition, in comparison to other reported studies, these interactions are more highlighted due to the lower fluence regimes applied in our experiments.

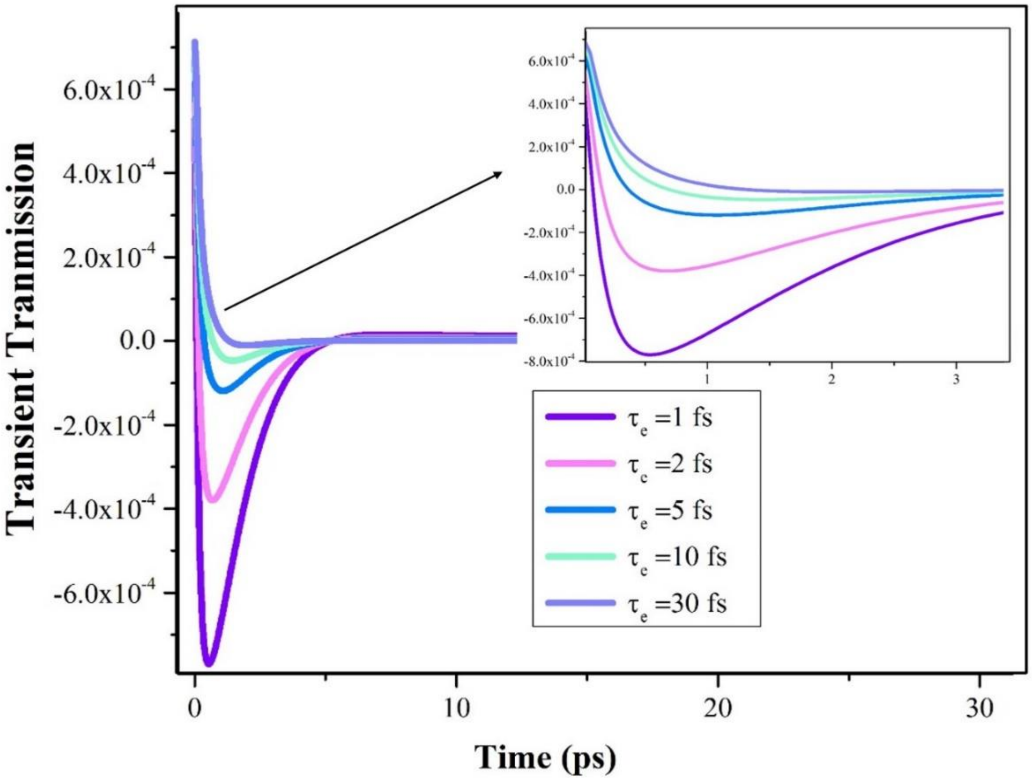

Figure 3.12. Simulation results of the momentum scattering-time dependence of the transmission response of graphene on quartz. Pumping and probing energies are set at 1.6 eV. (For better visualization, the inset shows the response for the first 3 ps)

We used CVD graphene transferred onto three different substrates namely: quartz, sapphire and (100) face of single crystalline diamond. To guaranty that the observed differences in the dynamics, arise only due to the differences in the underlying substrate and not due to the growth or fabrication variations, the CVD graphene transferred on all samples, was grown in a single growth batch and the transfer process on the multiple substrates, was conducted in parallel and at the same time. (Details described in chapter 2) Throughout the pump probe measurements, all experimental conditions were kept as identical as possible.

Figure 3.11 shows the fluence dependent transient transmission response of graphene for all three samples for an excitation and probing energy of 1.6 eV. Looking at the results from Figure 3.11 (a-c), it is clear that the substrate has a substantial impact on the femtosecond non-equilibrium carrier dynamics of graphene and can result in an enhancement or decrease in graphene's absorption as well as modification of carrier relaxation times. Looking at Equation 3.4, one can see that the choice of substrate could influence the optical sheet conductivity of graphene in two distinct ways:

- Induce changes in the intrinsic doping density or the static Fermi level (E_F) of graphene.
- Provide an additional scattering mechanism through phonons of the substrate which can modify the momentum scattering rate and more importantly assist in the dissipation of the electronic energy and reduction of the carrier temperature.

Based on the model described in the previous section, Figure 3.12 shows the dependence of the transient transmission dynamics of graphene on the momentum scattering time τ_e. One can see that decreasing the momentum scattering time results in a more pronounced negative dip in transmission, which implies more scattering events and an increase in the free carrier absorption. The dependence of the dynamics on the static Fermi level of graphene is shown in Figure 3.13. Our simulations show that increasing E_F, leads to an increase in the interband transitions and hence a less negative ΔT response.

By defining a time dependent Fermi level and carrier temperature, similar results were obtained by Chen et al.[112] where the effect of τ_e and Fermi level E_F on the optical conductivity of graphene were studied. Although this study did not directly take into account the effect of substrate, the presence of the substrate can induce changes in both of these parameters.

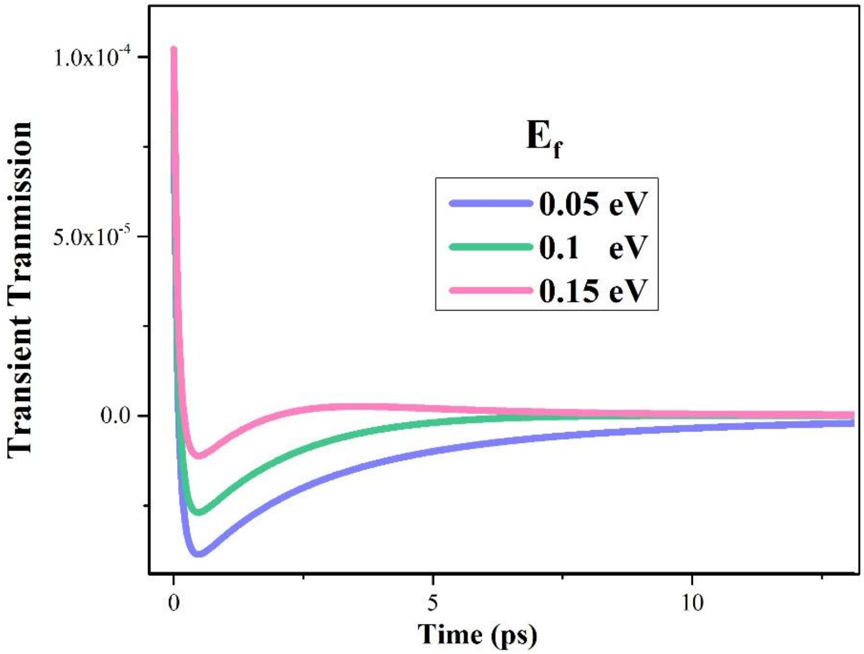

Figure 3.13. Simulation results showing the dependence of the transient transmission of graphene (transferred on a quartz substrate), on the static Fermi level. Pumping and probing energies are at set at 1.6 eV.

To ensure that the differences observed in our dynamics are not solely due to the different doping levels of the graphene samples, we performed Raman point mapping on the probed areas of all 3 samples. Figure 3.14 shows the Raman mapping of the relative shift in the G peak position of graphene transferred on quartz. This mapping is used to estimate the average doping and static Fermi level of graphene in the areas probed in the pump probe experiments. (details discussed in Chapter 2) The estimated shift in the Fermi level for the three studied substrates are displayed in Table 3.1.

Table 3.1. The estimated shift in the Fermi level of graphene for the three studied substrates, obtained by Raman mapping.

Substrate	**Diamond**	**Sapphire**	**Quartz**
E_F (eV)	0.21 ± 0.01	0.27 ± 0.01	0.35 ± 0.01

Based on the simulation results of Figure 3.13, the lower the Fermi level, the more negative the differential transmission response ΔT, will be. Looking at the estimated Fermi levels of the three samples in Table 3.1, if the differences in the static Fermi level of each substrate were the underlying reason behind the diversities observed in our experiments, therefore, one would expect graphene on diamond with the smallest shift in Fermi level to have the most negative transmission response. However, Figure 3.11 reveals the opposite outcome, with graphene on diamond having a uniformly positive transmission.

The more positive transient transmission response of graphene on diamond compared to other substrates was also confirmed at different excitation energies and reveals that the difference in the doping of the studied samples cannot account for our experimental results. Therefore, there must a more dominating factor arising from the additional energy relaxation channel through the surface phonons of the substrate that can significantly modify the femtosecond optical conductivity of graphene on different substrates.

It is known that the surface optical phonon modes present in polar materials, can have electric fields extended over distances past the surface of the substrate and affect the carriers in graphene through long range Fröhlich interactions. [128][131][134] This remote carrier scattering mechanism through surface optical phonons (SP), has been known to not only limit the transport properties of graphene, [130] but also impact the ultrafast relaxation dynamics of carriers and phonons. [118][119]

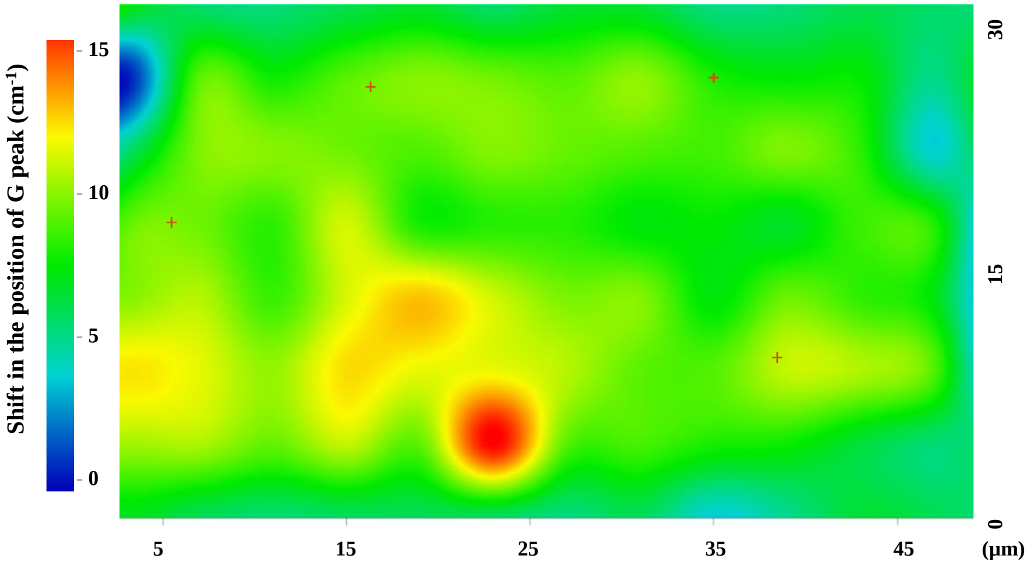

Figure 3.14. Raman mapping of the relative shift in the position of the G peak of graphene transferred on quartz.

We believe that on our smooth polar substrates, the charge carriers in graphene can readily couple to the electric field generated by the surface polar phonons of the underlying substrate. This coupling can significantly alter the transient electronic temperature T_{el} by providing an additional scattering channel and consequently modifying the ultrafast optical response of graphene. The efficiency of this cooling channel will depend on the separation distance between graphene and the polar substrate, the energy of the surface phonon modes

$\hbar\omega_{SOP}$, the Fröhlich coupling constant F_{SOP} and the intrinsic doping of graphene.[128][131][134] In the following sections, we will discuss the SP scattering mechanisms and the impact on the carrier dynamics and optical phonon lifetimes of graphene.

3.6. Surface optical phonon of polar materials

Remote phonon scattering through surface phonons of polar materials, is a known limiting factor in the electron mobility and transport properties of graphene. High k dielectric materials, relevant in graphene FET and device technology, allow for the carriers of graphene to electrostatically couple to the polarization field created at the interface of these polar materials through long range Fröhlich interactions. The interaction primarily occurs with high frequency optical phonon modes $(50\text{–}200 meV)$. [131] This surface polaronic effect is enhanced in single layer graphene, due to the poor screening properties of the quasiparticles near the Dirac point and can highly influence the hot electron/phonon dynamics and high temperature mobility of graphene.[135][136][130]

In 2008, in a four probe resistivity experiment, Chen et al.[130] studied the performance of graphene based devices on SiO_2 where the observed density and temperature dependent resistivity at room temperature was attributed to the scattering from surface optical phonons of SiO_2. Since the same results were observed for ultra-clean samples under vacuum and “dirtier” samples with more resist residue and adsorbed contaminant, it is concluded that *the observed resistivity is intrinsic to the graphene-SiO_2 interface and is not due to the impurity scattering.*

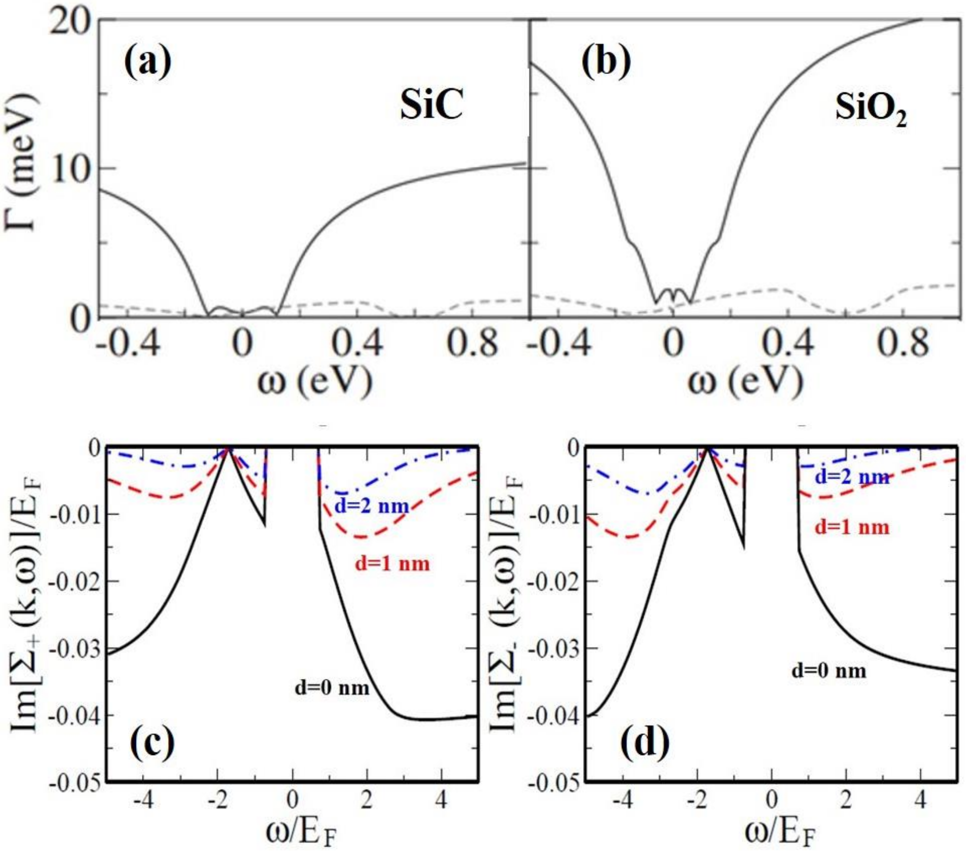

Figure 3.15 Surface optical phonon scattering rate as a function of energy for **(a)** SiC **(b)** SiO_2. The dashed lines correspond to E_F=0.6 eV and the full lines correspond to intrinsic undoped graphene.[134] Imaginary part of the self-energy Σ for **(c)** SP emission and **(d)** SP absorption as a function of energy for T=0 for different separation distances, 0,1 and 2 nm. Screening is taken into account for both cases. Adapted from reference [128]

In a theoretical study, Sabio et al. [137] compared the electrostatic interactions between graphene and SiO_2 and graphene and charge impurities and confirmed that the leading effects are due to the polar modes of the SiO_2substrate and not the impurities resulting from the graphene transfer process. It is deemed that at low temperatures, the mobility of graphene is limited by impurity scattering whereas at higher temperatures, SP scattering becomes more dominant over longitudinal acoustic phonon scattering. This increase in resistivity, due to the remote surface phonon scattering, poses a tradeoff for using higher dielectric substrates to reduce the effects of impurity scattering due to an increase in screening.

3.6.1. Fröhlich coupling and the role of the separation distance

In the presence of surface optical phonons, the electrons in graphene interact with other electrons not only through Coulomb interactions but also through remote virtual surface optical phonon scattering via Fröhlich coupling. The strength of this coupling M(q) can be expressed as:[128]

$$[M(q)]^2 = \frac{M_0^2}{q\varepsilon(q)} e^{-2qd} \qquad \text{Eq 3.6}$$

Where

$$M_0^2 = \pi e^2 \omega_{SO} \left[\frac{1}{\varepsilon_\infty + 1} - \frac{1}{\varepsilon_0 + 1} \right] \qquad \text{Eq 3.7}$$

Where d is the separation distance between graphene and the polar surface, ε_0, the static dielectric constant and ε_∞, the dielectric constant at high frequencies. The frequency of the SP mode ω_{SO} can be determined by the frequency of the transverse bulk phonon mode ω_{TO} through: [134]

Eq 3.8

$$\omega_{SO} = \omega_{TO}\sqrt{\left(\frac{1+\varepsilon_0}{1+\varepsilon_\infty}\right)}$$

As one can see from Eq 3.6, due to the long range nature of the surface phonon interactions, considerations of the separation distance between graphene and the substrate (d) as well as the screening effects are critical. Hwang and Sarma [128] calculated the self-energy (Σ) and scattering rate in the presence of SP mediated electron interactions as a function of carrier energy. The imaginary part of the electron self-energy $Im[\Sigma]$ can be used to extract the quasi-particle lifetimes and dissipation rates of excited carriers in graphene.

It is shown that screening can reduce the calculated SP scattering rate by a factor of 5 and the exponential dependence of the SP coupling strength on the separation distance, i.e., e^{-2d} , can result in a substantial decrease in the SP scattering rate as the distance between graphene and the substrate is increased. Figure 3.15 (c and d) show the Imaginary part of the self-energy corresponding to the emission (+) and absorption (-) of an SP for different separation distances. As one can see, at a separation distance of ~ $2nm$, $Im[\Sigma]$ drops by at least an order of magnitude. The dependence of the SP interactions on the separation distance (d), further highlights the importance of the sub nm surface roughness used in our experiments and sets our measurements apart from other studies.

3.6.2. Effect of doping and polarity of the substrate

In a theoretical study, Fratini et al.[134] found the origin of the density-dependent room temperature mobility in graphene to be due to the carrier interactions with the surface optical phonons of polar materials. This in turn puts a limit on the transport properties of single layer graphene. Table 3.2 shows the reported values of ε_0, $\varepsilon_\infty$and ε_i (static, intermediate and high frequency permittivities respectively) as well as the surface phonon frequencies and associate bare Fröhlich constants $\boldsymbol{F^2}_{\boldsymbol{SO}}$ defined through:

$$F_{SO1}^2(q) = \frac{\hbar\omega_{SO1}}{2\pi}\left[\frac{1}{\varepsilon_i + 1} - \frac{1}{\varepsilon_0 + 1}\right]$$

$$F_{SO2}^2(q) = \frac{\hbar\omega_{SO2}}{2\pi}\left[\frac{1}{\varepsilon_\infty + 1} - \frac{1}{\varepsilon_i + 1}\right]$$

Knowing these parameters, Fratini et al. calculated the scattering rate due to the surface optical phonons of SiC and SiO_2 for both doped and undoped graphene. It is evident that *intrinsic doping, reduces the SP coupling considerably* for graphene on both substrates. This effect is attributed to the poorer screening properties of Dirac electrons close to the Dirac point which results in a much higher scattering rate for undoped graphene. The sensitivity of the SP coupling to the intrinsic doping has been confirmed by a number of different studies.[128] [138][139]

Looking at Figure 3.15 (a and b), one can see that SP scattering rate is higher for graphene on SiO_2 compared to graphene on SiC. The low polarizability of SiC and higher surface phonon frequencies compared to sapphire or quartz, results in a less pronounced effect from the carrier-SP coupling in the transport and ultrafast pump probe measurements for epitaxial graphene. Scharf et al. [139] studied the effect of surface and intrinsic phonons of graphene on the steady state optical conductivity of doped graphene on various substrates.

Table 3.2. Static, intermediate and high frequency permittivities, surface phonon frequencies and bare Fröhlich coupling constants for different substrates. Adapted from reference [139]

	Al_2O_3	**SiO_2**	**HfO_2**	**SiC**	**h-BN**
ε_0	12.53	3.90	22.0	9.7	5.09
ε_i	7.27	3.36	6.58	—	4.57
ε_∞	3.20	2.40	5.03	6.5	4.1
$\hbar\omega_{SO1}$ (meV)	56.1	58.9	21.6	116.0	101.7
$\hbar\omega_{SO2}$(meV)	110.1	156.4	54.2	—	195.7
F^2_{SO1}(meV)	0.42	0.23	0.30	0.735	0.25
F^2_{SO2}(meV)	2.05	1.6	0.29	—	0.52

Theoretically, due to the Pauli blocking effect, for energies $0 < \hbar\omega < 2|E_F|$, the optical conductivity of graphene is expected to go to zero. However, as seen in Figure 3.16, one observes a finite midgap absorption which shows a strong substrate dependence. At room temperature, this phonon assisted absorption could be close to 20–25% for graphene on polar substrates as opposed to 5% for suspended graphene.

Although all polar substrates, affect the optical conductivity of graphene, sapphire has the most pronounced impact on the optical dynamics of single layer graphene. In a pump probe experiment, we measure the real part of the transient optical conductivity of graphene. Consequently, not considering the substrate coupled energy relaxation pathways, results in incomplete and sometimes contradictory results.

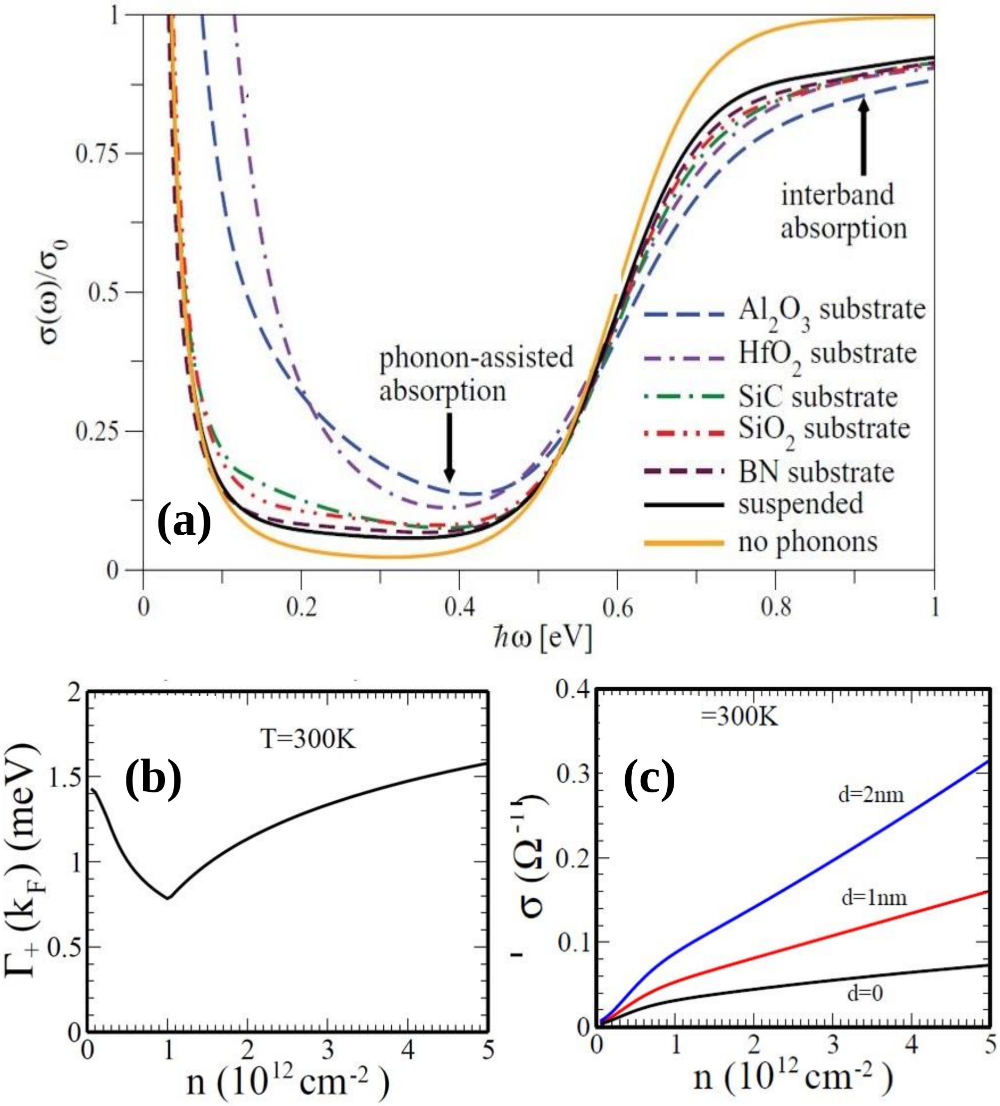

Figure 3.16. (a) Calculated energy dependence of the optical conductivity of graphene on different substrates. Adapted from [139] **(b)** SP scattering rate as a function of carrier density at T = 300K **(c)** calculated conductivity as a function of density for different separation distances at T= 300 K. [128]

Unlike most pump probe studies in IR and NIR spectral range where the primary relaxation channel considered is solely through the intrinsic optical phonons of graphene at Γ and K points, both intrinsic and extrinsic phonon channels need to be taken into account for a correct depiction of graphene's ultrafast carrier dynamics.

3.6.3. Intrinsic optical phonon vs. surface optical phonon scattering rate

Knowing that the substrate can provide an additional cooling channel in the carrier relaxation process, the most relevant question evidently becomes: "What is the strength of this cooling mechanism compared to the intrinsic optical phonons of graphene?" In 2006, a study done by Petrov and Rotkin [140] showed that the *SP life times are close to 1.5 to 2 orders of magnitude shorter than the intrinsic optical phonon lifetimes of CNT*, making the emission of surface optical phonons into the substrate the main energy relaxation mechanism in CNTs. In this picture, hot carriers can transfer energy *directly* into the substrate without an intermediate stage in which the CNT optical phonons would have to be heated up. In this case, the carriers are in thermal equilibrium with the substrate bath whose heat capacity is limited. The SP relaxation time is inversely proportional to the surface optical phonon energy and the rate is proportional to the Fröhlich constant at that specific SP frequency.

Using the Fermi golden rule, Petrov et al. calculated the probability of electron scattering through surface phonons and found the SP emission to be the *main* relaxation mechanism. As seen in Table 3.3, quartz possess five SP modes, where the first and third are commonly neglected due to the very small optical activity, however, the $150\,meV$ and $63\,meV$

modes, have calculated lifetimes of $\sim 12\ fs$ and $45\ fs$ respectively, which is remarkably short compared to the intrinsic optical phonon life times of CNT. [141][142]

Table 3.3. Calculated relaxation times due to surface phonon modes of quartz. (Phonon mode 4 is doubly degenerate) Reference[140]

mode	$\hbar\omega_{SO}$	τ
1	50 meV	0.4 ps
2	63 meV	0.045 ps
3	100 meV	0.3 ps
4	153 meV	0.012 ps

Similar results were obtained for graphene by Low et al. [138], where the cooling power of different relaxation pathways through IP, SP and acoustic phonon scattering were compared. They find that in most conditions, the carrier dynamics of graphene are mostly dominated by remote phonon scattering through the SP channel.

Since the key to efficient photovoltaics is the conversion of photoexcited carrier energy into electric current (before it loses energy to the phonon bath), the coupling of carriers to the surface phonons of polar substrates, can considerably lower the overall strength of the photocurrent response in graphene by an order of magnitude. However, this mechanism could also provide opportunities in terms of energy dissipation for FET devices.

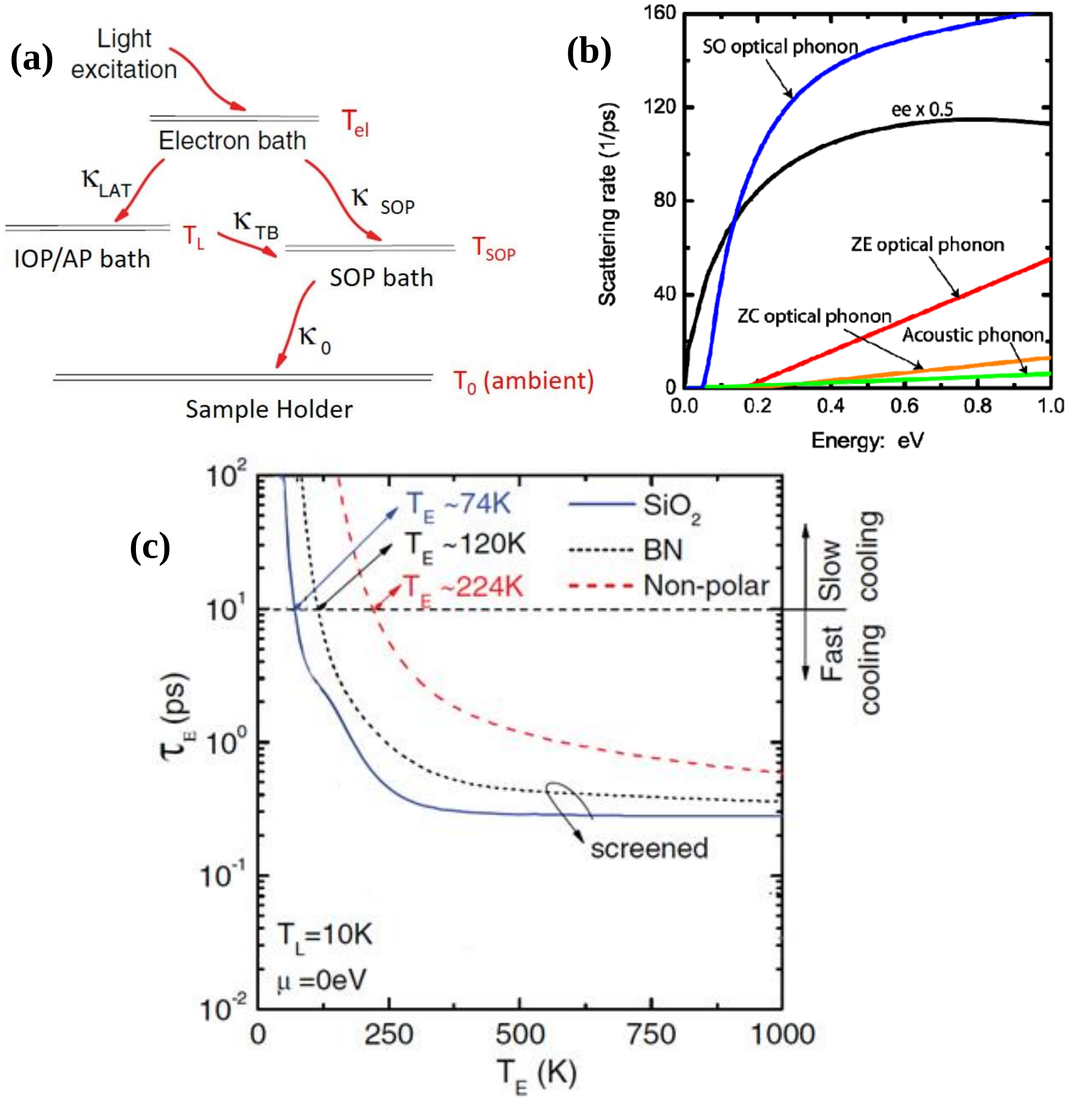

Figure 3.17. (a) Illustration of different energy relaxation pathways after photo excitation. [138] **(b)** Calculated scattering rates as a function of energy for different energy relaxation channels: Surface optical phonon scattering, electron-electron scattering, zone edge and zone center intrinsic optical phonon scattering and acoustic phonon scattering.[118]**(c)** Carrier cooling time τ_E as a function of carrier temperature for cold intrinsic graphene on different substrates. The SP interactions considered here are screened. Adapted from reference [138]

In chapter 4, we will discuss the remarkably high photocurrent response of freestanding curled graphene ribbons at zero source and drain bias. The observed high photocurrent could in part stem from the lack of substrate-coupled energy relaxation pathways, where the photoexcitation energy can stay in the electronic system long enough for the current to be collected and not be lost to the phonon bath of either graphene or the substrate.

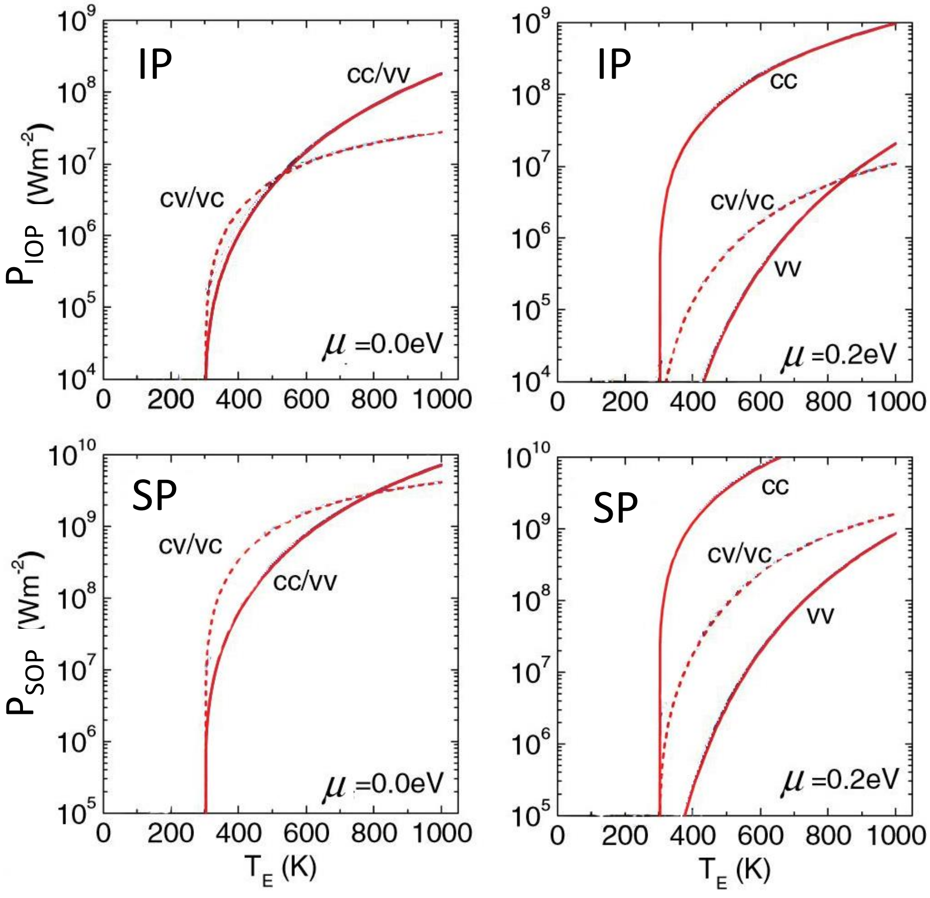

Figure 3.18. Electron cooling power due to intrinsic optical phonons of graphene (IP) and unscreened surface optical phonons of the substrate (SP) for doped and undoped graphene. CC and VV denote intraband and CV and VC denote interband transitions. Adapted from reference [138]

Figure 3.17. (a) illustrates the mechanisms of energy exchange between different thermal baths, where the heat exchange between these baths is described by the thermal conductivity κ. It is clear that, carriers can directly exchange energy with the substrate through substrate polar phonons, without necessarily having to first heat up the intrinsic phonon bath. Figure 3.17. (b), shows the theoretical calculations by Gao et al.[118] where the scattering rate due to the different energy relaxation mechanisms are compared. As one can see, the SP scattering rate is considerably higher than graphene's intrinsic optical phonon scattering rate in the relevant range of our experiments.

Figure 3.18 shows the calculated cooling power of the intrinsic optical phonons of graphene compared to the substrate surface phonon channel for both doped and undoped cases. One can see that the SP electron cooling power is consistently higher than the IP channel, making it the primary energy relaxation channel for both doped and undoped graphene. Furthermore, as discussed earlier, doping compromises the efficacy of the electron-SP interactions and reduces the cooling power of the surface phonon channel.

In an ultrafast pump probe experiment, the temporal evolution of the carrier temperature and the relaxation of the energetic carriers and their associated densities can be effectively monitored. Figure 3.17. (c) shows the cooling time τ_E as a function of the electronic temperature T_{el}, where, as the carriers cool down, the bottleneck represented by the cooling via acoustic phonons sets in and leads to longer decay times. The temperature at which this transition to the slower cooling regime happens, depends on the underlying substrate and is dictated by the lowest frequency SP mode. It is evident that at a given electronic temperature, the carrier cooling times are much faster for graphene on polar substrates.

As we saw earlier in Figure 3.15 (c-d), at higher energies, $Im[\Sigma]$ and consequently the quasi particle life time seems to reach a saturation value. A comparison of these results with the self-energy calculated for non-polar intrinsic LO optical phonon ($\omega_{LO} \sim 200\ meV$) shows that for large $|\omega|$, due to the linear increase in DOS, the imaginary part of Σ increases linearly for intrinsic optical phonons, whereas for long range surface optical phonons, the imaginary part of Σ reaches a saturation value. Hwang et al. [128]claim that at a finite distance d, the relaxation of electrons through SP, depends weakly on the electron energy. As a result, at higher energies, hot electrons decay more effectively through LO phonons rather than SP. Figure 3.16. (b) shows the SP scattering rate as a function of carrier density. With the scattering rate Γ known, one can calculate the conductivity (Figure 3.16. (c)) which shows a similar trend as the trend confirmed experimentally in reference[130]. Due to the long range nature of SP interactions, graphene conductivity limited by SP scattering, increases with density, whereas, conductivity limited by LO phonons shows a weak density dependence.[122]. This trend was also confirmed by the theoretical work of Fratini et al. [134], where it was demonstrated that unlike scattering from intrinsic optical phonons, remote SP scattering, results in a density dependent conductivity $\sigma \propto | E_F |$.

3.6.4. Effect of SP on IOP lifetimes of graphene

Fitting the experimental transient optical conductivity measurements to the model discussed earlier in this chapter, various values for the IP lifetimes have been inferred. As we stressed previously, no substrate-coupled energy relaxation channels are considered in this model which could render the inferred substrate independent IP lifetimes, derived by Wang et al. [102] questionable. Unlike optical conductivity pump probe techniques, where the lifetimes of the optical phonons are indirectly deduced from the relaxation of the hot carriers, in time resolved Anti-Stokes Raman (ASR) method, one can implicitly derive the optical phonon lifetimes of graphene from the inverse of the linewidth of different Raman modes. The advantage lies in the fact that this method will not have unwanted sensitivity to carrier-carrier contributions or recombination, providing a direct measure to monitor the population and lifetimes of zone center optical phonons .[143][119]

The optical phonon lifetimes of graphite, monolayer and multi-layer graphene on SiO_2 were studied by Kang et al. [143]. Using ASR spectroscopy, a shorter lifetime $\sim 1.2\ ps$ was observed for monolayer graphene as opposed to $\sim 2.4\ ps$ for graphite. Based on these temperature dependent measurements, it is concluded that the shorter lifetime of single layer graphene is due to the additional decay channel through the surface phonons of the substrate. In 2012, using the same method, Wu et al.[119] studied the dynamics of suspended, supported and gated exfoliated graphene. They claimed that hot phonon lifetimes do not show any dependence on the Fermi level or excitation fluence but are considerably dependent on the layer number and whether or not graphene is suspended. Optical phonon lifetimes of 1.5 , 2.0 and $2.2\ ps$ are derived for mono, bi and tri-layer graphene respectively and an optical phonon lifetime of $2.0\ ps$ is derived for suspended mono layer graphene. They explain these results invoking an additional relaxation channel through either remote SP scattering or direct scattering between phonons of graphene and phonons of the substrate.

Figure 3.19. (a) shows the optical phonon populations at $5\ J/m^2$ and $2.5\ J/m^2$ fluences for graphene supported on SiO_2. One can see that doubling the fluence, increases the optical phonon population by 10 fold. Based on this figure, Wu et al. claim that the change in the

optical phonon lifetime is negligable as the fluence is increased. However, upon closer examination, we notice that the data especially at longer time delays is too sparce to make a definite conclusion. In addition, at shorter delay times, the lower fluence data seems to have a faster relaxation, which is consistant with our measurements. Furthermore, the paper mentions that the measurements were performed at 4 different fluences, however, only two of these are included in the text, which makes drawing the fluence-independent conclusion harder. The same data interpretation line is used to draw the conclusion that optical phonon lifetimes are "nearly" independent of Fermi level and carrier temperature, which is contradictory to the studies done in refrences [118][144][120].

A more complete and conclusive study with a more methodical fluence dependent data interpretation, was done by Gao et al. [118] where they compared the dynamics of supported and suspended CVD graphene and observed a longer carrier relaxation time for supported graphene. Figure 3.19.(b) shows a bi-exponential decay for the transient reflection of supported and suspended graphene, where the faster decay of supported graphene is attributed to a combination of carrier coupling to IP and SP channels.

The SP relaxation pathway is known to *decrease the hot phonon effect and lower the optical phonon lifetimes of graphene.* [132][134] In this study, the longer decay time τ_2 for supported graphene is attributed to the hot phonon effect or the relaxation of the accumulated intrinsic optical phonons, which presents a bottleneck for the energy drainage. At higher carrier densities, carrier relaxation is controlled by the lifetimes of intrinsic optical phonons; as a result, *at higher fluences,* τ_2 *can potentially reflect the lifetimes of these hot optical phonons,* where it is found to be $\sim 1.2\ ps$ for graphene supported on glass and $1.8\ ps$ for suspended graphene.(It is important to note that this reduction in the lifetime, could be due to the carriers of graphene coupling to the surface phonons or direct coupling of the graphene phonons to the bulk phonons of the substrate.)

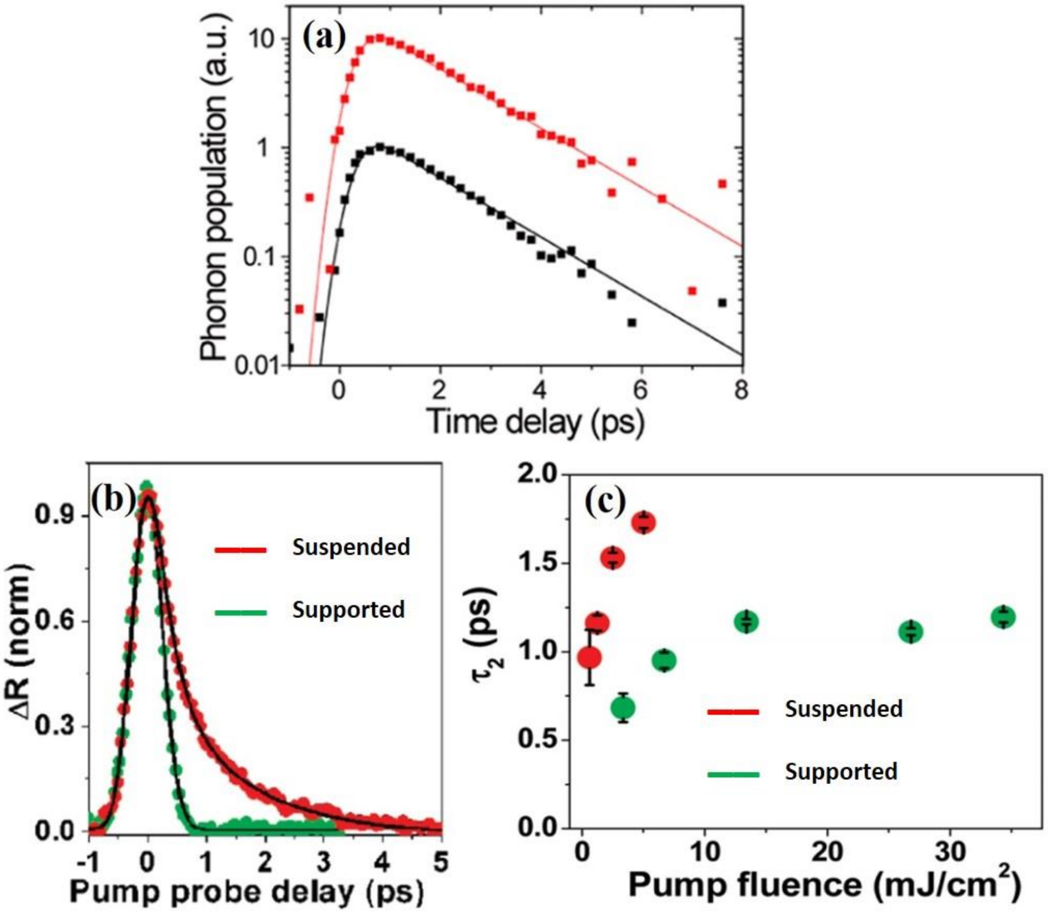

Figure 3.19. (a) Phonon population measurements at different pump fluences: 5.0 J/m^2 (Red) and 2.5 J/m^2 (Black). [119] **(b)** Transient absorption response for suspended (Red) and supported (Green) graphene at a fluence of 2 mJ/cm^2. **(c)** Fluence dependence of the slow decay constant τ_2 for suspended (Red) and supported (Green) graphene.[118]

To confirm this speculation, the optical phonon populations for suspended vs supported graphene were compared using the ratio between anti-Stokes and Stokes Raman signals. A much higher optical phonon population for suspended graphene is observed, leading to the conclusion that when there is substrate coupled relaxation channel, the carriers in graphene relax mainly through SP scattering rather than IP scattering. This in turn results in a smaller IP population for substrate supported graphene. Figure 3.19. (c) shows an increase in τ_2 as the fluence is increased, which is similar to the trend observed in our measurements which we will discuss shortly.

In this section, we highlighted the fact that the surface optical phonons of polar materials can not only affect the electronic properties of graphene but also alter the intrinsic optical phonon lifetimes and phonon populations. Since almost all SP related ultrafast studies have been focused on the comparison of suspended vs supported graphene, we close this gap of knowledge by methodically studying the ultrafast optical response and femtosecond carrier dynamics of graphene on different substrates. In the following section we will invoke a multi-channel relaxation theory involving surface optical phonons, intrinsic optical phonons and the latter's decay into lower energy intrinsic phonons to explain the substrate-dependent dynamics as well as the observed substrate-dependent relaxation times of single layer graphene.

3.7. Transient transmission in the presence of surface optical phonons

The substrate dependent ultrafast transmission response of graphene on quartz, sapphire and single crystalline diamond are shown in Figure 3.20. The single color pump probe experiments were done at an excitation energy of $1.6\, eV$ with a constant fluence of $9.6\ \mu J/cm^2$. For an accurate comparison of the graphene dynamics, extra measures were taken to ensure that the observed differences are not due to the discrepancies arising from the different conformity levels of graphene to the different substrates or the fabrication variations. Accordingly, as discussed earlier, all studied substrates possess a comparable sub nm surface roughness and the CVD graphene used in this study is from a single growth batch and transferred on the target substrates in parallel and at the same time. A close look at Figure 3.20 shows that the notable differences in the observed dynamics of graphene on different substrates are: (1) the amplitude of the positive peak, (2) the relative positive to negative peak ratio representing the inter vs intraband transition interplay (γ), and (3) the relaxation times of the carriers.

Based on the parameters presented in Table 3.2. and the steady-state optical conductivity measurements in reference [139], the more polar nature of sapphire and its higher effective Fröhlich coupling constant, leads to *stronger SP interactions for graphene on sapphire compared to graphene on quartz*. [129][139] Unlike intrinsic diamond, which is a non-polar material with a low static dielectric constant, hydrogenated diamond is known to be a highly polar surface with a high static dielectric constant.[145][146] containing highly energetic surface vibrational modes $\sim 0.34\ eV$ associated with $C-H$ bonds, as well as, lower energy surface phonon modes.[147][148] In addition, as previously discussed, the SP coupling strength decreases considerably as the intrinsic doping or the static Fermi level of graphene is increased. [128][134][138] Looking at the shift in the Fermi level E_F presented in Table 3.1 (estimated from the Raman mapping of the target areas of the 3 samples), one can conclude that surface phonon coupling effects are much stronger and further amplified for graphene on diamond with a Fermi level $\sim 0.2\ eV$, compared to graphene on sapphire with $E_F \sim 0.27\ eV$ and quartz with $E_F \sim 0.35\ eV$.

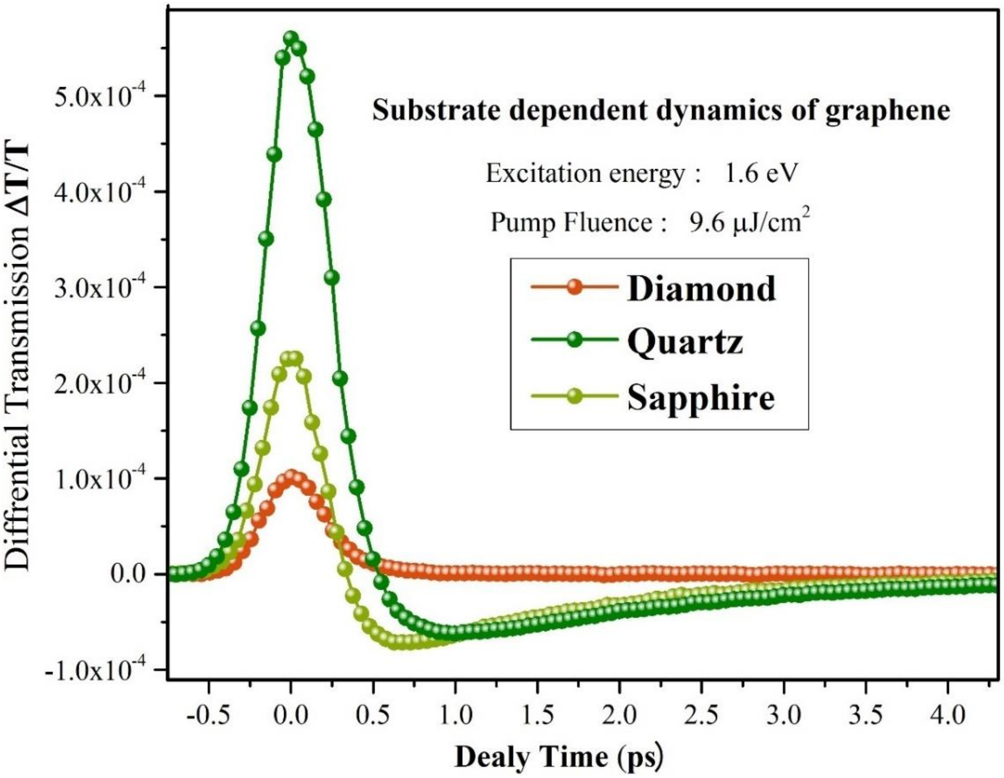

Figure 3.20. Transient transmission response of graphene on diamond, quartz and sapphire. The excitation and probing energy for all measurements are 1.6 eV at a pumping fluence of 9.6 μJ/cm^2

3.7.1. Effect of substrate on the band filling dynamics of graphene

As seen in Figure 3.20, when excited at the same energy and fluence, the band filling dynamics, or the amplitude of the positive peak of transmission ΔT, is strongest for graphene on quartz and weakest for graphene on diamond. Given the fact that the SP scattering rate or the carrier cooling power due to the surface phonons of the substrate is significantly higher than the IP channel in our relevant pumping energy range, [128][138][140] surface phonons can rapidly deplete energy from the hot electron system and lower the carrier temperature before the thermalization between the carriers and the IP bath sets in. The stronger and the faster the SP channel, the more efficient the depletion of energy from the probed state $(0.8\, eV)$ and the faster the drop in the transient electronic temperature T_{el} in that time window will be.

The dynamical femtosecond optical response of graphene is closely linked to the temporal evolution of the carrier temperature (T_{el}). As a result, at each time window, depending on the electronic temperature, the optical conductivity (hence, the transient transmission response) of graphene will be different. As discussed earlier, at higher carrier temperatures, the interband transitions or band filling dynamics are more dominant. Since the SP channel in diamond is very strong, the sharp fall in the electronic temperature in the first 100 fs, will result in a cooler electron distribution and a smaller amplitude of the PB peak seen in Figure 3.20. Accordingly, the lower SP coupling of graphene on quartz compared to other substrates, leads to a hotter electronic distribution at this target time frame and hence, a more pronounced bleaching effect which is presented as the large amplitude of the positive peak in ΔT.

3.7.2. Effect of substrate on the induced carrier absorption of graphene

Figure 3.21 shows the normalized transient transmission response of graphene on different substrates after the initial bleaching of transitions. With $\gamma_{\text{diamond}} = 1$, $\gamma_{\text{quartz}} = 0.88$ and $\gamma_{\text{sapphire}} = 0.66$, it is clear that the decrease in ΔT due to the dominance of the intraband transitions or induced carrier absorption is strongest for sapphire and weakest for diamond.

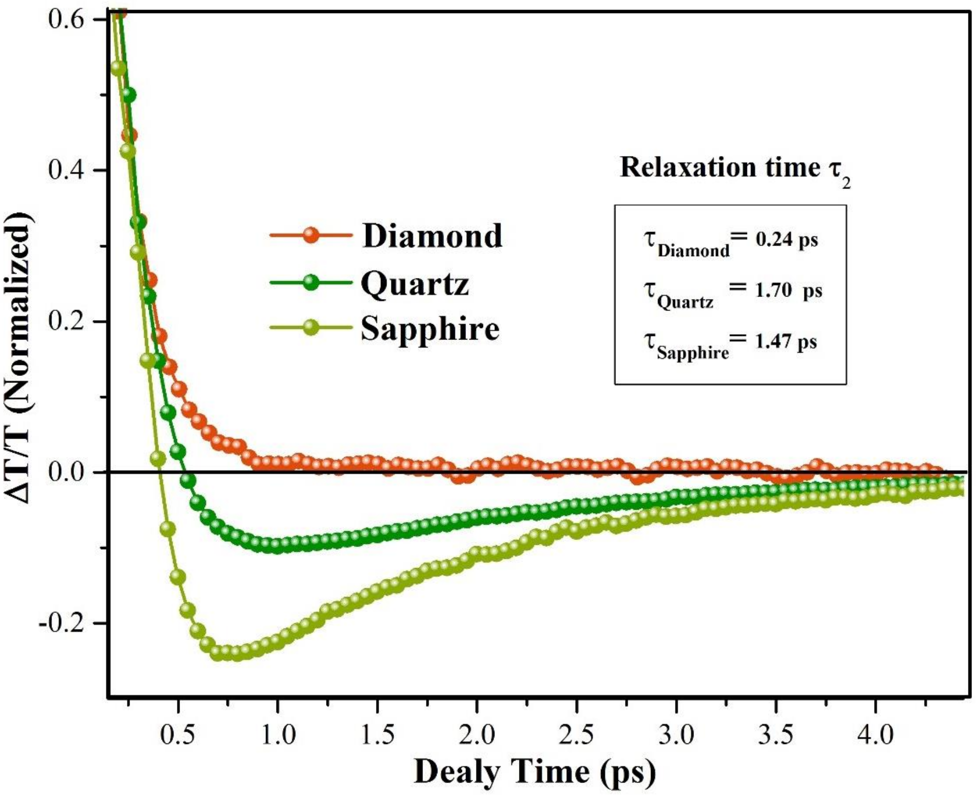

Figure 3.21. Normalized transmission response of graphene on diamond, quartz and sapphire for an excitation energy of 1.6 eV and a fluence of 9.6 µJ/cm^2. The slow recovery is fit to a mono exponential with the best fitting for relaxation time ~ 0.24 ps for diamond, 1.47 ps for sapphire and 1.7 ps for quartz.

To explain these differences, one needs to recall that the transient changes in the electronic temperature of graphene are dependent on the competition of the different relaxation channels and their associated timeframes. After the initial carrier-carrier scattering and thermalization into a Fermi Dirac distribution, the subsequent activation of the surface phonon relaxation channel, results in the bulk of the electronic energy moving closer to the highest frequency mode of these surface vibrations in a very short time window. Given that the most energetic surface phonon modes of diamond, quartz and sapphire are: 0.34, 0.14 and 0.11 eV respectively, in this time frame, the electronic distribution will be hotter for graphene on diamond compared to other substrates.(Figure 3.22) Therefore, due to the dominance of the interband transitions, ΔT will be more positive for graphene on diamond, whereas, the lower energy surface phonon mode of sapphire results in a cooler energy distribution and a more enhanced intraband absorption as seen in Figure 3.21. Although the IP channel will alter the energy distribution in approximately the same time window, nevertheless, the high energy surface phonon mode of diamond will still result in a hotter electronic distribution in comparison to sapphire and quartz.

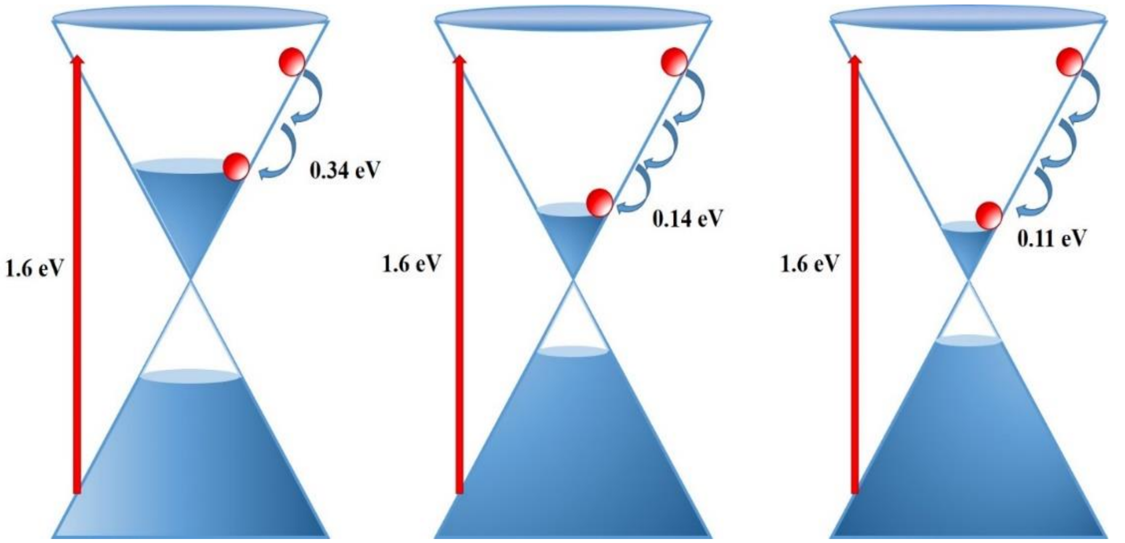

Graphene on diamond **Graphene on quartz** **Graphene on sapphire**

Figure 3.22. Illustration of the thermalization process through surface phonon scattering for pristine graphene on diamond, quartz and sapphire with their respective highest surface phonon mode energies of 0.34 eV, 0.14 eV and 0.11 eV. In this time window, the distribution is hottest for graphene on diamond and coolest for graphene on sapphire.

3.7.3. Effect of substrate on the carrier relaxation times of graphene

As discussed previously, the fast decay component in the ultrafast optical conductivity of graphene (τ_1), is attributed to the rapid carrier-optical phonon thermalization. [105] [110] [149] This decay time is instrument-limited in in our measurements of graphene on diamond. However, the slow decay component (τ_2), which is attributed to the bottleneck created by the hot phonon effect or the slow relaxation of the thermalized carrier-IP bath through the lower energy intrinsic phonons[102][118][149], can be resolved for all three substrates. The noted relaxation times τ_2, shown in Figure 3.21 are obtained by fitting the slow recovery portion of the relaxation dynamics to a mono exponential decay with $\tau_{2\,(Diamond)}{\sim}0.24\,ps,$ $\tau_{2\,(sapphire)}{\sim}1.47\,ps$ and finally, $\tau_{2\,(Quartz)}{\sim}\ 1.70\,ps.$ The interaction between carriers of graphene and polar modes of the substrate are believed to have two distinct effects: [118][119][137][138][140][143][150]

1- Lowering the number of generated intrinsic optical phonons. (The faster scattering rate of the surface optical phonons results in a faster energy drainage from the electron system and consequently results in a lower number of IP’s being generated.)

2- Decreasing the IP lifetime through either direct coupling of the substrate bulk phonons to the phonons of graphene or the discussed carrier-substrate surface phonon coupling.

Among the three studied substrates, SP channel in quartz will be the least efficient in reducing the IP lifetimes. As a result, due to the larger number of hot IPs whose relaxation to lower energy phonons will create a bottleneck, the carriers of graphene on quartz will take longer to relax. ($\tau_{2\,(Quartz)}{\sim}\ 1.70\,ps$) On the other hand, the highly polar nature of the hydrogenated diamond, compounded by the low intrinsic doping of graphene on this substrate, leads to a strong carrier-SP coupling which results in a rapid relaxation of $\sim 200\ fs$. In addition, due to the similar and particularly large zone edge and zone center optical phonon frequencies of graphene and diamond, an extra relaxation channel through direct phonon-phonon coupling between graphene and diamond is highly possible. This could further assist in the carrier relaxation process.[147][151]–[154]

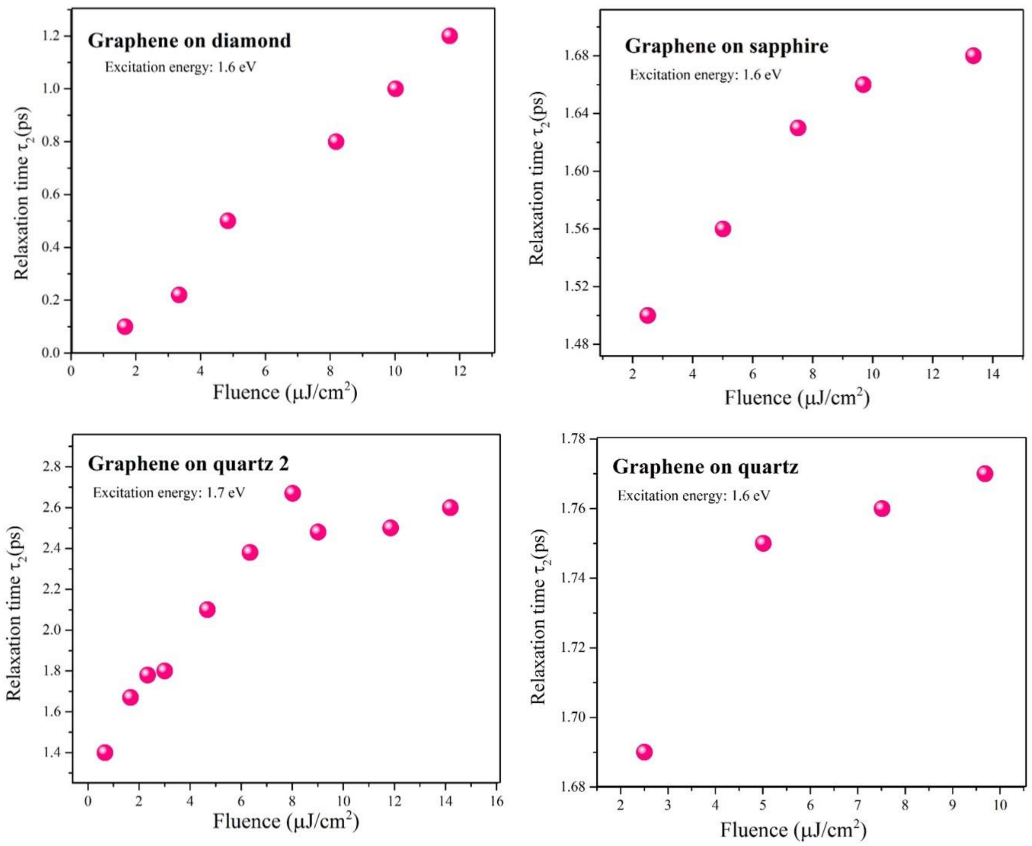

Figure 3.23. Slow relaxation time τ_2 is plotted against pump power for graphene on diamond, sapphire and two different quartz substrates with different dopings. The time constants were obtained by fitting the slow relaxation dynamics to a mono exponential decay.

For further analysis, we carrier out a comprehensive set of photoexcited carrier density dependent measurements shown in Figure 3.11. We extracted the carrier relaxation time τ_2

at each fluence for the three different substrates. The fluence dependence of τ_2 is shown in Figure 3.23 where the results from an additional quartz sample is also included. (The 2nd quartz is a commercially available and commonly used optical grade substrate, with a lesser overall surface polish. It is important to note that the graphene transferred on the 2nd quartz is not from the same batch as the 3 other samples)

The present results from Figure 3.23 show that, for all substrates, the relaxation times of carriers in graphene increase with the increasing fluence. This unexpected trend was verified for a number of different samples and different excitation energies. In the low fluence regime used in our experiments, the carrier-IP scattering rate increases with increasing carrier density. [106] If the intrinsic optical phonons were the only cooling channel available to the carrier of graphene, the increase in the photoexcited carrier density would result in a faster decay of carriers due to the increased possibility of electron- optical phonon scattering.

Consequently, the observed increase in τ_2 as the pumping fluence is increased, is a further confirmation of the existence of an *additional* energy relaxation channel through surface phonons of the underlying substrate which can compete with the IP channel in cooling of the photoexcited carriers. The strength and efficiency of this competition will be highly dependent on the applied fluence regime. At lower fluences, the SP channel will be efficient enough to decrease the carrier relaxation and optical phonon lifetimes, but at higher fluences where more IP's are created, there will be a buildup of generated intrinsic optical phonons which will in turn create a bottleneck for the energy relaxation and render *longer* carrier decay times as observed in our experiment. At high enough fluences, where

IP is the dominant energy relaxation channel, the slower tail of the experimental dynamics, can potentially reflect the intrinsic optical phonon lifetimes of graphene.[118] [155] [156]

Figure 3.23 shows that at higher fluences, for graphene on sapphire and both quartz substrates, τ_2 tends to reach a constant value. For graphene on quartz 2, where the conformity of graphene and the substrate is not optimal, at high fluences we have $\tau_2 \sim 2.5\ ps,$ which is similar to the optical phonon lifetimes of graphite measured by time-resolved incoherent Anti-Stokes Raman spectroscopy. [143] The decay constant converges toward 1.6-1.7 ps for graphene on sapphire and smoother quartz which is in the range of the reported optical phonon lifetimes for single layer graphene. Within the range of our experimental pump powers, the carrier relaxation times for graphene on diamond are considerably smaller and do not reach a saturation. This behavior is consistent with the depicted picture in which the strong SP channel for graphene on diamond not only assists in the relaxation of carriers, but also reduces the number of generated IP and the hot phonon effect.

3.8. Conclusion

In this chapter, we methodically studied the effect of substrate on the relaxation dynamics of carriers and phonons in graphene using ultrafast transient transmission pump probe spectroscopy. Based on a comprehensive set of fluence and excitation energy dependent measurements, we established that the temporal evolution of the carrier temperature in graphene, strongly depends on the underlying substrate. We further demonstrated that these differences cannot be simply accounted for by the change in the static Fermi level of graphene caused by each substrate. We believe that the sub nm roughness of the studied substrates: quartz, sapphire and single crystal diamond, enables a strong coupling between the energetic carriers of graphene and surface optical phonons of the polar substrates. Accordingly, a multi-channel cooling picture involving surface phonons of the substrate and intrinsic optical phonons of graphene was employed to explain the observed differences in the ultrafast transmission response of graphene on different substrates. The increase in the relaxation times as the fluence is increased, further validates the existence of this non-negligible additional cooling pathway that can compete with the intrinsic optical phonons of graphene in cooling the electron distribution and decreasing the intrinsic optical phonon lifetimes.

CHAPTER

4. PHOTO RESPONSE OF CURLED GRAPHENE RIBBONS

4.1. Introduction

Graphene is considered a promising material in the electronics arena due to its high charge-carrier mobility, optical transparency and broadband absorption. [34] [31][14] However, lack of a bandgap, in addition to the poor intrinsic photocurrent response of pristine graphene, has introduced a challenge in the efficient use of graphene in photovoltaic devices. As a result, enhancing graphene's photon-to-electron conversion rate is the next step towards an efficient energy harvesting technology. Different avenues have been taken to improve the performance of graphene based photodetectors by increasing the efficiency of converting light into electric signals. The two different mechanisms discussed for photocurrent generation in the literature are: built-in electric field at the graphene-metal interface and photo thermoelectric effect (PTE).[157]–[160] Photo thermoelectric effect is a novel nonlocal hot-carrier-assisted transport regime and is expected to increase power conversion efficiency in graphene-based energy harvesting devices.[161] It is, therefore, desirable to synthesize graphene nanostructures with an intrinsic PTE-induced photocurrent response.

Modifying graphene's morphology and consequently altering its optoelectronic properties is an attractive option that can be pursued to enhance the photo response of graphene. In this chapter, we introduce a new morphological form of graphene called curled graphene ribbon (CGR). Although some of the morphologically modified graphene structures in the literature have shown distinct properties compared to pristine graphene, none but CGR have demonstrated an enhanced photocurrent response, which is a key component for future photovoltaics. In this chapter, we investigate the nature of this enhanced photo response in suspended CGR via scanning photocurrent microscopy. The results in this chapter have been published in [162].

4.2. Morphology of graphene

Modifying graphene's intrinsic properties by simply altering its morphology, is an attractive option that has driven a thriving research field. Dimensional confinement approach, although riddled with difficulties pertaining to the nano fabrication process and edge control, has long been practiced and tried extensively. The quantum confinement of charge carriers in graphene nano ribbons (GNR) is shown to open a finite band gap which scales inversely with the width of the ribbon.[163] There exist many different approaches to fabricating GNRs. In 2009 Kosynksin et al. [164] showed a chemical approach to longitudinal unzipping of carbon nanotubes to form GNR.(Figure 4.1.a) Selective growth of GNR on SiC by ion implantation and lithography patterning methods are other alternatives for graphene nanoribbon synthesis.[165]–[167]

Another interesting morphological form of graphene is known as carbon nano scrolls (CNS).(Figure 4.1.b) Carbon scrolls are jelly roll-like wrapping of a graphene sheet into a one dimensional tubular structure.[168] This hybrid of graphene and carbon nanotubes has properties that are clearly distinct from both CNT and graphene. A simple fabrication process by Xie et al. was introduced in 2009 involving the use of isopropyl alcohol (IPA) for effective rolling of sheets of graphene into CNS.[169] Raman spectrum of CNS confirms that the electron and phonon dispersions for CNS are slightly different from those of graphene or carbon nano tubes.

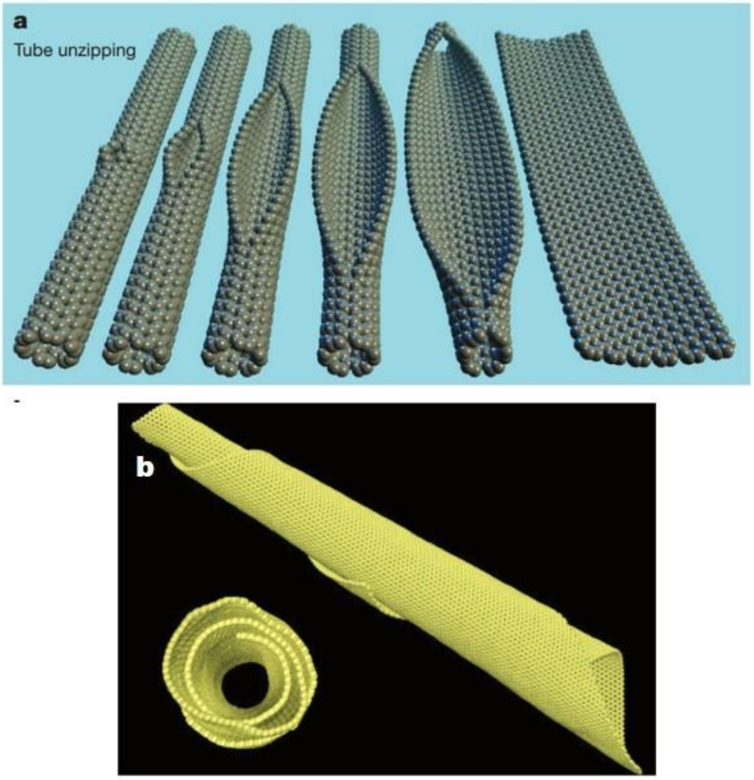

Figure 4.1.(a) Schematics of the gradual longitudinal unzipping of a carbon nanotube resulting in a flat graphene nano ribbon.[164] **(b)** Top and side view of a carbon nano scroll obtained by dynamics simulation.[168]

Graphene, the atomically thin membrane, can be easily folded into complex shapes, creating distinct properties that can be potentially controlled. It has been shown that the deformation of sigma bonds caused by the curvature in graphene folds, can result in charge transfer between the out of plane sigma bonds and the π orbitals, which can change the chemisorption and molecular adhesion of graphene.[170] Kim et al. have studied grafolds or the origami folding of graphene into multiple folds.(Figure 4.2.a) They show that the electronic band structure of graphene is changed during the process and the occupied states in the vicinity of the Fermi level are localized close to the folded sections.[171]

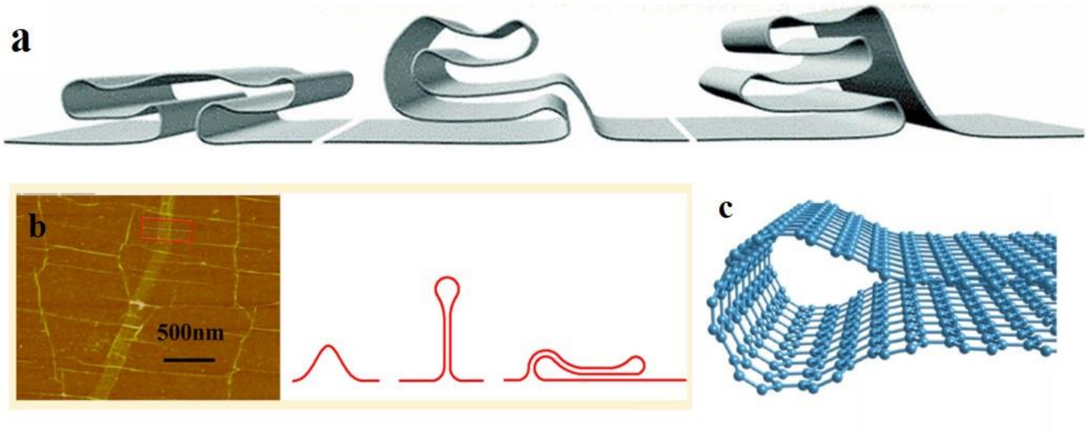

Figure 4.2. (a) Various complex folding of graphene membrane including a quadruple folding and a box pleat as simulated by Kim et al. [171] **(b)** Figure on the left shows an AFM image of graphene on SiO2/Si substrate including folding and wrinkling of the graphene membrane. The figures on the right, show schematics of simple ripple, standing collapsed wrinkle and a folded wrinkle respectively.[172] **(c)** Simulation results of tight-binding atomistic calculations done by Ortolani et al. [170] of a 3D renderization of zigzag folded graphene membrane.

In the context of fold formation, ubiquitous graphene wrinkling caused by the growth and transfer processes, have been studied where it is shown that the wrinkles can reach a defined maximum height before folding over. [172] (Figure 4.2.b) The quantum transport calculations show that, transport through the collapsed wrinkles is limited by a density of states bottleneck and tunneling through interlayers in the collapsed regions. These findings highlight the close relation between electronic properties of graphene and its morphology. Theoretical studies show that the long suspended ribbons of graphene are prone to distortion and formation of a morphological form of twisted graphene ribbons.[173] [174] Cranford et al. [174] found a distinct transition from a saddle like twisted structure to a coil like helical configuration as a function of number of graphene layers and amount of rotation in graphene nano ribbons. (Figure 4.3) These results are explained as a transition towards a more energetically stable molecular configuration and a more uniform distribution of strain in these twisted ribbons.

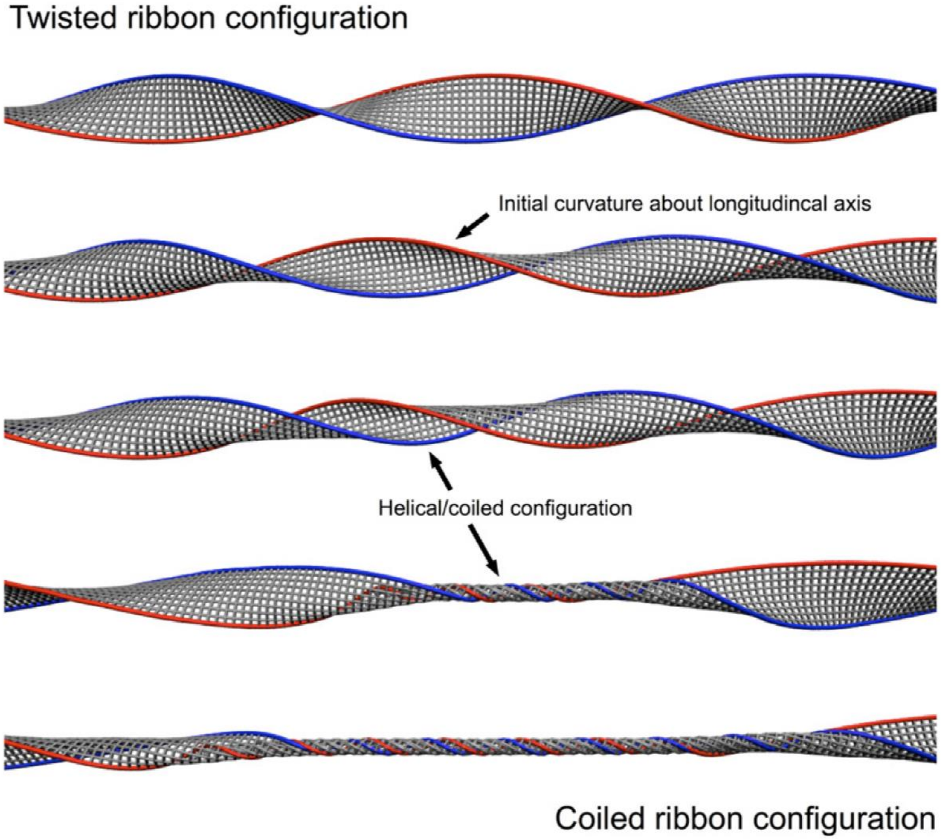

Figure 4.3. Simulation results of twisted ribbon transformation into a coiled ribbon configuration. Opposite edges are marked red and blue for clarity. The images from top show a regular twisted ribbon that further collapses into a coiled configuration which asserts a more homogenous strain on the whole structure. Less strain energy is required for the coiled morphology. [174]

In an effort to enhance the photocurrent response of graphene, we have engineered a novel morphological form of suspended graphene called curled graphene ribbons (CGR). Figure 4.4 shows SEM images of these structures suspended over trenches of 5 μm width and 5 μm depth etched into fused silica substrates. In the next section we will review the fabrication details for a high yield CGR synthesis.

4.3. Curled graphene ribbon synthesis

The graphene growth and transfer procedures were explained in depth in chapter 2. To synthesize CGR, the growth annealing step is conducted at $1000º\ C$ with 100 $sccm$ of Ar and 10 $sccm$ of H_2 for a duration of one hour. The Ar gas is subsequently turned off and a mixture of the hydrocarbon source CH_4 ($35sccm$) and hydrogen (8 $sccm$) at $950º\ C$ is introduced for 30 minutes. This recipe has been optimized to produce uniform coverage single layer graphene on copper.

We then spin coat a layer of $PMMA\ A2$ with 2% solids on top of the copper foil to act as support. Using oxygen plasma we remove the graphene grown on the back of the copper foil. We consequently etch away the copper using ferric chloride ($FeCl_3$) and rinse off the copper etachant residue using multiple DI water baths. Next, the graphene/PMMA layer is "fished" away with a pre-patterned target substrate where trenches of 5 μm width and 5 μm depth were previously etched into fused silica using Oxford 80 RIE. The sample is then air dried overnight. Since we use a thin low solid content PMMA layer, the suspended graphene structures are more fragile and a more careful handling of the sample is required to avoid the collapsing of the graphene membrane.

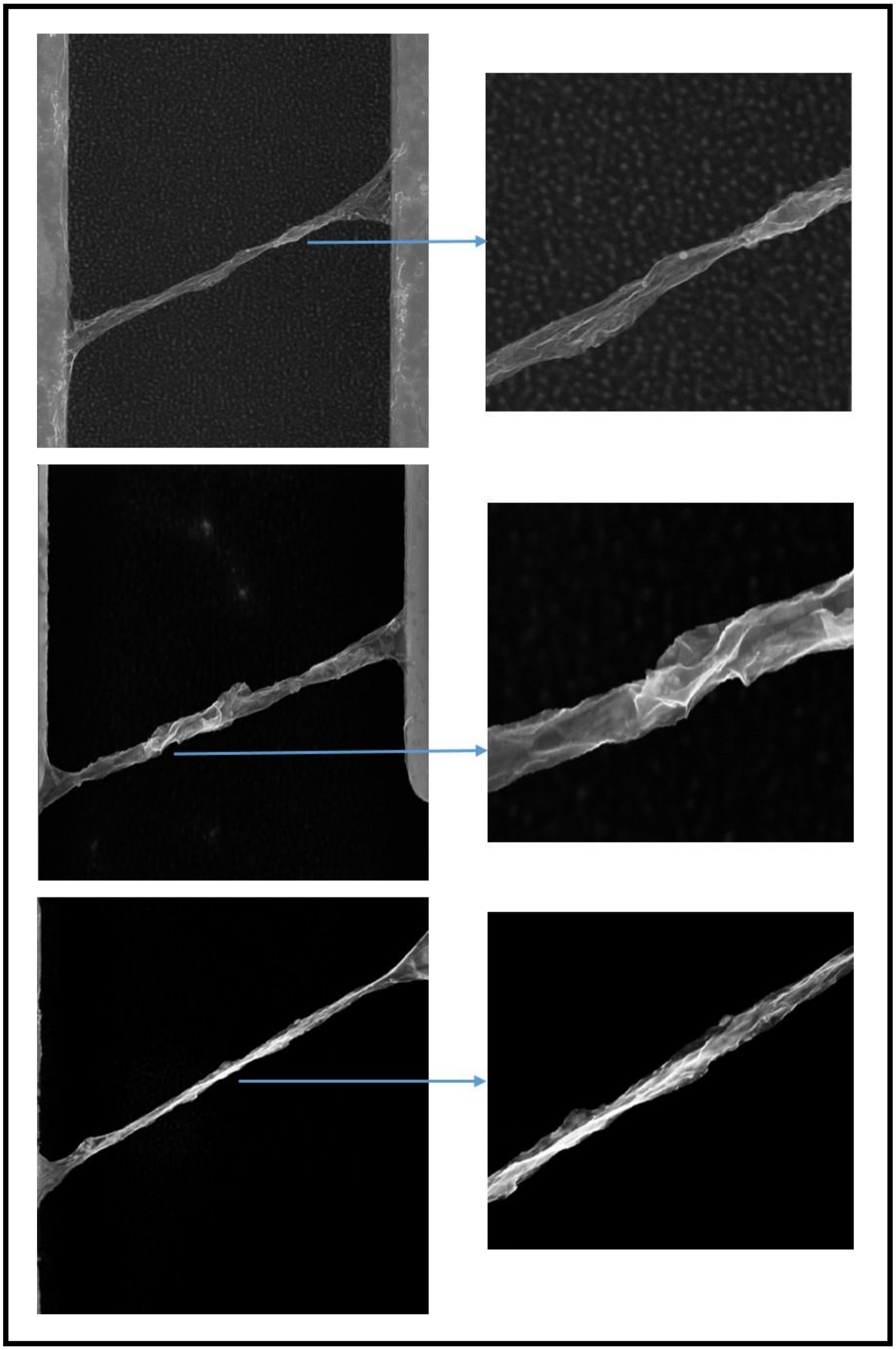

Figure 4.4. SEM images of three different curled graphene ribbons suspended over trenches of 5µm width. One can clearly see from the top figure that the most intense curling happens in the middle of the ribbon. The images on the right show a more magnified view of the curling.

We noticed that focusing a high energy electron beam onto the suspended regions of a suspended graphene ribbon can result in rupturing of the membrane and scrolling of the edges in the exposed side. Although these scrolled edges showed interesting photocurrent response, the efforts to have a single suspended curled structure of narrow width was not possible with this approach. In an effort to fabricate a narrow suspended ribbon with curled and scrolled edges, we correspondingly experimented with shooting the membrane with focused laser beams of high fluence. Although this method seemed more successful, the required accuracy and the low yield of curled graphene formations prompted us to try a different method which proved to be much more successful.

The method devised is a shock annealing technique where the bulk of the PMMA is first dissolved in a solvent bath with acetone and rinsed with IPA and subsequently annealed in hydrogen and argon in an already hot furnace at $420\ ^{\circ}C$. The CGRs created by this method are narrow, with a sub-micron width and a very high yield of ~ 100 CGR per cm. During the evaporation process, the supported graphene effectively adheres to the silica substrate through Van der Waals interactions, meanwhile the suspended section over the trench wrinkles and subsequently shrinks and curls into a CGR morphology.

With further optimization, we discovered that a higher solid content PMMA results in lower number of CGRs per synthesis. The same trend was observed for thicker layers of PMMA with the same solid content. These results could be attributed to the "stiffness" of the support layer which inhibits the dynamic structural deformation of the suspended membrane. It was also observed that temperatures lower than the degradation temperature of PMMA $\sim 320\ ^{\circ}C$ [175], were not very effective in CGR formation and mostly resulted in formation of suspended flat ribbons of varying widths. To fully understand the underlying mechanisms behind CGR formation through shock annealing, MD simulations were performed in a collaborative effort with Pantelides group at Vanderbilt University.

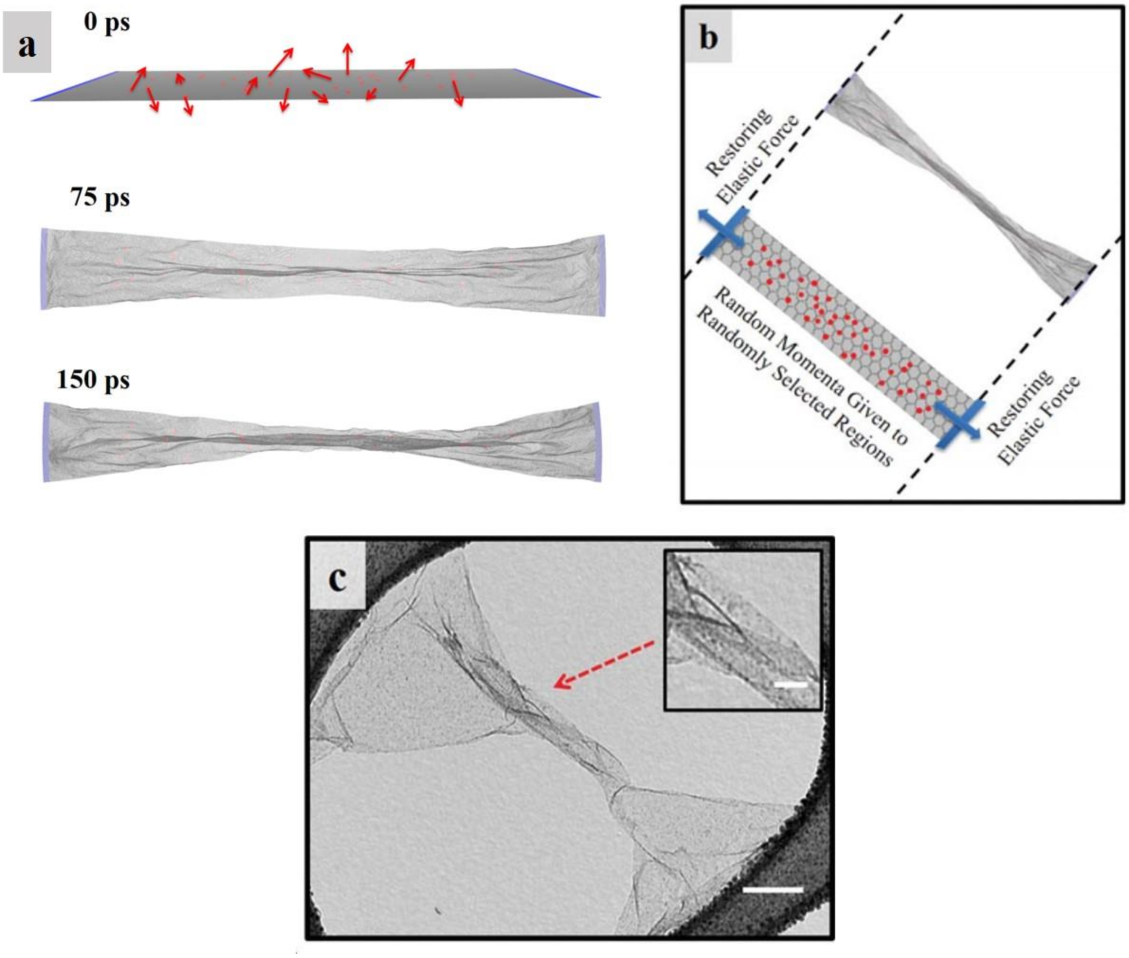

Figure 4.5. (a) MD simulations of CGRs, MD simulation cell with a restoring elastic force $F = kx$ at each end and random momenta given to randomly selected regions along the flat ribbon (top) and the simulated CGR structure after different relaxation times: initial folding after 75 ps (middle) and curled structure forming after 150 ps (bottom). **(b)** View of the CGR formation from the top **(c)** TEM image of a CGR. The scale bar is 200 nm. The inset shows a close-up image of the curled area with a scale bar of 50 nm.

4.4. MD simulations

Classical MD simulations were carried out using the LAMMPS package.[176] A bond-order potential (LCBOP)[177] was used to model the atomic interactions and included intrinsic long-range order interactions between the layers. The simulations in Figure 4.5 were performed using micro canonical (NVE) ensemble ohn a 1-μm-long and 0.1-μm-wide graphene ribbon containing 3,840,000 carbon atoms. During the system equilibration before dynamic deformation, the simulation box dimensions' parallel to the graphene surface were fixed to correspond to the equilibrium lattice constant of unstrained graphene at $T = 300K$. The structural evolution during temperature annealing was simulated to mimic desorption of PMMA molecules. Groups of atoms were randomly selected in the graphene nanoribbon and given random momenta at the initial time. (Figure 4.5. (a) top) To accelerate the structural deformation, the momentum value was chosen to be equivalent to a temperature increase of ~ $2500\,K$, while the total momentum remained zero. Meanwhile, the average temperature remained close to $400\,^{\circ}C$, which is similar to the experimental value. Boundary conditions for the larger dimension kept the ends flat with a restoring elastic force $F = kx$, according to the experimental conditions. (Figure 4.5. (b)) Other dimensions had no restraints. After $75\,ps$, graphene nanoribbon formed wrinkles and developed a multilayer-like structure in the middle region. (Figure 4.5. (a) middle)

Within $150\,ps$ after initial momenta were given, the ribbon curled and locally formed multi-layers, resulting in a quasi-one-dimensional structure in the middle. (Figure 4.5. (a) bottom) Several sets of atomic groups and momenta, namely 4 different simulations, were picked to explore the nanoribbon structural evolution. While the tendencies in structural deformations during all the simulations remained the same, the time required for the formation of the curled region in the middle of the nanoribbon varied. The MD simulation results indicate that random momenta produced during the PMMA evaporation process is the main mechanism behind the formation of CGRs.

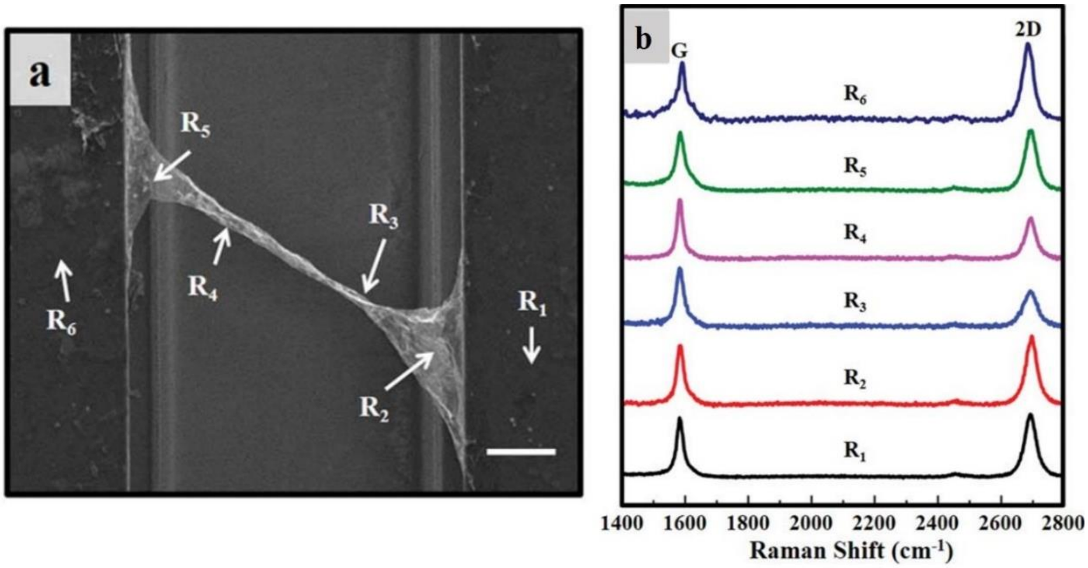

Figure 4.6. (a) SEM image of a CGR structure. The CGR was suspended across a 5 μm-wide and 5 μm-deep trench on fused silica. The white arrows specify the spots where Raman spectroscopy was performed. The scale bar is 1 μm. **(b)** Raman spectra of six different regions along the CGR at 532 nm. The 2D-to-G intensity ratios are greater than 1 in the regions R_1, R_2, R_5 and R_6, indicating the presence of a single layer graphene membrane. The broad 2D bands in the regions R_3 and R_4 may result from the interlayer interactions between different graphene layers within the CGR.

In order to fully understand the structures of CGRs, single layer graphene was directly transferred onto TEM grids coated with lacey carbon films and similar annealing process was adopted to form CGRs. Bright-field TEM imaging was performed on an FEI Tecnai 20T operated at 80 kV. The MD simulated morphology is in good agreement with the TEM image of a CGR (Figure 4.5.c), where it can be seen that a single layer near the edge area and a multi-layer structure in the central area is present. (Figure 4.5. (c) inset)

4.5. Raman Spectroscopy on CGR structure

As discussed in chapter 2, Raman spectroscopy can reveal a wealth of information about the bonding nature between the layers, stacking order and also electron-phonon interactions in graphene.[178] We performed Raman spectroscopy at an incident wavelength of $532\ nm$ along the CGR structure, keeping the power below $1\ mW$. Figure 4.6. (a) shows the SEM image of a CGR and Figure 4.6. (b) shows the corresponding Raman spectra at 6 different locations. The signature peaks of graphene namely G and 2D, at $\sim 1590\ cm^{-1}$ and $\sim 2680\ cm^{-1}$ respectively are present for all 6 locations.

It can be clearly seen that at locations R1 and R6, where graphene is supported by the substrate, the Raman spectra has the characteristics of a single layer graphene with a sharp, symmetric 2D peak, and the characteristic 2D-to-G intensity ratio >1. At R2 and R5 locations, one can observe the same single Lorentzian symmetric 2D peak but the position of both 2D and G peaks have been slightly shifted in addition to the change in the ratio of 2D to G peak intensity. As discussed in chapter 2, the interaction of single layer graphene with the substrate and the change in the Fermi level of graphene induced by the substrate can result in a change in the electron-phonon coupling and evidently a change in the resonance energy of both G and 2D peaks. As one can see from the SEM image of the studied CGR, in both R2 and R5 locations, slight wrinkling is observed. These slightly wrinkled regions can be classified as Turbostratic graphene where layers of graphene are stacked on top of each other without any inherent symmetry or interlayer interactions. As discussed in earlier chapters, the weak interlayer interaction in Turbostratic graphene results in a Raman signature which is close to that of SLG with a 2D peak that can be fit with a single Lorentzian but with a 2D to G ratio that verges on unity as the number of the stacked layers increase.[90]

As we move further to the middle of the ribbon in R3 and R4 regions, the curling and twisting in graphene becomes more and more evident and we observe a substantial decrease in the 2D to G intensity ratio. The 2D bands also become broadened and *asymmetrical*, indicating that more scattering cycles were involved during the second-order double resonance process, which results from the strong interlayer interactions between different graphene layers and is different from the case of Turbostratic graphene.

4.6. Photocurrent response in CGR

The combination of the ultra-high carrier mobility and short carrier lifetimes, makes graphene a candidate for ultrafast photodetectors. This advantage leads to very high bandwidth, zero source-drain bias and dark current operation in these applications.[17][179] However, lack of an intrinsic photocurrent response at zero source-drain bias, which results from the fast recombination of the photoexcited electron-hole pairs before they can be collected, has been a major obstacle. Scanning photocurrent spectroscopy measurements have shown the existence of photocurrent at the graphene-metal junction which is attributed to the local built-in electric field at the interface of graphene and metal electrodes.(Figure 4.7) The magnitude of this internal electric field depends on the difference in the work functions of graphene and the metal.[180] In this case the absorption of a photon leads to the creation of an electron-hole pair which is separated by the internal electric field and leads to the formation of an electric current.[181]–[183]

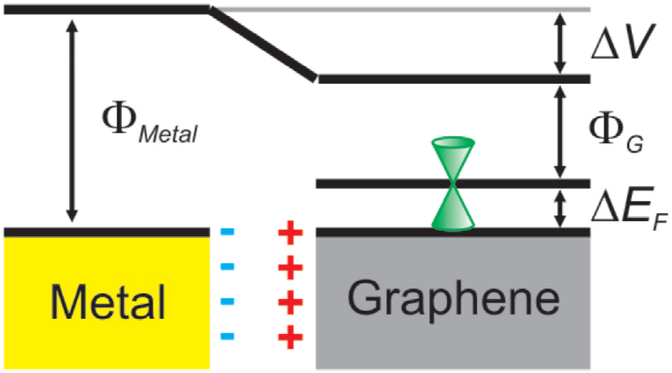

Figure 4.7. Schematics of the energy levels and their alignment due to the built in electric field at the graphene-metal junction. Adapted from reference [193]

A radically different mechanism for enhancement of the photocurrent response is the existence of hot carriers at the graphene p–n junctions through the photothermoelectric effect (PTE).[161][184] Moreover, this novel nonlocal hot-carrier-assisted transport regime is expected to increase the power conversion efficiency in graphene-based energy harvesting devices. In 2010, Xu et al reported observation of a photocurrent response at the interface of a single and double layer graphene.[185] They postulate that while varying the Fermi level, the polarity of the generated photocurrent is opposite of the polarity expected from the photocurrent generation due to the built-in electric field. They explain this phenomenon in terms of the photothermoelectric effect, where a temperature gradient is generated by light, across the interface of two different materials, which possess different thermoelectric powers (S). [161] It is, therefore, desirable to synthesize graphene nanostructures with an intrinsic PTE-induced photocurrent response.

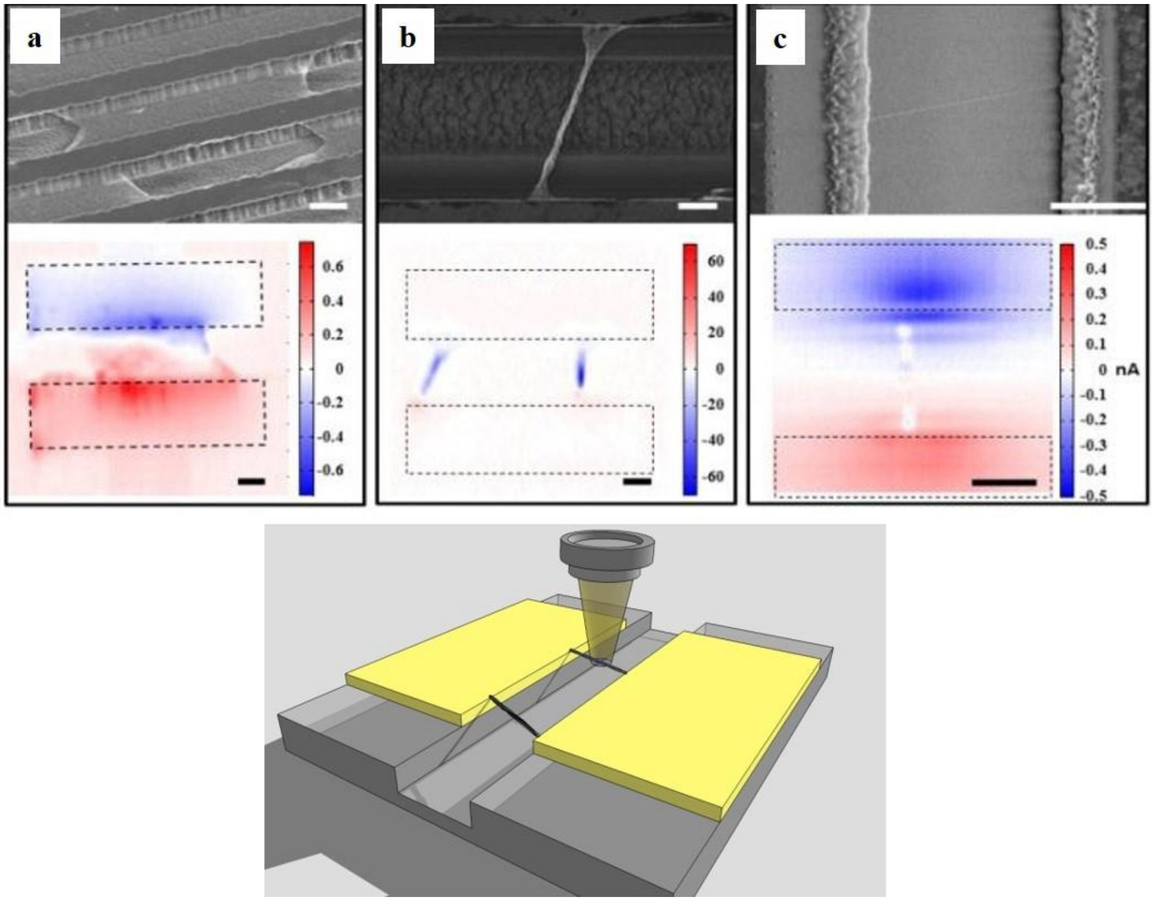

Figure 4.8. SEM images and corresponding photo current response of **(a)** large area suspended graphene ribbons and the corresponding photocurrent mapping (scale bar is in nA) **(b)** Suspended CGR, the dashed rectangles show the placement of the metal electrodes **(c)** Suspended carbon nanotube. Scale bar is 1µm. The bottom image shows the schematics of the experimental photocurrent setup.

As we discussed earlier in this chapter, modifying graphene's morphology and consequently altering its optoelectronic properties is an attractive option that has been pursued extensively. Although some of these structures have shown distinct properties compared to pristine graphene, none but CGR have demonstrated an *enhanced photocurrent response,* which is a key component for the future photovoltaics. We investigate the nature of this enhanced photo response in suspended CGR via scanning photocurrent microscopy in the following sections.

4.6.1. Photocurrent setup

Figure 4.9. (A) shows schematics of the studied CGR transistors. The devices were fabricated on top of a $170\ \mu m$ thick fused silica substrate where $5\ \mu m$ deep trenches were etched as discussed earlier and the source and drain electrodes were deposited with $5\ nm$ of Ti and $40\ nm$ of Pt using e-beam evaporation. The spatially resolved scanning photocurrent microscopy was performed using a CW laser with wavelength of $785\ nm$ and power of $\sim 1.2\ mW$. The laser beam was collimated and focused by a 60X IR enhanced water immersion objective onto a diffraction limited spot and scanned over the suspended CGR location. The photocurrent signal was obtained using a preamplifier with the highest sensitivity within the measurement range and the reflection of the incident laser beam was simultaneously recorded by a Si photodetector. By overlapping the reflection image and the photocurrent image, the position of the sample was located. The photocurrent intensity of a CGR was analyzed by accumulating the photocurrent signal in the central regions of the CGR's spatial photocurrent mapping.

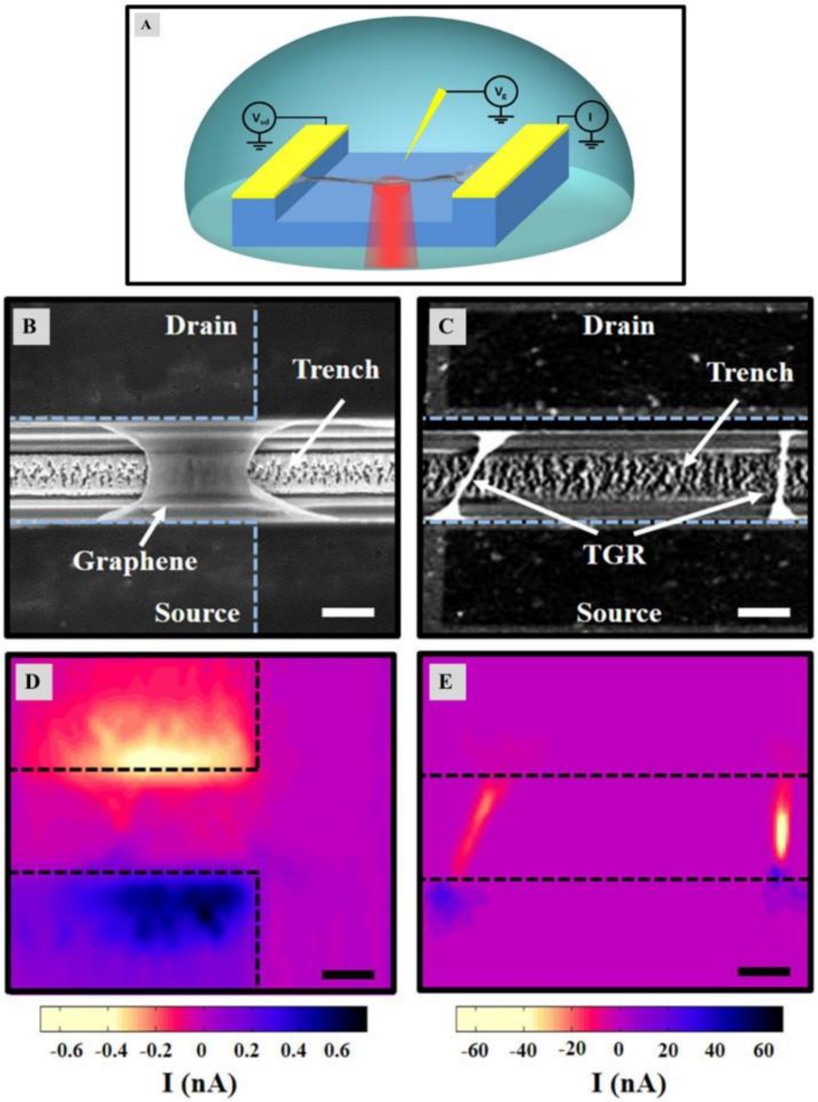

Figure 4.9. **(A)** Schematics of the device geometry. Source and drain electrodes are used to apply a voltage across the CGR and a third electrode is used as an electrolyte gate. A diffraction-limited laser beam with a spot size (< 500 nm) scans over the suspended CGR. SEM images of a suspended SLG**(B)** and a suspended CGR device **(C)**, respectively. The corresponding photocurrent images of the suspended SLG device **(D)** and the suspended CGR device **(E)**, respectively. The scale bars represent 5 μm. Blue and black dashed lines are the edges of the electrodes.

4.6.2. Results and discussion

To evaluate the photon-to-electron conversion efficiency of CGR, we performed spatially resolved scanning photocurrent spectroscopy on a device with suspended CGR channel, in comparison with a flat suspended graphene ribbon channel. (Figure 4.9. (B) and Figure 4.9. (C)) As one can see in the mapping image, the photocurrent generated along a CGR is in the range of tens of nA, which is about two orders of magnitude greater than the photocurrent generated at the graphene-metal contacts in a suspended flat graphene ribbon transistor (Figure 4.9. (B)) and in flat supported graphene ribbon reported by Gabor et al.[161] We observed that the intensity, sign, and symmetries of the obtained photocurrent data, depend on the local morphology of CGR as investigated in the next section.

4.6.3. Photocurrent generation mechanism in CGR

To gain further insight into the mechanisms of current generation in CGR, we needed to be able to change the Fermi level of these curled graphene structures and observe the dependence of the photocurrent on the carrier density. To accomplish this task, we performed gate-dependent scanning photocurrent measurements on CGR transistors where a free-standing CGR was sealed into a microfluidic chamber filled with $1.5\, mM\, PBS$ solution and a gold electrode was used to change the electrochemical potential of the system. The chamber was kept in a steady stream to ensure a homogeneous concentration of ions.

Figure 4.10. (a) displays the SEM image of a CGR, projected on its corresponding reflection image; the photocurrent image of this CGR is shown in Figure 4.9. (b). This photocurrent image was taken at a zero source-drain bias with a gate voltage $Vg = 1.9\, V$.

By sweeping the gate voltage from a value smaller than Vdirac, ($Vdirac = 1.62\,V$ represents the Dirac point of this device) to larger than Vdirac, while recording the photocurrent along the CGR, we obtained the gate-dependent scanning photocurrent map shown in Figure 4.9. (c). As can be seen from the data, the CGR used in these sets of experiments were shown to be p-doped after the growth and transfer processes.

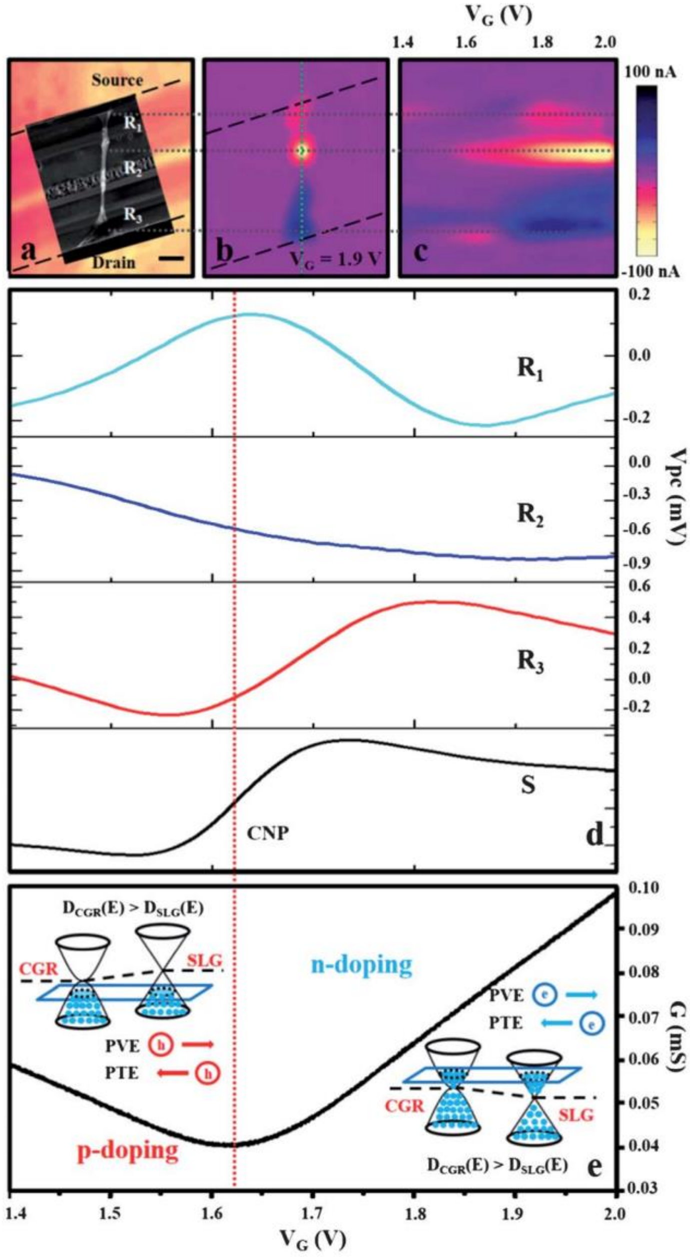

Figure 4.10. Photocurrent responses of a CGR device. **(a)** SEM image of a CGR device projected on the corresponding reflection image. The scale bar is 1 μm. **(b)** The corresponding photocurrent image at Vg = 1.9 V and a zero source-drain bias. The scanning position of the laser beam is indicated by the green dotted line. **(c)** The gate-dependent scanning photocurrent image as Vg is varied from 1.4 V to 2.0 V. **(d)** The horizontal cuts along the dotted lines for different regions (R1, R2, and R3) in the CGR as specified in the photocurrent images. The bottom curve shows the calculated Seebeck coefficient in the R3 region. **(e)** Conductance measurement of the CGR device as a function of Vg. The flow directions for different carriers are illustrated in the inset diagrams

Three regions (R1, R2, and R3) along the CGR were selected for a study of their photovoltage signal (V_{pc}=$I_{pc}R$) evolution as a function of the sweeping gate voltage. As shown in Figure 4.10. (d), the photovoltage signals in the region R3 (R1) exhibit strong non-monotonic gate voltage dependence and have a similar behavioral pattern to the calculated thermoelectric power (S), which may result from the PTE. However, the photovoltage response in the region R2 shows a monotonic gate voltage dependence, indicating that the photovoltaic effect (PVE), resulting from the built-in electric field, plays an important role in the photovoltage generation. It is therefore necessary to consider both PVE and PTE in the photovoltaic generation in CGRs, this inclusion can be expressed as:

$$V_{PC} = V_{PVE} + V_{PTE} = \int (-\frac{\eta}{\sigma(n)} n_x e\, \partial V + S(x) \partial T_e(x))\, dx$$

Where (n) is the local conductivity at the curled area, T_e is electron temperature, η and n_x are the mobility and the density of the photoexcited carriers respectively, and S is the Seebeck coefficient. According to the Mott relation:

$$S = -\frac{\pi^2 k_b^2 T_e}{3e} \frac{d(ln\sigma)}{dV_g} \frac{dV_g}{dE} | E = E_F$$

Where k_b is the Boltzmann constant, e is the electron charge, and E_F is the Fermi energy. $(ln\sigma)/dVg$ derived from the conductance measurement plays a key role in the photovoltage generation from the PTE. On the other hand, the contribution of PVE largely depends on the local potential gradient ΔV.

As discussed previously, the relatively low 2D to G intensity ratio and the broad 2D bands in the curled regions seen in Figure 4.6. (b), may result from the interlayer interactions between graphene planes, which may lead to an increase in the density of states (DOS) in the curled multi-layer regions of a CGR. It is known that the interlayer interaction can induce a parabolic dispersion of the energy bands in multi-layer graphene as opposed to a linear dispersion of the energy bands in SLG.[186][187]

As a result of the Fermi level alignment, the Dirac point of a curled ribbon is higher than that of a single layer graphene leading to the formation of a built-in electric field. As illustrated in Figure 4.10. (e) inset, for an n-doped graphene, the photoexcited electrons flow from the CGR to the SLG due to the built-in electric field. However, according to the second law of thermodynamics, the hot carriers induced by PTE tend to diffuse to the regions with larger DOS to maximize the entropy, leading to an electron flow from the SLG to the CGR. In the region R1 (R3), electrons flow from the SLG to the CGR and produce a negative (positive) photocurrent, which mainly results from the PTE. In the highly curled region R2, the contribution of PVE increases, which overwhelms the PTE-induced electron flow and produces a negative current with the experimental setup used. This confirms that the photocurrent behavior depends on the local morphology of graphene structures. Consequently, we investigated how this local morphology can affect the photocurrent generation.

In order to eliminate the interference from the electrodes, we picked curled ribbons located far from the electrodes (In this instance, single layer graphene acted as the interconnection between CGRs and the electrodes). Figure 4.11 shows a CGR device that exhibits a pronounced negative (positive) photocurrent response in the region R_1 (R_2). Figure 4.11. (c) is the extracted cut of the photocurrent image and illustrates the current changes along the suspended curled ribbon. The PTE-induced photocurrent might be responsible for the negative (positive) current in R_1 (R_2), resulting from the hole injection from the SLG side at the trench edge to the curled area in the middle of the CGR. The symmetric current change indicates that this CGR device might be uniformly curled from the trench edge to the middle of the curled ribbon (the junction between regions R_1 and R_2).

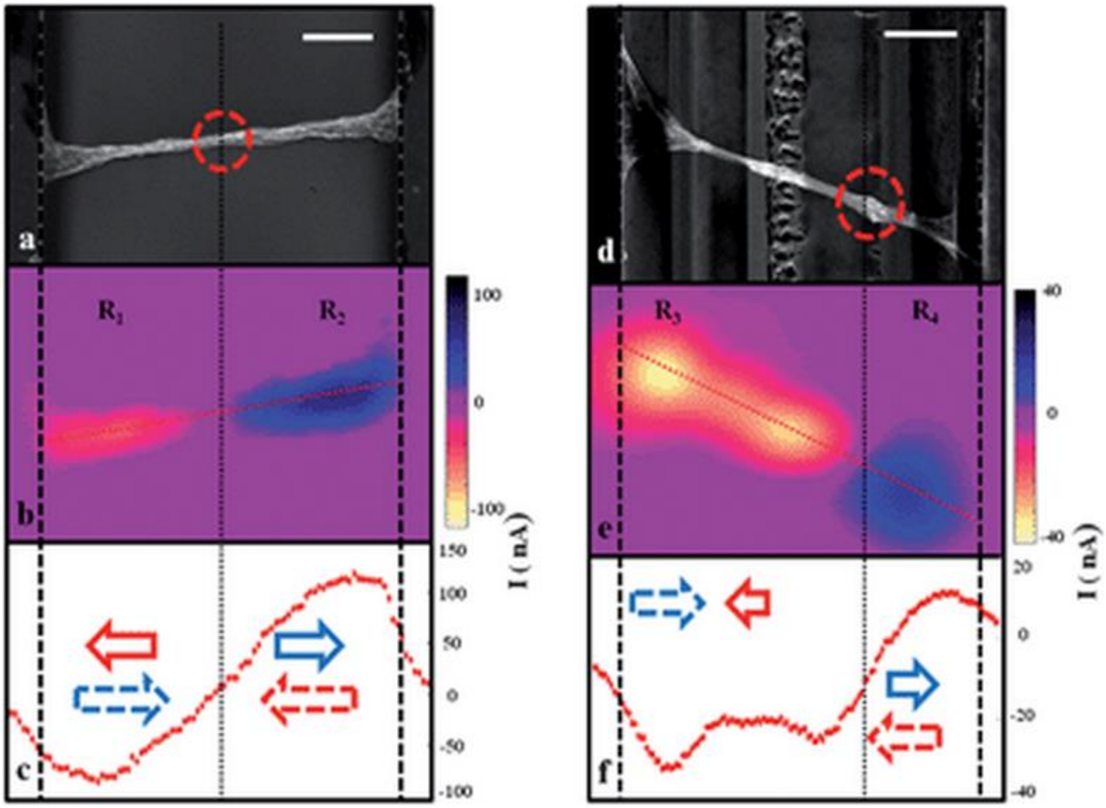

Figure 4.11. (a) and **(d)** SEM images of two different suspended CGRs across a trench. The red circles specify the "junction" areas. The scale bars are 1 μm. **(b)** and **(e)** the corresponding photocurrent images of the CGRs. **(c)** and **(f)** Line-cuts from the photocurrent images along the CGR, as marked by the red dotted lines. The solid arrows and the dashed arrows refer to the contributions from PVE and PTE, respectively. Blue color represents the negative current in the experimental setup used and red color corresponds to the positive current.

Unlike the previous device, the CGR device in Figure 4.11. (e) shows a dominant negative photocurrent response which may be due to the shift of the highly curled region from the middle to the right side of the curled ribbon (the junction between regions R_3 and R_4). As illustrated in Figure 4.11. (a). and 4.11. (d), we found that the dividing point of the photocurrent was strongly correlated with the junction-like structures (shown in red circles in Figure 4.11), where large morphology variance could be seen. Depending on the degree of curling, varying strengths of the interlayer interactions may be present in the said junctions, which may be the underlying factor behind the observed spreading of the photocurrent from $40\,nA$ to $100\,nA$ in different CGR structures in our experiment.

4.7. Conclusion

We have developed a simple method to synthesize free-standing quasi-1D curled graphene ribbons in high yields. We showed that a photocurrent enhancement of the order of 100 x can be achieved in CGR compared to flat suspended graphene. This high intrinsic (zero source drain bias) current is not possible in flat graphene where the rapid recombination of the photo excited electron hole pair, results in zero collected current. Our gate dependent scanning photocurrent measurements indicate that the photocurrent signal in CGR results mainly from the photothermoelectric effect (PTE) which is responsible for the augmentation of the photo response. The ability to change electrical and optical properties of graphene by simply modifying its morphology and achieving such high photo current responses, will provide a new exciting avenue for future graphene-based photovoltaics.

CHAPTER

5. OUTLOOK AND FUTURE WORK

5.1. The influence of the underlying substrate on the ultrafast carrier and phonon dynamics in 2D materials and 2D heterostructures

The emergence of 2D mono layer materials, starting with exfoliated graphene and its extremely high electron mobility and more recently Transition Metal Dichalcogenides (TMDC) with their large direct bandgap and high exciton energies, has opened exciting avenues for vastly improved performance and miniaturization of field effect transistors and opto-electronic devices. However, the *intrinsic* properties of 2D material systems are highly sensitive to the practical external environment. Placing these 2D membranes on a substrate, will affect both the equilibrium and non-equilibrium dynamics and inevitably influence the electrical and thermal properties and therefore the performance of any 2D based devices.

Understanding the interaction of carriers and phonons with each other and with those of the substrate in the first tens of picoseconds after carriers are excited to the conduction band and the consequent coupling of the acoustic phonons to the substrate in the hundreds of ps time scale, translates into understanding the full scale energy dissipation mechanisms in 2D devices. This complete picture, encompassing both short and longer time interactions with the substrate, is crucial in the FET device performance and thermal management. The results presented in this thesis clearly show that the ultrafast carrier dynamics in graphene are highly dependent on the substrate on which it resides. Given the striking difference we discovered in the relaxation times and behavior of carriers in graphene on different substrates in Chapter 3, it is important to develop a deep and systematic understanding of ultrafast carrier and phonon transfer dynamics of other 2D material systems and the key role that the underlying substrate plays in these processes.

5.1.1. Materials of interest

We intend to study 2 classes of 2D materials transferred on the most technologically relevant substrates: quartz, sapphire, doped and intrinsic diamond and HfO_2. The 2 classes include:

- TMDC (MoS_2, WS_2 and WSe_2).
- Van der Waals heterostructures. (in particular, combination of TMDC and graphene layers)

Since the 2D device architecture requires a vertical structure for practical device forms, it is absolutely critical to understand how the dynamical properties of 2D materials are altered by placement on substrates commonly used in the industry. We have designed a 3-prong ultrafast based-experimental plan to study the relaxation of carriers and both higher and lower energy phonons in 2D systems:

5.1.2. Ultrafast Pump Probe Spectroscopy (UPPS)

The main objective in a UPPS study is to mimic the behavior of 2D carriers in a high field FET, shortly after they have been excited to the conduction band. The extremely short time scales for these processes is beyond the resolution of any electronic devices and can only be resolved by ultrafast pulsed laser methods such as UPPS. By monitoring the relaxation of these excited carriers, we can not only resolve the carrier cooling rates but also the different energy relaxation pathways available to the excited electrons and the contribution of the substrate as an additional energy relaxation pathway through charge transfer or phonon coupling.

5.1.3. Time Resolved Photo Luminescence spectroscopy (TRPL)

TMDC’s are known for their high exciton energies and strong photoemission and are considered great contenders for photonic and optoelectronic devices. Given the direct band gap of these materials, TRPL will provide a unique opportunity to study the energy relaxation pathways through emission of photons in addition to the relaxation pathways through carrier-phonon scattering. Our goal is to resolve the substrate dependent exciton lifetimes and energies through studying the time resolved photon emission. One of our main interests is focused on evaluating the carrier-phonon coupling and the photon emission at the interface of Van der Waals heterostructures, in particular TMDC’s on graphene. We aspire to understand whether or not the interface provides additional energy relaxation channels that could alter, enhance or *compete* with the radiative photon emission and the carrier/phonon transport. Deciphering these fundamental mechanisms, presents the opportunity to tailor the radiative emission properties of TMDCs by changing the underlying substrate.

5.1.4. Coherent Acoustic Phonon interferometry (CAP)

CAP, a subset of UPPS, is conventionally performed by depositing a transducing layer on top of the studied sample. The absorption of the incident pumping laser by this layer, creates a local thermal stress and induces a transient elastic strain wave that propagates through the matter and can be used to non-destructively analyze the subsurface features in the depth of the material. Hundreds of picoseconds after photo-excitation, the bulk of the energy moves from the 2D electron system to the 2D lower energy phonon system and the immediate available energy relaxation channel becomes the coupling of acoustic phonon of the 2D layer to the substrate. Our objective is to use CAP interferometry to examine the efficiency and strength of this energy dissipation channel through generation and emission of out-of plane longitudinal acoustic phonons in the perpendicular direction into the substrate. Our *unconventional* use of the CAP technique involves focusing on the *strength and efficiency of the thermal stress generation* and the acoustic phonon coupling at the interface, rather than studying the bulk of the sample. We can accomplish this task, by using the 2D layer as a thermal inducer and comparatively study the generation of the longitudinal coherent acoustic waves and differences in the amplitude and frequency of the generated acoustic phonons on different substrates.

To advance the understanding of these critical phenomena, a quantitative model needs to be developed to depict the temporal evolution of the carrier temperature and density. Our emphasis is on considering *all competing energy relaxation pathways* such as carrier-phonon scattering, substrate charge transfer, photon emission and substrate phonon coupling and their associated rates and contributions to the ultrafast optical conductivity response of 2D materials.

5.2. Conclusion

Two of the most fundamental questions in physics and device sciences are: “Where does the energy of the excited electrons go?” And “How fast is this energy lost?” Our proposed sets of measurements will shed light on the role of the substrate in different energy relaxation mechanisms, activated at different time scales. Whether these channels are, optical phonon coupling, acoustic phonon coupling, carrier-phonon scattering or emission of photons, the proposed combination of these techniques will provide a complete and comprehensive picture. The possibility to selectively switch on and off the desired energy relaxation pathways and alter the associated relaxation rates, in addition to the possible ad hoc tuning of photon emission, by simply changing the substrate, is a very attractive option. This knowledge can provide a platform for not only understanding but also designing faster and more efficient 2D devices.

REFERENCES

[1] L. Landau, “Zur Theorie der phasenumwandlungen II,” *Phys. Z. Sowjetunion,* vol. 11, pp. 26 – 35, 1937.

[2] N. D. Mermin and H. Wagner, “Absence of Ferromagnetism or Antiferromagnetism in One- or Two-Dimensional Isotropic Heisenberg Models,” *Phys. Rev. Lett.*, vol. 17, no. 22, pp. 1133–1136, Nov. 1966.

[3] N. Mermin, “Crystalline Order in Two Dimensions,” *Phys. Rev.*, vol. 176, no. 1, pp. 250–254, Dec. 1968.

[4] P. Wallace, “The Band Theory of Graphite,” *Phys. Rev.*, vol. 71, no. 9, pp. 622–634, May 1947.

[5] D. P. DiVincenzo and E. J. Mele, “Self-consistent effective-mass theory for intralayer screening in graphite intercalation compounds,” *Phys. Rev. B*, vol. 29, no. 4, pp. 1685–1694, Feb. 1984.

[6] K. S. Novoselov, A. K. Geim, S. V Morozov, D. Jiang, Y. Zhang, S. V Dubonos, I. V Grigorieva, and A. A. Firsov, “Electric field effect in atomically thin carbon films.,” *Science*, vol. 306, no. 5696, pp. 666–9, Oct. 2004.

[7] A. Fasolino, J. H. Los, and M. I. Katsnelson, “Intrinsic ripples in graphene.,” *Nat. Mater.*, vol. 6, no. 11, pp. 858–61, Nov. 2007.

[8] K. S. Novoselov, A. K. Geim, S. V Morozov, D. Jiang, M. I. Katsnelson, I. V Grigorieva, S. V Dubonos, and A. A. Firsov, “Two-dimensional gas of massless Dirac fermions in graphene.,” *Nature*, vol. 438, no. 7065, pp. 197–200, Nov. 2005.

[9] C. Lee, X. Wei, J. W. Kysar, and J. Hone, “Measurement of the elastic properties and intrinsic strength of monolayer graphene.,” *Science*, vol. 321, no. 5887, pp. 385–8, Jul. 2008.

[10] I. Frank, D. Tanenbaum, A. Van der Zande, and P. McEuen, “Mechanical Properties of Suspended Graphene Sheets,” *Pomona Faculty Publications and Research*. 2007.

[11] A. A. Balandin, S. Ghosh, W. Bao, I. Calizo, D. Teweldebrhan, F. Miao, and C. N. Lau, “Superior thermal conductivity of single-layer graphene.,” *Nano Lett.*, vol. 8, no. 3, pp. 902–7, Mar. 2008.

[12] A. H. Castro Neto, N. M. R. Peres, K. S. Novoselov, and A. K. Geim, “The electronic properties of graphene,” *Rev. Mod. Phys.*, vol. 81, no. 1, pp. 109–162, Jan. 2009.

[13] A. Grüneis, C. Attaccalite, L. Wirtz, H. Shiozawa, R. Saito, T. Pichler, and A. Rubio, “Tight-binding description of the quasiparticle dispersion of graphite and few-layer graphene,” *Phys. Rev. B*, vol. 78, no. 20, p. 205425, Nov. 2008.

[14] K. I. Bolotin, K. J. Sikes, J. Hone, H. L. Stormer, and P. Kim, “Temperature-Dependent Transport in Suspended Graphene,” *Phys. Rev. Lett.*, vol. 101, no. 9, p. 096802, Aug. 2008.

[15] C. Canali, C. Jacoboni, F. Nava, G. Ottaviani, and A. Alberigi-Quaranta, “Electron drift velocity in silicon,” *Phys. Rev. B*, vol. 12, no. 6, pp. 2265–2284, Sep. 1975.

[16] C. Berger, Z. Song, X. Li, X. Wu, N. Brown, C. Naud, D. Mayou, T. Li, J. Hass, A. N. Marchenkov, E. H. Conrad, P. N. First, and W. A. de Heer, “Electronic confinement and coherence in patterned epitaxial graphene.,” *Science*, vol. 312, no. 5777, pp. 1191–6, May 2006.

[17] T. Mueller, F. Xia, and P. Avouris, “Graphene photodetectors for high-speed optical communications,” *Nat. Photonics*, vol. 4, no. 5, pp. 297–301, Mar. 2010.

[18] Z. Sun, T. Hasan, and A. C. Ferrari, “Ultrafast lasers mode-locked by nanotubes and graphene,” *Phys. E Low-dimensional Syst. Nanostructures*, vol. 44, no. 6, pp. 1082–1091, Mar. 2012.

[19] V. P. Gusynin, S. G. Sharapov, and J. P. Carbotte, “Unusual Microwave Response of Dirac Quasiparticles in Graphene,” *Phys. Rev. Lett.*, vol. 96, no. 25, p. 256802, Jun. 2006.

[20] N. M. R. Peres, “Colloquium : The transport properties of graphene: An introduction,” *Rev. Mod. Phys.*, vol. 82, no. 3, pp. 2673–2700, Sep. 2010.

[21] T. Stauber, N. M. R. Peres, and A. K. Geim, “Optical conductivity of graphene in the visible region of the spectrum,” *Phys. Rev. B*, vol. 78, no. 8, p. 085432, Aug. 2008.

[22] M. Mecklenburg, J. Woo, and B. C. Regan, “Tree-level electron-photon interactions in graphene,” *Phys. Rev. B*, vol. 81, no. 24, p. 245401, Jun. 2010.

[23] D. S. L. Abergel and V. I. Fal’ko, “Optical and magneto-optical far-infrared properties of bilayer graphene,” *Phys. Rev. B*, vol. 75, no. 15, p. 155430, Apr. 2007.

[24] G. Xing, H. Guo, X. Zhang, T. C. Sum, and C. H. A. Huan, “The Physics of ultrafast saturable absorption in graphene.,” *Opt. Express*, vol. 18, no. 5, pp. 4564–73, Mar. 2010.

[25] R. R. Nair, P. Blake, A. N. Grigorenko, K. S. Novoselov, T. J. Booth, T. Stauber, N. M. R. Peres, and A. K. Geim, “Fine structure constant defines visual transparency of graphene.,” *Science*, vol. 320, no. 5881, p. 1308, Jun. 2008.

[26] M. Fox, *Optical Properties of Solids*. OUP Oxford, 2010.

[27] L. A. Falkovsky and A. A. Varlamov, “Space-time dispersion of graphene conductivity,” *Eur. Phys. J. B*, vol. 56, no. 4, pp. 281–284, May 2007.

[28] H. Choi, F. Borondics, D. A. Siegel, S. Y. Zhou, M. C. Martin, A. Lanzara, and R. A. Kaindl, “Broadband electromagnetic response and ultrafast dynamics of few-layer epitaxial graphene,” *Appl. Phys. Lett.*, vol. 94, no. 17, p. 172102, Apr. 2009.

[29] L. A. Falkovsky, “Optical properties of graphene,” *J. Phys. Conf. Ser.*, vol. 129, no. 1, p. 012004, Oct. 2008.

[30] D. K. Efetov and P. Kim, “Controlling Electron-Phonon Interactions in Graphene at Ultrahigh Carrier Densities,” *Phys. Rev. Lett.*, vol. 105, no. 25, p. 256805, Dec. 2010.

[31] K. F. Mak, L. Ju, F. Wang, and T. F. Heinz, “Optical spectroscopy of graphene: From the far infrared to the ultraviolet,” *Solid State Commun.*, vol. 152, no. 15, pp. 1341–1349, Aug. 2012.

[32] K. F. Mak, J. Shan, and T. F. Heinz, “Seeing Many-Body Effects in Single- and Few-Layer Graphene: Observation of Two-Dimensional Saddle-Point Excitons,” *Phys. Rev. Lett.*, vol. 106, no. 4, p. 046401, Jan. 2011.

[33] L. Yang, J. Deslippe, C.-H. Park, M. L. Cohen, and S. G. Louie, “Excitonic Effects on the Optical Response of Graphene and Bilayer Graphene,” *Phys. Rev. Lett.*, vol. 103, no. 18, p. 186802, Oct. 2009.

[34] A. K. Geim and K. S. Novoselov, “The rise of graphene.,” *Nat. Mater.*, vol. 6, no. 3, pp. 183–91, Mar. 2007.

[35] I. Forbeaux, J.-M. Themlin, and J.-M. Debever, “High-temperature graphitization of the 6H-SiC face,” *Surf. Sci.*, vol. 442, no. 1, pp. 9–18, Nov. 1999.

[36] J. Hass, R. Feng, T. Li, X. Li, Z. Zong, W. A. de Heer, P. N. First, E. H. Conrad, C. A. Jeffrey, and C. Berger, “Highly ordered graphene for two dimensional electronics,” *Appl. Phys. Lett.*, vol. 89, no. 14, p. 143106, Oct. 2006.

[37] T. Kobayashi, M. Bando, N. Kimura, K. Shimizu, K. Kadono, N. Umezu, K. Miyahara, S. Hayazaki, S. Nagai, Y. Mizuguchi, Y. Murakami, and D. Hobara, “Production of a 100-m-long high-quality graphene transparent conductive film by

roll-to-roll chemical vapor deposition and transfer process," *Appl. Phys. Lett.*, vol. 102, no. 2, p. 023112, Jan. 2013.

[38] A. W. Tsen, L. Brown, M. P. Levendorf, F. Ghahari, P. Y. Huang, R. W. Havener, C. S. Ruiz-Vargas, D. A. Muller, P. Kim, and J. Park, "Tailoring electrical transport across grain boundaries in polycrystalline graphene.," *Science*, vol. 336, no. 6085, pp. 1143–6, Jun. 2012.

[39] C. Soldano, A. Mahmood, and E. Dujardin, "Production, properties and potential of graphene," *Carbon N. Y.*, vol. 48, no. 8, pp. 2127–2150, Jul. 2010.

[40] Y. Yao, C. Feng, J. Zhang, and Z. Liu, "'Cloning' of single-walled carbon nanotubes via open-end growth mechanism.," *Nano Lett.*, vol. 9, no. 4, pp. 1673–7, Apr. 2009.

[41] K. Celebi, M. T. Cole, J. W. Choi, F. Wyczisk, P. Legagneux, N. Rupesinghe, J. Robertson, K. B. K. Teo, and H. G. Park, "Evolutionary kinetics of graphene formation on copper.," *Nano Lett.*, vol. 13, no. 3, pp. 967–74, Mar. 2013.

[42] A. Reina, S. Thiele, X. Jia, S. Bhaviripudi, M. S. Dresselhaus, J. A. Schaefer, and J. Kong, "Growth of large-area single- and Bi-layer graphene by controlled carbon precipitation on polycrystalline Ni surfaces," *Nano Res.*, vol. 2, no. 6, pp. 509–516, Mar. 2010.

[43] C. Mattevi, H. Kim, and M. Chhowalla, "A review of chemical vapour deposition of graphene on copper," *J. Mater. Chem.*, vol. 21, no. 10, pp. 3324–3334, Feb. 2011.

[44] A. Pirkle, J. Chan, A. Venugopal, D. Hinojos, C. W. Magnuson, S. McDonnell, L. Colombo, E. M. Vogel, R. S. Ruoff, and R. M. Wallace, "The effect of chemical residues on the physical and electrical properties of chemical vapor deposited graphene transferred to SiO2," *Appl. Phys. Lett.*, vol. 99, no. 12, p. 122108, 2011.

[45] D. C. Elias, R. R. Nair, T. M. G. Mohiuddin, S V Morozov, P. Blake, M. P. Halsall, A. C. Ferrari, D. W. Boukhvalov, M. I. Katsnelson, A. K. Geim, and K. S. Novoselov, "Control of graphene's properties by reversible hydrogenation: evidence for graphane.," *Science*, vol. 323, no. 5914, pp. 610–3, Jan. 2009.

[46] M. W. Iqbal, A. K. Singh, M. Z. Iqbal, and J. Eom, "Raman fingerprint of doping due to metal adsorbates on graphene.," *J. Phys. Condens. Matter*, vol. 24, no. 33, p. 335301, Aug. 2012.

[47] T. J. Booth, P. Blake, R. R. Nair, D. Jiang, E. W. Hill, U. Bangert, A. Bleloch, M. Gass, K. S. Novoselov, M. I. Katsnelson, and A. K. Geim, "Macroscopic graphene membranes and their extraordinary stiffness.," *Nano Lett.*, vol. 8, no. 8, pp. 2442–6, Aug. 2008.

[48] Y.-C. Lin, C. Jin, J.-C. Lee, S.-F. Jen, K. Suenaga, and P.-W. Chiu, "Clean transfer of graphene for isolation and suspension.," *ACS Nano*, vol. 5, no. 3, pp. 2362–8, Mar. 2011.

[49] S. Scharfenberg, D. Z. Rocklin, C. Chialvo, R. L. Weaver, P. M. Goldbart, and N. Mason, "Probing the mechanical properties of graphene using a corrugated elastic substrate," *Appl. Phys. Lett.*, vol. 98, no. 9, p. 091908, Mar. 2011.

[50] M. Ishigami, J. H. Chen, W. G. Cullen, M. S. Fuhrer, and E. D. Williams, "Atomic structure of graphene on SiO2.," *Nano Lett.*, vol. 7, no. 6, pp. 1643–8, Jun. 2007.

[51] T. Li and Z. Zhang, "Substrate-regulated morphology of graphene," *J. Phys. D. Appl. Phys.*, vol. 43, no. 7, p. 075303, Feb. 2010.

[52] A. Reserbat-Plantey, D. Kalita, Z. Han, L. Ferlazzo, S. Autier-Laurent, K. Komatsu, C. Li, R. Weil, A. Ralko, L. Marty, S. Guéron, N. Bendiab, H. Bouchiat, and V. Bouchiat, "Strain superlattices and macroscale suspension of graphene induced by corrugated substrates.," *Nano Lett.*, vol. 14, no. 9, pp. 5044–51, Sep. 2014.

[53] T. Li and Z. Zhang, "Snap-Through Instability of Graphene on Substrates.," *Nanoscale Res. Lett.*, vol. 5, no. 1, pp. 169–173, Jan. 2009.

[54] O. A. Ivanov, A. B. Muchnikov, V. V. Chernov, S. A. Bogdanov, A. L. Vikharev, and J. E. Butler, "Experimental study of hydrogen plasma etching of (100) single crystal diamond in a MPACVD reactor," *Mater. Lett.*, vol. 151, pp. 115–118, Jul. 2015.

[55] P. Blake, E. W. Hill, A. H. Castro Neto, K. S. Novoselov, D. Jiang, R. Yang, T. J. Booth, and A. K. Geim, "Making graphene visible," *Appl. Phys. Lett.*, vol. 91, no. 6, p. 063124, Aug. 2007.

[56] S. Roddaro, P. Pingue, V. Piazza, V. Pellegrini, and F. Beltram, "The optical visibility of graphene: interference colors of ultrathin graphite on SiO(2).," *Nano Lett.*, vol. 7, no. 9, pp. 2707–10, Sep. 2007.

[57] D. M. Basko, S. Piscanec, and A. C. Ferrari, "Electron-electron interactions and doping dependence of the two-phonon Raman intensity in graphene," *Phys. Rev. B*, vol. 80, no. 16, p. 165413, Oct. 2009.

[58] a. C. Ferrari, J. C. Meyer, V. Scardaci, C. Casiraghi, M. Lazzeri, F. Mauri, S. Piscanec, D. Jiang, K. S. Novoselov, S. Roth, and a. K. Geim, "Raman spectrum of graphene and graphene layers," *Phys. Rev. Lett.*, vol. 97, no. 18, pp. 1–4, 2006.

[59] A. Eckmann, A. Felten, A. Mishchenko, L. Britnell, R. Krupke, K. S. Novoselov, and C. Casiraghi, "Probing the nature of defects in graphene by Raman spectroscopy.," *Nano Lett.*, vol. 12, no. 8, pp. 3925–30, Aug. 2012.

[60] L. G. Cançado, A. Jorio, E. H. M. Ferreira, F. Stavale, C. A. Achete, R. B. Capaz, M. V. O. Moutinho, A. Lombardo, T. S. Kulmala, and A. C. Ferrari, "Quantifying defects in graphene via Raman spectroscopy at different excitation energies.," *Nano Lett.*, vol. 11, no. 8, pp. 3190–6, Aug. 2011.

[61] M. Kalbac, A. Reina-Cecco, H. Farhat, J. Kong, L. Kavan, and M. S. Dresselhaus, "The influence of strong electron and hole doping on the Raman intensity of chemical vapor-deposition graphene," *ACS Nano*, vol. 4, no. 10, pp. 6055–6063, 2010.

[62] a Das, S. Pisana, B. Chakraborty, S. Piscanec, S. K. Saha, U. V Waghmare, K. S. Novoselov, H. R. Krishnamurthy, a K. Geim, a C. Ferrari, and a K. Sood, "Monitoring dopants by Raman scattering in an electrochemically top-gated graphene transistor.," *Nat. Nanotechnol.*, vol. 3, no. 4, pp. 210–215, 2008.

[63] M. Bruna, A. K. Ott, M. Ijäs, D. Yoon, U. Sassi, and A. C. Ferrari, "Doping dependence of the Raman spectrum of defected graphene," *ACS Nano*, vol. 8, no. 7, pp. 7432–7441, 2014.

[64] Z. H. Ni, T. Yu, Y. H. Lu, Y. Y. Wang, Y. P. Feng, and Z. X. Shen, "Uniaxial strain on graphene: Raman spectroscopy study and band-gap opening," *ACS Nano*, vol. 2, no. 11, pp. 2301–2305, 2008.

[65] T. M. G. Mohiuddin, a. Lombardo, R. R. Nair, a. Bonetti, G. Savini, R. Jalil, N. Bonini, D. M. Basko, C. Galiotis, N. Marzari, K. S. Novoselov, a. K. Geim, and a. C. Ferrari, "Uniaxial strain in graphene by Raman spectroscopy: G peak splitting, Grüneisen parameters, and sample orientation," *Phys. Rev. B - Condens. Matter Mater. Phys.*, vol. 79, no. 20, pp. 1–8, 2009.

[66] T. Yu, Z. Ni, C. Du, Y. You, Y. Wang, and Z. Shen, "Raman mapping investigation of graphene on transparent flexible substrate: The strain effect," *J. Phys. Chem. C*, vol. 112, no. 33, pp. 12602–12605, 2008.

[67] M. Lazzeri and F. Mauri, "Nonadiabatic Kohn Anomaly in a Doped Graphene Monolayer," *Phys. Rev. Lett.*, vol. 97, no. 26, p. 266407, Dec. 2006.

[68] C.-F. Chen, C.-H. Park, B. W. Boudouris, J. Horng, B. Geng, C. Girit, A. Zettl, M. F. Crommie, R. A. Segalman, S. G. Louie, and F. Wang, "Controlling inelastic light scattering quantum pathways in graphene.," *Nature*, vol. 471, no. 7340, pp. 617–20, Mar. 2011.

[69] L. Lindsay, D. A. Broido, and N. Mingo, "Flexural phonons and thermal transport in multilayer graphene and graphite," *Phys. Rev. B*, vol. 83, no. 23, p. 235428, Jun. 2011.

[70] J.-A. Yan, W. Y. Ruan, and M. Y. Chou, “Phonon dispersions and vibrational properties of monolayer, bilayer, and trilayer graphene: Density-functional perturbation theory,” *Phys. Rev. B*, vol. 77, no. 12, p. 125401, Mar. 2008.

[71] L. Lindsay and D. A. Broido, “Optimized Tersoff and Brenner empirical potential parameters for lattice dynamics and phonon thermal transport in carbon nanotubes and graphene,” *Phys. Rev. B*, vol. 81, no. 20, p. 205441, May 2010.

[72] H. Wang, Y. Wang, X. Cao, M. Feng, and G. Lan, “Vibrational properties of graphene and graphene layers,” *J. Raman Spectrosc.*, vol. 40, no. 12, pp. 1791–1796, Dec. 2009.

[73] R. Nicklow, N. Wakabayashi, and H. G. Smith, “Lattice Dynamics of Pyrolytic Graphite,” *Phys. Rev. B*, vol. 5, no. 12, pp. 4951–4962, Jun. 1972.

[74] D. L. Nika and A. A. Balandin, “Two-dimensional phonon transport in graphene.,” *J. Phys. Condens. Matter*, vol. 24, no. 23, p. 233203, Jun. 2012.

[75] A. Balandin and K. L. Wang, “Effect of phonon confinement on the thermoelectric figure of merit of quantum wells,” *J. Appl. Phys.*, vol. 84, no. 11, p. 6149, Dec. 1998.

[76] D. Li, Y. Wu, P. Kim, L. Shi, P. Yang, and A. Majumdar, “Thermal conductivity of individual silicon nanowires,” *Appl. Phys. Lett.*, vol. 83, no. 14, p. 2934, Sep. 2003.

[77] A. A. Balandin, “Thermal properties of graphene and nanostructured carbon materials.,” *Nat. Mater.*, vol. 10, no. 8, pp. 569–81, Aug. 2011.

[78] P. G. KLEMENS, “Theory of the a-Plane Thermal Conductivity of Graphite,” *J. Wide Bandgap Mater.*, vol. 7, no. 4, pp. 332–339, Apr. 2000.

[79] R. J. Nemanich, G. Lucovsky, and S. A. Solin, “Infrared active optical vibrations of graphite,” *Solid State Commun.*, vol. 23, no. 2, pp. 117–120, Jul. 1977.

[80] S. Piscanec, M. Lazzeri, F. Mauri, A. C. Ferrari, and J. Robertson, “Kohn Anomalies and Electron-Phonon Interactions in Graphite,” *Phys. Rev. Lett.*, vol. 93, no. 18, p. 185503, Oct. 2004.

[81] C. Thomsen and S. Reich, “Double Resonant Raman Scattering in Graphite,” *Phys. Rev. Lett.*, vol. 85, no. 24, pp. 5214–5217, Dec. 2000.

[82] D. L. Mafra, G. Samsonidze, L. M. Malard, D. C. Elias, J. C. Brant, F. Plentz, E. S. Alves, and M. A. Pimenta, “Determination of LA and TO phonon dispersion relations of graphene near the Dirac point by double resonance Raman scattering,” *Phys. Rev. B*, vol. 76, no. 23, p. 233407, Dec. 2007.

[83] R. J. Nemanich and S. A. Solin, “First- and second-order Raman scattering from finite-size crystals of graphite,” *Phys. Rev. B*, vol. 20, no. 2, pp. 392–401, Jul. 1979.

[84] A. Ferrari and J. Robertson, “Interpretation of Raman spectra of disordered and amorphous carbon,” *Phys. Rev. B*, vol. 61, no. 20, pp. 14095–14107, May 2000.

[85] T. Shimada, T. Sugai, C. Fantini, M. Souza, L. G. Cançado, A. Jorio, M. A. Pimenta, R. Saito, A. Grüneis, G. Dresselhaus, M. S. Dresselhaus, Y. Ohno, T. Mizutani, and H. Shinohara, “Origin of the 2450cm−1 Raman bands in HOPG, single-wall and double-wall carbon nanotubes,” *Carbon N. Y.*, vol. 43, no. 5, pp. 1049–1054, Jan. 2005.

[86] R. VIDANO and D. B. FISCHBACH, “New Lines in the Raman Spectra of Carbons and Graphite,” *J. Am. Ceram. Soc.*, vol. 61, no. 1–2, pp. 13–17, Jan. 1978.

[87] E. McCann and V. Fal’ko, “Landau-Level Degeneracy and Quantum Hall Effect in a Graphite Bilayer,” *Phys. Rev. Lett.*, vol. 96, no. 8, p. 086805, Mar. 2006.

[88] “Aa’ stacked graphite and fabrication method thereof.” 04-Feb-2010.

[89] A. C. Ferrari, “Raman spectroscopy of graphene and graphite: Disorder, electron–phonon coupling, doping and nonadiabatic effects,” *Solid State Commun.*, vol. 143, no. 1–2, pp. 47–57, Jul. 2007.

[90] J.-S. Hwang, Y.-H. Lin, J.-Y. Hwang, R. Chang, S. Chattopadhyay, C.-J. Chen, P. Chen, H.-P. Chiang, T.-R. Tsai, L.-C. Chen, and K.-H. Chen, “Imaging layer number and stacking order through formulating Raman fingerprints obtained from hexagonal single crystals of few layer graphene.,” *Nanotechnology*, vol. 24, no. 1, p. 015702, Jan. 2013.

[91] F. Tuinstra, “Raman Spectrum of Graphite,” *J. Chem. Phys.*, vol. 53, no. 3, p. 1126, 1970.

[92] L. G. Cançado, A. Jorio, and M. A. Pimenta, “Measuring the absolute Raman cross section of nanographites as a function of laser energy and crystallite size,” *Phys. Rev. B*, vol. 76, no. 6, p. 064304, Aug. 2007.

[93] S. Pisana, M. Lazzeri, C. Casiraghi, K. S. Novoselov, A. K. Geim, A. C. Ferrari, and F. Mauri, “Breakdown of the adiabatic Born-Oppenheimer approximation in graphene.,” *Nat. Mater.*, vol. 6, no. 3, pp. 198–201, Mar. 2007.

[94] D. M. Basko, “Theory of resonant multiphonon Raman scattering in graphene,” *Phys. Rev. B*, vol. 78, no. 12, p. 125418, Sep. 2008.

[95] K. F. Mak, M. Y. Sfeir, Y. Wu, C. H. Lui, J. A. Misewich, and T. F. Heinz, "Measurement of the Optical Conductivity of Graphene," *Phys. Rev. Lett.*, vol. 101, no. 19, p. 196405, Nov. 2008.

[96] D. Brida, A. Tomadin, C. Manzoni, Y. J. Kim, A. Lombardo, S. Milana, R. R. Nair, K. S. Novoselov, A. C. Ferrari, G. Cerullo, and M. Polini, "Ultrafast collinear scattering and carrier multiplication in graphene.," *Nat. Commun.*, vol. 4, p. 1987, Jan. 2013.

[97] T. Winzer, A. Knorr, and E. Malic, "Carrier multiplication in graphene.," *Nano Lett.*, vol. 10, no. 12, pp. 4839–43, Dec. 2010.

[98] E. H. Hwang, B. Y.-K. Hu, and S. Das Sarma, "Inelastic carrier lifetime in graphene," *Phys. Rev. B*, vol. 76, no. 11, p. 115434, Sep. 2007.

[99] E. Malic, T. Winzer, E. Bobkin, and A. Knorr, "Microscopic theory of absorption and ultrafast many-particle kinetics in graphene," *Phys. Rev. B*, vol. 84, no. 20, p. 205406, Nov. 2011.

[100] T. Winzer, A. Knorr, and E. Malic, "Carrier multiplication in graphene.," *Nano Lett.*, vol. 10, no. 12, pp. 4839–43, Dec. 2010.

[101] J. M. Dawlaty, S. Shivaraman, J. Strait, P. George, M. Chandrashekhar, F. Rana, M. G. Spencer, D. Veksler, and Y. Chen, "Measurement of the optical absorption spectra of epitaxial graphene from terahertz to visible," *Appl. Phys. Lett.*, vol. 93, no. 13, p. 131905, Sep. 2008.

[102] H. Wang, J. H. Strait, P. A. George, S. Shivaraman, V. B. Shields, M. Chandrashekhar, J. Hwang, F. Rana, M. G. Spencer, C. S. Ruiz-Vargas, and J. Park, "Ultrafast relaxation dynamics of hot optical phonons in graphene," *Appl. Phys. Lett.*, vol. 96, no. 8, p. 081917, Feb. 2010.

[103] S. Tani, F. Blanchard, and K. Tanaka, "Ultrafast Carrier Dynamics in Graphene under a High Electric Field," *Phys. Rev. Lett.*, vol. 109, no. 16, p. 166603, Oct. 2012.

[104] T. Li, L. Luo, M. Hupalo, J. Zhang, M. C. Tringides, J. Schmalian, and J. Wang, "Femtosecond Population Inversion and Stimulated Emission of Dense Dirac Fermions in Graphene," *Phys. Rev. Lett.*, vol. 108, no. 16, p. 167401, Apr. 2012.

[105] M. Breusing, C. Ropers, and T. Elsaesser, "Ultrafast Carrier Dynamics in Graphite," *Phys. Rev. Lett.*, vol. 102, no. 8, p. 086809, Feb. 2009.

[106] F. Rana, P. A. George, J. H. Strait, J. Dawlaty, S. Shivaraman, M. Chandrashekhar, and M. G. Spencer, "Carrier recombination and generation rates for intravalley and intervalley phonon scattering in graphene," *Phys. Rev. B*, vol. 79, no. 11, p. 115447, Mar. 2009.

[107] S. Butscher, F. Milde, M. Hirtschulz, E. Malić, and A. Knorr, “Hot electron relaxation and phonon dynamics in graphene,” *Appl. Phys. Lett.*, vol. 91, no. 20, p. 203103, Nov. 2007.

[108] P. A. George, J. Strait, J. Dawlaty, S. Shivaraman, M. Chandrashekhar, F. Rana, and M. G. Spencer, “Ultrafast optical-pump terahertz-probe spectroscopy of the carrier relaxation and recombination dynamics in epitaxial graphene.,” *Nano Lett.*, vol. 8, no. 12, pp. 4248–51, Dec. 2008.

[109] J. H. Strait, H. Wang, S. Shivaraman, V. Shields, M. Spencer, and F. Rana, “Very slow cooling dynamics of photoexcited carriers in graphene observed by optical-pump terahertz-probe spectroscopy.,” *Nano Lett.*, vol. 11, no. 11, pp. 4902–6, Nov. 2011.

[110] J. Shang, T. Yu, J. Lin, and G. G. Gurzadyan, “Ultrafast electron-optical phonon scattering and quasiparticle lifetime in CVD-grown graphene.,” *ACS Nano*, vol. 5, no. 4, pp. 3278–83, May 2011.

[111] L. M. Malard, K. Fai Mak, A. H. Castro Neto, N. M. R. Peres, and T. F. Heinz, “Observation of intra- and inter-band transitions in the transient optical response of graphene,” *New J. Phys.*, vol. 15, no. 1, p. 015009, Jan. 2013.

[112] K. Chen, H. Li, L.-P. Ma, W. Ren, T.-F. Chung, H.-M. Cheng, Y. P. Chen, and T. Lai, “Diversity of ultrafast hot-carrier-induced dynamics and striking sub-femtosecond hot-carrier scattering times in graphene,” *Carbon N. Y.*, vol. 72, pp. 402–409, Jun. 2014.

[113] *Optical Techniques for Solid-State Materials Characterization*. CRC Press, 2011.

[114] M. Sprinkle, D. Siegel, Y. Hu, J. Hicks, A. Tejeda, A. Taleb-Ibrahimi, P. Le Fèvre, F. Bertran, S. Vizzini, H. Enriquez, S. Chiang, P. Soukiassian, C. Berger, W. A. de Heer, A. Lanzara, and E. H. Conrad, “First direct observation of a nearly ideal graphene band structure.,” *Phys. Rev. Lett.*, vol. 103, no. 22, p. 226803, Nov. 2009.

[115] Y. Huang, X. Dong, Y. Shi, C. M. Li, L.-J. Li, and P. Chen, “Nanoelectronic biosensors based on CVD grown graphene.,” *Nanoscale*, vol. 2, no. 8, pp. 1485–8, Aug. 2010.

[116] R. W. Newson, J. Dean, B. Schmidt, and H. M. van Driel, “Ultrafast carrier kinetics in exfoliated graphene and thin graphite films,” *Opt. Express*, vol. 17, no. 4, p. 2326, Feb. 2009.

[117] T. Kampfrath, L. Perfetti, F. Schapper, C. Frischkorn, and M. Wolf, “Strongly Coupled Optical Phonons in the Ultrafast Dynamics of the Electronic Energy and Current Relaxation in Graphite,” *Phys. Rev. Lett.*, vol. 95, no. 18, p. 187403, Oct. 2005.

[118] B. Gao, G. Hartland, T. Fang, M. Kelly, D. Jena, H. G. Xing, and L. Huang, "Studies of intrinsic hot phonon dynamics in suspended graphene by transient absorption microscopy.," *Nano Lett.*, vol. 11, no. 8, pp. 3184–9, Aug. 2011.

[119] S. Wu, W.-T. Liu, X. Liang, P. J. Schuck, F. Wang, Y. R. Shen, and M. Salmeron, "Hot phonon dynamics in graphene.," *Nano Lett.*, vol. 12, no. 11, pp. 5495–9, Nov. 2012.

[120] N. Bonini, M. Lazzeri, N. Marzari, and F. Mauri, "Phonon Anharmonicities in Graphite and Graphene," *Phys. Rev. Lett.*, vol. 99, no. 17, p. 176802, Oct. 2007.

[121] I.-T. Lin, Y.-P. Lai, K.-H. Wu, and J.-M. Liu, "Terahertz Optoelectronic Property of Graphene: Substrate-Induced Effects on Plasmonic Characteristics," *Appl. Sci.*, vol. 4, no. 1, pp. 28–41, Feb. 2014.

[122] E. H. Hwang and S. Das Sarma, "Acoustic phonon scattering limited carrier mobility in two-dimensional extrinsic graphene," *Phys. Rev. B*, vol. 77, no. 11, p. 115449, Mar. 2008.

[123] K. Kaasbjerg, K. S. Thygesen, and K. W. Jacobsen, "Unraveling the acoustic electron-phonon interaction in graphene," *Phys. Rev. B*, vol. 85, no. 16, p. 165440, Apr. 2012.

[124] T. Stauber, N. M. R. Peres, and A. H. Castro Neto, "Conductivity of suspended and non-suspended graphene at finite gate voltage," *Phys. Rev. B*, vol. 78, no. 8, p. 085418, Aug. 2008.

[125] J.-Y. Park, S. Rosenblatt, Y. Yaish, V. Sazonova, H. Üstünel, S. Braig, T. A. Arias, P. W. Brouwer, and P. L. McEuen, "Electron−Phonon Scattering in Metallic Single-Walled Carbon Nanotubes," *Nano Lett.*, vol. 4, no. 3, pp. 517–520, Mar. 2004.

[126] E. H. Hwang, S. Adam, and S. Das Sarma, "Carrier Transport in Two-Dimensional Graphene Layers," *Phys. Rev. Lett.*, vol. 98, no. 18, p. 186806, May 2007.

[127] J.-H. Chen, C. Jang, S. Adam, M. S. Fuhrer, E. D. Williams, and M. Ishigami, "Charged-impurity scattering in graphene," *Nat. Phys.*, vol. 4, no. 5, pp. 377–381, Apr. 2008.

[128] E. H. Hwang and S. Das Sarma, "Surface polar optical phonon interaction induced many-body effects and hot-electron relaxation in graphene," *Phys. Rev. B*, vol. 87, no. 11, p. 115432, Mar. 2013.

[129] I.-T. Lin and J.-M. Liu, "Surface polar optical phonon scattering of carriers in graphene on various substrates," *Appl. Phys. Lett.*, vol. 103, no. 8, p. 081606, Aug. 2013.

[130] J.-H. Chen, C. Jang, S. Xiao, M. Ishigami, and M. S. Fuhrer, “Intrinsic and extrinsic performance limits of graphene devices on SiO2.,” *Nat. Nanotechnol.*, vol. 3, no. 4, pp. 206–9, Apr. 2008.

[131] S. Q. Wang and G. D. Mahan, “Electron Scattering from Surface Excitations,” *Phys. Rev. B*, vol. 6, no. 12, pp. 4517–4524, Dec. 1972.

[132] I. Meric, M. Y. Han, A. F. Young, B. Ozyilmaz, P. Kim, and K. L. Shepard, “Current saturation in zero-bandgap, top-gated graphene field-effect transistors.,” *Nat. Nanotechnol.*, vol. 3, no. 11, pp. 654–9, Nov. 2008.

[133] P. J. Hale, S. M. Hornett, J. Moger, D. W. Horsell, and E. Hendry, “Hot phonon decay in supported and suspended exfoliated graphene,” *Phys. Rev. B*, vol. 83, no. 12, p. 121404, Mar. 2011.

[134] S. Fratini and F. Guinea, “Substrate-limited electron dynamics in graphene,” *Phys. Rev. B*, vol. 77, no. 19, p. 195415, May 2008.

[135] X. Hong, K. Zou, A. M. DaSilva, C. H. Ahn, and J. Zhu, “Integrating functional oxides with graphene,” *Solid State Commun.*, vol. 152, no. 15, pp. 1365–1374, Aug. 2012.

[136] K. Zou, X. Hong, D. Keefer, and J. Zhu, “Deposition of High-Quality HfO 2 on Graphene and the Effect of Remote Oxide Phonon Scattering,” *Phys. Rev. Lett.*, vol. 105, no. 12, p. 126601, Sep. 2010.

[137] J. Sabio, C. Seoánez, S. Fratini, F. Guinea, A. H. C. Neto, and F. Sols, “Electrostatic interactions between graphene layers and their environment,” *Phys. Rev. B*, vol. 77, no. 19, p. 195409, May 2008.

[138] T. Low, V. Perebeinos, R. Kim, M. Freitag, and P. Avouris, “Cooling of photoexcited carriers in graphene by internal and substrate phonons,” *Phys. Rev. B*, vol. 86, no. 4, p. 045413, Jul. 2012.

[139] B. Scharf, V. Perebeinos, J. Fabian, and P. Avouris, “Effects of optical and surface polar phonons on the optical conductivity of doped graphene,” *Phys. Rev. B*, vol. 87, no. 3, p. 035414, Jan. 2013.

[140] A. G. Petrov and S. V. Rotkin, “Energy relaxation of hot carriers in single-wall carbon nanotubes by surface optical phonons of the substrate,” *JETP Lett.*, vol. 84, no. 3, pp. 156–160, Oct. 2006.

[141] W. T. Lynch, “Calculation of electric field breakdown in quartz as determined by dielectric dispersion analysis,” *J. Appl. Phys.*, vol. 43, no. 8, p. 3274, Nov. 1972.

[142] N. Sano, “A Monte Carlo study of hot-electron transport under a needle-plate assembly,” *J. Phys. D. Appl. Phys.*, vol. 22, no. 2, pp. 309–315, Feb. 1989.

[143] K. Kang, D. Abdula, D. G. Cahill, and M. Shim, “Lifetimes of optical phonons in graphene and graphite by time-resolved incoherent anti-Stokes Raman scattering,” *Phys. Rev. B*, vol. 81, no. 16, p. 165405, Apr. 2010.

[144] J. Yan, Y. Zhang, P. Kim, and A. Pinczuk, “Electric field effect tuning of electron-phonon coupling in graphene.,” *Phys. Rev. Lett.*, vol. 98, no. 16, p. 166802, Apr. 2007.

[145] M. Kubovi, A. Aleksov, A. Denisenko, and E. Kohn, “Advances in diamond surface channel FET technology with focus on large signal properties,” in *Proceedings. IEEE Lester Eastman Conference on High Performance Devices*, pp. 90–99.

[146] A. Denisenko, A. Aleksov, A. Pribil, P. Gluche, W. Ebert, and E. Kohn, “Hypothesis on the conductivity mechanism in hydrogen terminated diamond films,” *Diam. Relat. Mater.*, vol. 9, no. 3–6, pp. 1138–1142, Apr. 2000.

[147] A. Mazur, B. Sandfort, V. Gräschus, and J. Pollmann, *Festkörperprobleme 36*, vol. 36. Berlin, Heidelberg: Springer Berlin Heidelberg, 1996.

[148] D. R. Alfonso, D. A. Drabold, and S. E. Ulloa, “Phonon modes of diamond (100) surfaces from ab initio calculations,” *Phys. Rev. B*, vol. 51, no. 3, pp. 1989–1992, Jan. 1995.

[149] B. Y. Sun, Y. Zhou, and M. W. Wu, “Dynamics of photoexcited carriers in graphene,” *Phys. Rev. B*, vol. 85, no. 12, p. 125413, Mar. 2012.

[150] L. Huang, B. Gao, G. Hartland, M. Kelly, and H. Xing, “Ultrafast relaxation of hot optical phonons in monolayer and multilayer graphene on different substrates,” *Surf. Sci.*, vol. 605, no. 17–18, pp. 1657–1661, Sep. 2011.

[151] J. L. Warren, J. L. Yarnell, G. Dolling, and R. A. Cowley, “Lattice Dynamics of Diamond,” *Phys. Rev.*, vol. 158, no. 3, pp. 805–808, Jun. 1967.

[152] W. Hu, Z. Li, and J. Yang, “Diamond as an inert substrate of graphene.,” *J. Chem. Phys.*, vol. 138, no. 5, p. 054701, Feb. 2013.

[153] M. Lazzeri, C. Attaccalite, L. Wirtz, and F. Mauri, “Impact of the electron-electron correlation on phonon dispersion: Failure of LDA and GGA DFT functionals in graphene and graphite,” *Phys. Rev. B*, vol. 78, no. 8, p. 081406, Aug. 2008.

[154] M. Lazzeri and F. Mauri, “Coupled dynamics of electrons and phonons in metallic nanotubes: Current saturation from hot-phonon generation,” *Phys. Rev. B*, vol. 73, no. 16, p. 165419, Apr. 2006.

[155] J. Shah, *Ultrafast Spectroscopy of Semiconductors and Semiconductor Nanostructures*, vol. 115. Berlin, Heidelberg: Springer Berlin Heidelberg, 1999.

[156] L. Huang, G. V Hartland, L.-Q. Chu, Luxmi, R. M. Feenstra, C. Lian, K. Tahy, and H. Xing, “Ultrafast transient absorption microscopy studies of carrier dynamics in epitaxial graphene.,” *Nano Lett.*, vol. 10, no. 4, pp. 1308–13, Apr. 2010.

[157] E. J. H. Lee, K. Balasubramanian, R. T. Weitz, M. Burghard, and K. Kern, “Contact and edge effects in graphene devices.,” *Nat. Nanotechnol.*, vol. 3, no. 8, pp. 486–90, Aug. 2008.

[158] F. Xia, T. Mueller, R. Golizadeh-Mojarad, M. Freitag, Y. Lin, J. Tsang, V. Perebeinos, and P. Avouris, “Photocurrent imaging and efficient photon detection in a graphene transistor.,” *Nano Lett.*, vol. 9, no. 3, pp. 1039–44, Mar. 2009.

[159] Y. M. Zuev, W. Chang, and P. Kim, “Thermoelectric and Magnetothermoelectric Transport Measurements of Graphene,” *Phys. Rev. Lett.*, vol. 102, no. 9, p. 096807, Mar. 2009.

[160] P. Wei, W. Bao, Y. Pu, C. N. Lau, and J. Shi, “Anomalous Thermoelectric Transport of Dirac Particles in Graphene,” *Phys. Rev. Lett.*, vol. 102, no. 16, p. 166808, Apr. 2009.

[161] N. M. Gabor, J. C. W. Song, Q. Ma, N. L. Nair, T. Taychatanapat, K. Watanabe, T. Taniguchi, L. S. Levitov, and P. Jarillo-Herrero, “Hot carrier-assisted intrinsic photoresponse in graphene.,” *Science*, vol. 334, no. 6056, pp. 648–52, Nov. 2011.

[162] Z. Jarrahi, Y. Cao, T. Hong, Y. S. Puzyrev, B. Wang, J. Lin, A. H. Huffstutter, S. T. Pantelides, and Y.-Q. Xu, “Enhanced photoresponse in curled graphene ribbons.,” *Nanoscale*, vol. 5, no. 24, pp. 12206–11, Dec. 2013.

[163] M. Han, B. Özyilmaz, Y. Zhang, and P. Kim, “Energy Band-Gap Engineering of Graphene Nanoribbons,” *Phys. Rev. Lett.*, vol. 98, no. 20, p. 206805, May 2007.

[164] D. V Kosynkin, A. L. Higginbotham, A. Sinitskii, J. R. Lomeda, A. Dimiev, B. K. Price, and J. M. Tour, “Longitudinal unzipping of carbon nanotubes to form graphene nanoribbons.,” *Nature*, vol. 458, no. 7240, pp. 872–6, Apr. 2009.

[165] S. Tongay, M. Lemaitre, J. Fridmann, A. F. Hebard, B. P. Gila, and B. R. Appleton, “Drawing graphene nanoribbons on SiC by ion implantation,” *Appl. Phys. Lett.*, vol. 100, no. 7, p. 073501, Feb. 2012.

[166] J. G. Son, M. Son, K.-J. Moon, B. H. Lee, J.-M. Myoung, M. S. Strano, M.-H. Ham, and C. A. Ross, “Sub-10 nm Graphene Nanoribbon Array field-effect transistors fabricated by block copolymer lithography.,” *Adv. Mater.*, vol. 25, no. 34, pp. 4723–8, Sep. 2013.

[167] G. Liu, Y. Wu, Y.-M. Lin, D. B. Farmer, J. A. Ott, J. Bruley, A. Grill, P. Avouris, D. Pfeiffer, A. A. Balandin, and C. Dimitrakopoulos, "Epitaxial graphene nanoribbon array fabrication using BCP-assisted nanolithography.," *ACS Nano*, vol. 6, no. 8, pp. 6786–92, Aug. 2012.

[168] S. F. Braga, V. R. Coluci, S. B. Legoas, R. Giro, D. S. Galvão, and R. H. Baughman, "Structure and Dynamics of Carbon Nanoscrolls," *Nano Lett.*, vol. 4, no. 5, pp. 881–884, May 2004.

[169] X. Xie, L. Ju, X. Feng, Y. Sun, R. Zhou, K. Liu, S. Fan, Q. Li, and K. Jiang, "Controlled fabrication of high-quality carbon nanoscrolls from monolayer graphene.," *Nano Lett.*, vol. 9, no. 7, pp. 2565–70, Jul. 2009.

[170] L. Ortolani, E. Cadelano, G. P. Veronese, C. D. E. Boschi, E. Snoeck, L. Colombo, and V. Morandi, "Folded graphene membranes: mapping curvature at the nanoscale.," *Nano Lett.*, vol. 12, no. 10, pp. 5207–12, Oct. 2012.

[171] K. Kim, Z. Lee, B. D. Malone, K. T. Chan, B. Alemán, W. Regan, W. Gannett, M. F. Crommie, M. L. Cohen, and A. Zettl, "Multiply folded graphene," *Phys. Rev. B*, vol. 83, no. 24, p. 245433, Jun. 2011.

[172] W. Zhu, T. Low, V. Perebeinos, A. A. Bol, Y. Zhu, H. Yan, J. Tersoff, and P. Avouris, "Structure and electronic transport in graphene wrinkles.," *Nano Lett.*, vol. 12, no. 7, pp. 3431–6, Jul. 2012.

[173] P. Koskinen, "Electromechanics of twisted graphene nanoribbons," *Appl. Phys. Lett.*, vol. 99, no. 1, p. 013105, Jul. 2011.

[174] S. Cranford and M. J. Buehler, "Twisted and coiled ultralong multilayer graphene ribbons," *Model. Simul. Mater. Sci. Eng.*, vol. 19, no. 5, p. 054003, Jul. 2011.

[175] J. D. Peterson, S. Vyazovkin, and C. A. Wight, "Stabilizing effect of oxygen on thermal degradation of poly(methyl methacrylate)," *Macromol. Rapid Commun.*, vol. 20, no. 9, pp. 480–483, Sep. 1999.

[176] J. H. Los and A. Fasolino, "Intrinsic long-range bond-order potential for carbon: Performance in Monte Carlo simulations of graphitization," *Phys. Rev. B*, vol. 68, no. 2, p. 024107, Jul. 2003.

[177] S. Plimpton, "Fast Parallel Algorithms for Short-Range Molecular Dynamics," *J. Comput. Phys.*, vol. 117, no. 1, pp. 1–19, Mar. 1995.

[178] A. C. Ferrari and D. M. Basko, "Raman spectroscopy as a versatile tool for studying the properties of graphene.," *Nat. Nanotechnol.*, vol. 8, no. 4, pp. 235–46, 2013.

[179] F. Xia, T. Mueller, Y.-M. Lin, A. Valdes-Garcia, and P. Avouris, “Ultrafast graphene photodetector.,” *Nat. Nanotechnol.*, vol. 4, no. 12, pp. 839–43, Dec. 2009.

[180] T. Mueller, F. Xia, M. Freitag, J. Tsang, and P. Avouris, “Role of contacts in graphene transistors: A scanning photocurrent study,” *Phys. Rev. B*, vol. 79, no. 24, p. 245430, Jun. 2009.

[181] “Wiley: Physics of Semiconductor Devices, 3rd Edition - Simon M. Sze, Kwok K. Ng.” [Online]. Available: http://www.wiley.com/WileyCDA/WileyTitle/productCd-0471143235.html. [Accessed: 27-Aug-2015].

[182] G. Giovannetti, P. A. Khomyakov, G. Brocks, V. M. Karpan, J. van den Brink, and P. J. Kelly, “Doping Graphene with Metal Contacts,” *Phys. Rev. Lett.*, vol. 101, no. 2, p. 026803, Jul. 2008.

[183] J. Park, Y. H. Ahn, and C. Ruiz-Vargas, “Imaging of photocurrent generation and collection in single-layer graphene.,” *Nano Lett.*, vol. 9, no. 5, pp. 1742–6, May 2009.

[184] M. C. Lemme, F. H. L. Koppens, A. L. Falk, M. S. Rudner, H. Park, L. S. Levitov, and C. M. Marcus, “Gate-activated photoresponse in a graphene p-n junction.,” *Nano Lett.*, vol. 11, no. 10, pp. 4134–7, Oct. 2011.

[185] X. Xu, N. M. Gabor, J. S. Alden, A. M. van der Zande, and P. L. McEuen, “Photo-thermoelectric effect at a graphene interface junction.,” *Nano Lett.*, vol. 10, no. 2, pp. 562–6, Feb. 2010.

[186] S. Das Sarma, S. Adam, E. H. Hwang, and E. Rossi, “Electronic transport in two-dimensional graphene,” *Rev. Mod. Phys.*, vol. 83, no. 2, pp. 407–470, May 2011.

[187] D. Nezich, A. Reina, and J. Kong, “Electrical characterization of graphene synthesized by chemical vapor deposition using Ni substrate.,” *Nanotechnology*, vol. 23, no. 1, p. 015701, Jan. 2012.

[188] “Microchem corporation.” [Online]. Available: http://microchem.com/pdf/PMMA_Data_Sheet.pdf. [Accessed: 30-Nov-2015].

[189] “Graphene Industries.” [Online]. Available: http://grapheneindustries.com/.

[190] A. C. Ferrari and D. M. Basko, “Raman spectroscopy as a versatile tool for studying the properties of graphene,” *Nat Nano*, vol. 8, no. 4, pp. 235–246, Apr. 2013.

[191] L. M. Malard, M. A. Pimenta, G. Dresselhaus, and M. S. Dresselhaus, “Raman spectroscopy in graphene,” *Phys. Rep.*, vol. 473, no. 5–6, pp. 51–87, Apr. 2009.

[192] A. Das, S. Pisana, B. Chakraborty, S. Piscanec, S. K. Saha, U. V Waghmare, K. S. Novoselov, H. R. Krishnamurthy, A. K. Geim, A. C. Ferrari, and A. K. Sood, “Monitoring dopants by Raman scattering in an electrochemically top-gated graphene transistor.,” *Nat. Nanotechnol.*, vol. 3, no. 4, pp. 210–5, Apr. 2008.

[193] E. U. Stützel, “Fabrication and Optoelectronic Properties of Graphene Nanoribbons,” 2013.